T.C.
NECMETTİN ERBAKAN NİVERSİTESİ
FEN BİLİMLERİ ENSTİTÜSÜ

MATHEMATICAL MODELLING OF AIR-WATER FLOW STRUCTURE IN CIRCULAR DROPSHAFTS

Muhammed UÇAR

YÜKSEK LİSANS TEZİ

İnşaat Mühendisliği Anabilim Dalı

Temmuz-2021
KONYA

TEZ KABUL VE ONAYI

Muhammed UÇAR tarafından hazırlanan "**MATHEMATICAL MODELLING OF AIR-WATER FLOW STRUCTURE IN CIRCULAR DROPSHAFTS**" adlı tez çalışması 29/06/2021 tarihinde aşağıdaki jüri tarafından oy birliği ile Necmettin Erbakan Üniversitesi Fen Bilimleri Enstitüsü İnşaat Mühendisliği Anabilim Dalı'nda YÜKSEK LİSANS olarak kabul edilmiştir.

Jüri Üyeleri **İmza**

Başkan
Prof.Dr. M. Emin AYDIN

Danışman
Doç.Dr. Ş. Yurdagül KUMCU

Üye
Dr.Öğr.Üy. A. İhsan MARTI

Yukarıdaki sonucu onaylarım.

Prof. Dr. İbrahim KALAYCI
FBE Müdürü

TEZ BİLDİRİMİ

Bu tezdeki bütün bilgilerin etik davranış ve akademik kurallar çerçevesinde elde edildiğini ve tez yazım kurallarına uygun olarak hazırlanan bu çalışmada bana ait olmayan her türlü ifade ve bilginin kaynağına eksiksiz atıf yapıldığını bildiririm.

DECLARATION PAGE

I hereby declare that all information in this document has been obtained and presented in accordance with academic rules and ethical conduct. I also declare that, as required by these rules and conduct, I have fully cited and referenced all material and results that are not original to this work.

Muhammed UÇAR

Tarih:

ÖZET

YÜKSEK LİSANS TEZİ

DAİRESEL DÜŞÜLÜ BACALARDA HAVA-SU KARIŞIMININ MATEMATİKSEL MODELLEMESİ

Muhammed UÇAR

Necmettin Erbakan Üniversitesi Fen Bilimleri Enstitüsü
İnşaat Mühendisliği Anabilim Dalı

Danışman: Doç. Dr. Ş. Yurdagül KUMCU

2021, 96 Sayfa

Jüri
Doç.Dr. Ş. Yurdagül KUMCU
Prof.Dr. M. Emin AYDIN
Dr.Öğr.Üy. A. İhsan MARTI

Günlük yaşamda bireylerin ulaşım, haberleşme, temiz su ve atık su gibi hayati ihtiyaçları kent alt yapısı ile giderilmektedir. Kentlerde nufus artışı dolayısı ile oluşan yatay ve dikey büyümelerinin sonucunda da ciddi bir altyapı talebi ortaya çıkmaktadır. Gelişmekte olan kentlerin gerekli alt yapı sistemlerinin artan endüstriyel tesis ve konut talebine cevap verecek kapasitede projelendirilmesi gerekmektedir. Teknik alt yapının yetersiz kaldığı bölgelerde zamanla aşırı trafik, sel-yağmur baskınları, hava kirliliği sorunları ile otopark, içme ve kullanma suyu, haberleşme yetersizliği gibi sorunların oluşması kaçınılmaz olup bu sorunlar zamanla toplumsal problemlere ve sağlık problemlerine yol açacaktır. Bu noktada kent-medeniyet gelişiminin öncelikli faktörünün altyapı çalışmaları olduğu ve inşaat mühendisliğinin ingilizce karşılığının civil engineering-medeniyet mühendisliği olmasının ne kadar manidar olduğu anlaşılmaktadır.

Düşülü bacalar, kanalizasyon veya yağmur suyu gibi basınçsız akan borulu sistemlerde, hattın yönünü değiştirmek, düşü sağlamak ve enerji kırmak amacı ile kullanılan, genellikle dairesel kesitli imal edilen su yapılarıdır. Çalışma prensiplerinde akımın içinde oluşan hava miktarı önemlidir ve bu çalışmada temel olarak bu iki fazlı akım incelenmiştir. Enerji kırılması ve havalanma arasında doğrudan bağlantı bulunduğu Chanson (2002) tarafından gösterilmiş olup enerji kırılımına etkiyen faktörlerin ne oranda ve nasıl etki ettikleri henüz tam anlamıyla bilinmemektedir. Bu faktörlerin tam anlamıyla bilinmesi halinde ise daha efektif düşülü baca tasarımları yapılacak ve çok daha etkili altyapı sistemleri dizaynının önü açılmış olacaktır. Bu çalışmanın amacı da dizayn faktörlerinin Hesaplamalı Akışkanlar Dinamiği-HAD programları kullanılarak daha kapsamlı araştırılmasına rehberlik etmektir. İlgili programların tercih edilmesinin sebebi, hidrolik modellemeye göre daha az malzeme, işçilik ve zaman maliyeti olmasıdır. Kullanılan HAD programındaki girdilerin, çıktıların ve çözüm sisteminin yeterliliği daha önce yapılmış olan hidrolik deney sonuçları ile karşılaştırılması ile ortaya koyulmuştur.

Anahtar Kelimeler: Düşülü Bacalar, HAD, İki Fazlı Akış, Kanalizasyon Sistemi, Yağmur Suyu Sistemi

ABSTRACT

MS THESIS

MATHEMATICAL MODELLING OF AIR-WATER FLOW STRUCTURE IN CIRCULAR DROPSHAFTS

Muhammed UÇAR

THE GRADUATE SCHOOL OF NATURAL AND APPLIED SCIENCE OF
NECMETTİN ERBAKAN UNIVERSITY
THE DEGREE OF MASTER OF SCIENCE
IN CIVIL ENGINEERING

Advisor: Assoc. Prof. Dr. Ş. Yurdagul KUMCU

2021, 96 Pages

Jury
Assoc. Prof. Dr. Ş. Yurdagul KUMCU
Prof.Dr. M. Emin AYDIN
Asst. Prof.Dr. A. İhsan MARTI

Citizens' daily needs such as; transportation, communication, clean water and sewage are supplied with infrastructure systems. Horizontal and vertical expansion in the cities due to the increase in population leads to serious demand for infrastructural improvements. The infrastructure systems in developing cities are required to be designed in a satisfactory capacity to supply the increasing demand for residential and industrial constructions. The districts having insufficient infrastructure systems inevitably confront heavy traffic, flood, air pollution problems, and also having difficulties with the inadequacy of parking area, clear and potable water, communication. The problems may cause social and health problems over time. At this point, it is wished to emphasize that the primary factor of city-civilization development depends on infrastructural systems and it is meaningful to name the engineering field like civil engineering, literally leads civilization.

Dropshafts, commonly used in the urban storm and sewage water systems produced generally circular are used for energy dissipation and flow direction control. Aeration is significant for the working principle of the flow in dropshaft and this study is made mainly for this two-phase (air-water) physics of dropshafts. Chanson showed that aeration and energy dissipation is directly linked to each other (2002), but the influencing factors and the action mechanisms of the factors on the phenomena are not discovered entirely. By the comprehension of the factors, more effective dropshafts will be able to design. This study aims to guide the more comprehensive investigation of design factors using Computational Fluid Dynamics-CFD programs. The reasons for the preference of the programs are the cost-effectiveness of material, workmanship and duration relative to hydraulic modelling. The competence of the inputs, outputs and solution system of the CFD code is validated by the comparison of previous hydraulic modelling results.

Keywords: CFD, Dropshaft, Sewer system, Storm Water System, Two-Phase Flow

ÖNSÖZ

Bu tez çalışmasında DAİRESEL DÜŞÜLÜ BACALARDA HAVA-SU KARIŞIMININ MATEMATİKSEL MODELLEMESİ incelenmek istenmiştir.

Öncelikle tez konumu belirlerken taleplerimi göz önünde bulundurarak bana yardımcı olan danışmanım Doç. Dr. Şerife Yurdagül Kumcu'ya teşekkürlerimi sunarım. Değerli bölüm hocalarıma ve tüm eğitim hayatım boyunca benden maddi ve manevi desteklerini esirgemeyen her zaman yanımda olan sevgili eşime ve aileme teşekkürlerimi bir borç bilirim.

Muhammed UÇAR
KONYA-2021

İÇİNDEKİLER

NOMENCLATURE

A_s	Surface area (m^2)
AC	Aeration coefficient
β	Relative air demand
BC	Boundary condition
C	Aeration concentration
C_{air}	Coefficient of proportionality
d_c	Critical inflow depth
d_i	Free-jet thickness at impingement location
D_{in}	Inlet pipe diameter (m)
D_{out}	Outlet pipe diameter (m)
D_s	Shaft diameter (m)
D_M	Manhole diameter (m)
$D^{\#}$	Dimensionless air bubble diffusivity
ϵ	Turbulent dissipation rate (m^{2}s^{-3})
E_0	Inflow local energy head (m)
E_d	Downstream local energy head (m)
η	Relative energy head loss
F	Volume of fluid (VoF) function
F_0	Approach flow Froude number
F_{0ch}	Approach flow choking Froude number
F_I	Impact Froude number
f_i	Gravity component (ms^{-2})
g	Gravity acceleration (ms^{-2})
g_n	Component of gravity normal to the free surface (ms^{-2})
G_k	Generation of turbulent energy caused by the average velocity gradient
h_0	Water depth of inflow conduit (m)
H_0	Inflow energy head (m)
H_d	Downstream energy head (m)
I	Froude type impact number
k	Turbulent kinetic energy (kg.ms^{-2})
L_s	Length of rectangular shaft
L_T	Turbulence length scale (m)
p	Gauge pressure (pa)
P	Pool height (m)
P_d	Disturbance energy per unit volume (Nm^{-2})
P_t	Stabilizing forces per unit volume (Nm^{-2})
ρ	Water density (kg.m^{-3})
ρ_a	Air density (kg.m^{-3})
ρ_{mac}	The density of mixture-macroscopic density (kg.m^{-3})
s	Drop height (m)
S	Dimensionless drop height
SDM	Stacked Drop Manhole
Q	Discharge (m^{3}s^{-1})
Q^*	Manhole Froude number
Q_a	Air flowrate (m^{3}s^{-1})
γ	Specific weight of water (Nm^{-3})
t	Time (s)

T	Particle residence time (s)
u_i	Velocity component (m/s)
μ	Coefficient of dynamic viscosity (kg.m^{-1}s^{-1})
μ_{eff}	Revisionary coefficient of dynamic viscosity (kg.m^{-1}s^{-1})
ν	Coefficient of kinematic viscosity (m^{2}s^{-1})
ψ	Choking parameter
ψ_{ch}	Choking number related to approach filling ratio
V_0	Average approach flow velocity (ms^{-1})
δV	Volume of entrained air per unit time m^3
σ	Coefficient of surface tension (Nm^{-1})
θ	Angle between the velocity direction and the vertical direction
λ	Factor of friction loss
y_0	Approach conduit filling ratio
x_i	Coordinate component

LIST OF TABLES

LIST OF FIGURES

1 INTRODUCTION

1.1 Background

Stormwater and wastewater drainage systems are primarily designed to collect water into a downstream reservoir or treatment plant by gravity movement. Adequate drop structures should be provided to eliminate the elevation difference from end to end to ensure pipeline installation without exceeding maximum slope requirements and speed limitations. Not only to reduce the peak velocity but also to meet maintenance requirements, the sewage slope is reduced by suitable drop structures using suitable intervals. Dropshafts are serving on these purposes and are extensively used in urban sewer and stormwater systems. Chanson (2000) divides their purpose into three ways; slope requirements for steep topographies, dissipation of excess kinetic energy and aeration (re-oxygenation) to raise the water quality. A strong relationship exists between energy dissipation and aeration (Chanson, 2002).

The phenomenon of aeration is also associated with the unpleasant odour from the sewer line; anaerobic bacteria that live in places with low oxygen content produce Hydrogen Sulfide (H_2S) (Zhang et al., 2016). A community of anaerobic bacteria living on the submerged pipe wall forms biofilms (*Figure* ***1.1***). The thickness of this formation can vary from a few micrometres to a few centimetres. Bacteria are active only in the absence of nitrate and oxygen; therefore, oxygen and nitrate enrichment processes are widely used in the control of hydrogen sulfide emission (Jensen *et al.*, 2016). Moeller & Natarian states that the substantial test data and physical evidence indicate the occurrence most hydrogen sulfide emissions are at the drops, rather than the pipes. In most practical cases, the wastewater contains a remarkable amount of potentially volatile dissolved molecular H_2S. The existence of an anaerobic environment causes severe corrosion, which reduces the service life of the pipeline system significantly. Moreover, the anaerobic bacteria release H_2S gas in drop structures, which causes odour emission. Vertical drops have beneficial aspects when sewerage is still fresh and contains relatively low dissolved hydrogen sulfides. Intensive re-aeration and flow turbulence at these drops increase the dissolved oxygen level in such sewers. These types of O_2 supplementation prevents the consumption of dissolved oxygen to a considerable pipe length (2000).

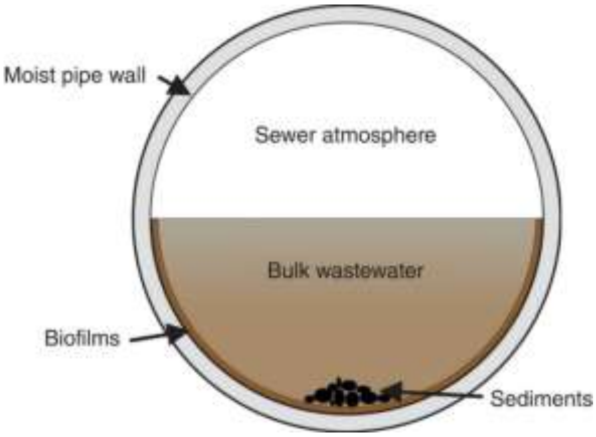

Figure 1.1 Cross-section of a typical sewer pipe highlighting different environments (Jensen *et al., 2016)*

While Sousa et al. (2009) defined the key practical variance between manholes and dropshafts as the bottom pool realizations to avoid the erosion of the floor. Ma et al. (2017) define the dropshafts with drop heights of more than 5m, authors state that the disintegration of water flow produces droplets resulting in excessive air entrainment and energy dissipation. Drop manhole height limitation is suggested by the authors to be 3m, the heights between are classified as transitional.

Christodoulou (1991) suggested a height requirement for drop structures considering sufficient energy dissipation; that is, maintaining a pool depth smaller than the drop height while producing a head loss greater than that. In North America, most of the municipal guidelines limited the height of manholes to 1m (the City of Calgary, 2000). In the design guide of the City of Edmonton, a drop structure should be used for differences of elevation higher than 1m between the incoming and outgoing pipes. The manhole must be equipped with air vents and designed following the requirements specified in the design manuals (Camino, 2011). There is no experimental or theoretical basis supporting these limits; however, the restriction reduces potential harmful effects, such as; vibration, erosion, or abrasion of structure and odour related to excessive air entrainment (Hager, 1999). The City of Edmonton (2015) has provided design criteria for drop structures according to the inlet, vertical shaft and outlet dimensions. While the inlet pipe should be large enough to avoid subcritical overflow conditions, vertical shaft diameter is recommended to be equal or greater than that of the largest inlet sewer, and the outflow connections must provide a hydraulic jump to convert the flow to the subcritical regime. Ardıclıoglu states that the drop height does not exceed 2m in Turkey, but may increase to 4m for essential conditions (2017).

Despite all these studies mentioned in detail in the literature section, the design criteria such as the ratios between diameters, drop height, pool depth & maximum allowable discharge, still could not be developed at the desired level.

1.2 Research Objectives and Scope

Understanding the flows in plunging drop structures could enable efficient ways to transport water between different elevations in urban drainage systems. Numerous research has been done to expand the understanding of the phenomena but the investigations are limited by physical conditions such as; limited flow field information, high costs, long-lasting test setup installations, and the unavoidable scale effects. With the recent development of data processing technology, solutions to complex hydraulic problems have been provided by using various mathematical models. High-capacity workstation computers and the efficient Computational Fluid Dynamics (CFD) codes provide a virtual laboratory, serving realistic fluid flow solutions. While the numerical model has many advantages over the physical model, it must be validated by the results of the physical model. Consequently, by the use of a validated numerical model, valuable flow information can be obtained.

The scope of the study is investigating the two-phase flow hydraulics of a circular dropshaft with a commercially available Computational Fluid Dynamics (CFD) program by solving the Reynolds Averaged Navier-Stokes (RANS) equations. Numerical modelling was conducted in a single dropshaft geometry under different flow conditions and solver technique options. The available computational options in the program are examined to capture free surface and aeration properties approximate to the real experimentation data. Water profiles, impact locations, energy dissipations & other two-phase flow features are analyzed for three basic flow regimes (R1, R2 and R3).

The main objective of this thesis is to investigate the numerical flow parameters of dropshafts to facilitate further investigations of flow field optimizations, which can be carried out directly on numerical models by the guide of this thesis.

2 LITERATURE SEARCH

There are two main categories of vertical fall structures, which can be distinguished by height and input characteristics: a) vortex dropshafts and b) plunging type drop structures: dropshafts and drop manholes (*Figure 2.1*). The vortex dropshafts allow the flow to substantially wind down the vertical shaft held along the shaft walls, and the air acts as a central air core (Hager, 1999). The plunge droplet structures direct the flow directly to the vertical shaft and there is no provision for airflow within the shaft.

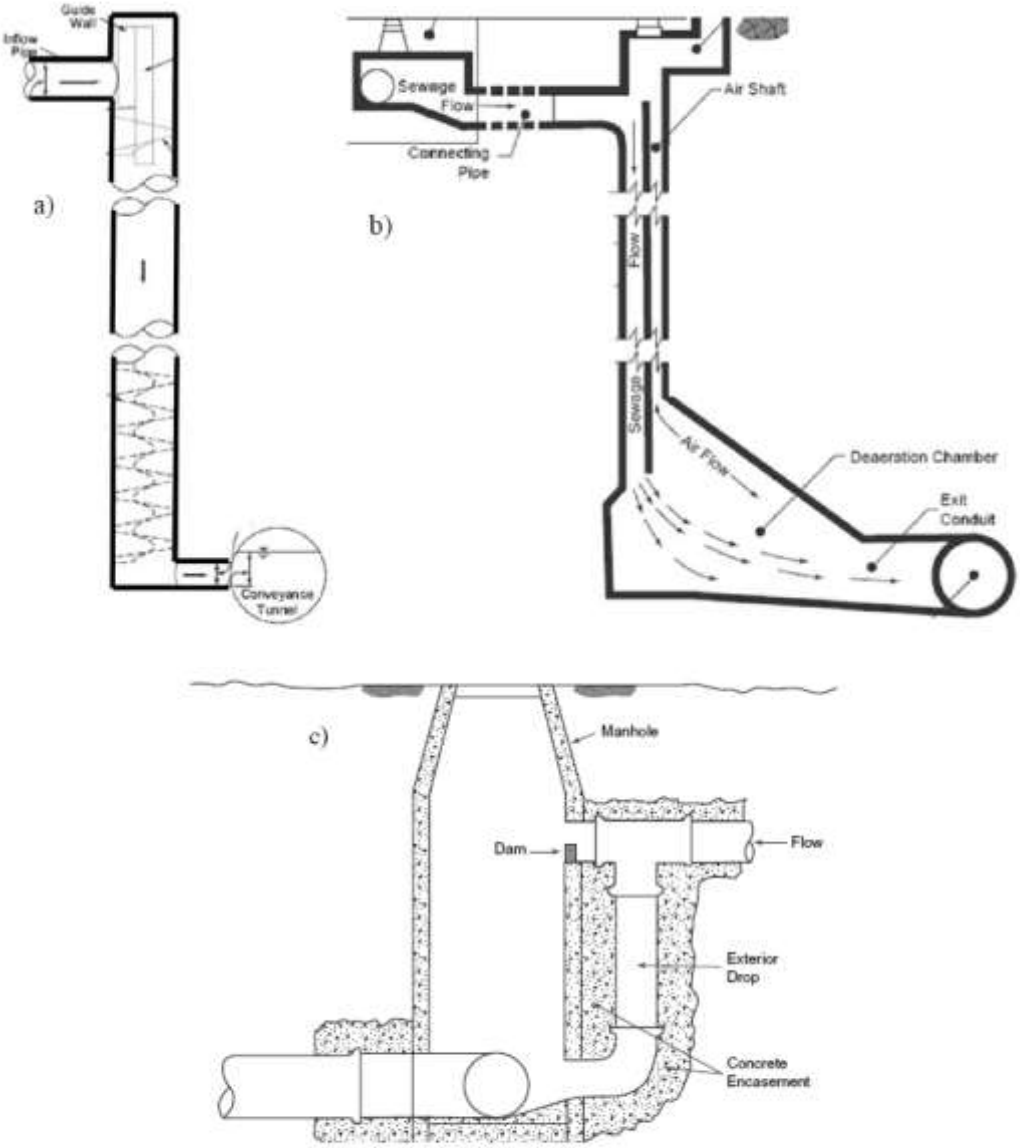

Figure 2.1 Typical urban drainage drop structures: a) vortex dropshaft of the helical inlet; b) plunging dropshaft of elbow entrance; and, c) sanitary drop manhole or dropshaft (Camino, 2011)

2.1 Historical Background of Flow Patterns

Until Chanson (1999), dropshafts were thought to act as sediment traps in historical Roman aqueducts in which the dropshaft cascades (i.e. a series of vertical dropshafts) were used for dissipation of the kinetic energy. With the physical model tests made by Chanson (1999, 2000) at the University of Queensland, Roman dropshaft hydraulics have re-analyzed. Despite some arguments suggesting that Roman aqueducts maintained a fluvial flow in some regimes, it is suggested that these steep conditional drops produce supercritical flows that require a technical response to ensure normal water flow. In his work, he states that there are three techniques used by the Romans to solve this problem: chutes followed by stilling basins, dropshafts and stepped channels. The results show that vertical dropshafts can be very efficient energy breakers and re-oxygenation structures under suitable flow conditions. Optimal working conditions of dropshafts were discussed and, to predict these conditions, an analytical model was developed. Besides, the performance of aqueduct dropshafts and modern dropshaft designs were compared (Chanson, 1999).

The first modern research in this field began in the early 90s. Christodoulou (1991) experimentally explored the hydraulic behaviour of a circular drop manhole model consisting of a 500 mm diameter vertical pipe, connected to two pipes of diameters 190 mm and 2 m long each. Local head loss and water level in the manhole was found to be mainly due to a dimensionless drop parameter, expressed by the drop height and the approach flow velocity. Christodoulou (1991) also stated that the level of manhole water depends on the angle between the inflow and outflow directions. Also, an empirical expression was suggested for the local head-loss coefficient as a function of the drop parameter only. Therefore, evaluation of the local energy loss due to a simple drop manhole for supercritical approach flow is expressed.

Rajaratnam et al. (1997) experimented on a circular dropshaft model with a diameter of 290 mm and a length of 2.11 m. This vertical shaft was connected to a horizontal outlet pipe of the same diameter close to the base, and an inlet pipe with a diameter of 154 mm. The authors described the conditions that caused flow choking and demonstrated the significance of providing an inlet curve to increase conveying capacity. The authors also investigated and reported energy losses especially due to the jet impact on the opposite sidewall in ways as; the friction resistance of the spiral flow along the shaft, surface hydraulic jump formation on the jet, and the turbulent mixture in the pool. The characteristics of air demand mechanisms of a dropshaft have also been investigated to enhance the hydraulic performance of these dropshafts.

De Martino et al. (2002) analyzed some flow characteristics for the supercritical approach flow in small and medium drops. Their position relative to the flow depth and droplet portion below a drop was obtained. Besides, they produced a cut-off scheme as a function of the pipe fill for various relative drop heights, indicating that the droplets could lead to a significant reduction in the discharge capacity.

Pagliara & Dazzini (2002) explained the energy loss of different types of dropshafts. Experimental results show relative energy losses as a function of a dimensionless critical flow depth for a single drop. The results of both Chanson (2004) and Pagliara & Dazzini (2002) are applied to the subcritical approach flows in rectangular sewers.

Chanson systematically researched two prototypes and five small models of drop structures in 2002. Experimental observations have shown three basic flow regimes for dropshaft configurations with 180 degrees of outflow direction while two flow regimes have been observed with a 90-degree outflow direction. Chanson stated that the energy dissipation rate at the low flow rates in the dropshafts was approximately 95%. In the models, the depth of the pool, which is prone to water abrasion, had just little impact on the hydraulic characteristics of the dropshaft, but a larger amount of energy dissipation was consistent with the 90º outflow direction. For low deep shaft pools and flow rates, the residence time probability distribution functions showed a bi-modal distribution in both prototype and model. At low flow rates, the data were compared successively with an analytical solution of the diffusion equation associated with the air bubble. From less than 0.5 mm to more than 25 mm, Pseudo-bubble chord size measurements showed a very wide range of air bubble sizes, with mean pseudo-bubble chords between 10 and 20 mm. The chord size distribution was skewed by the advantage of small bubbles regarding the mean. Analysis of the distribution of bubbles in the direction of flow has shown that the majority of clusters consist of only 2 bubbles and associated with a cluster structure there can be stated as a fair proportion of bubbles. Acoustic traces of bubbly flow accurately characterize changes in flow regimes. However, the conversion from acoustic frequencies to bubble radii has underestimated the entrained bubble dimensions and could not predict the shape of the bubble size probability distribution functions, which is measured by the interfering conductivity probes. (Chanson, 2002)

The hydraulics of rectangular dropshafts were examined by Chanson (2004), who conducted his study on seven dropshafts: a) five designed to investigate the drop height (s=0.55 and 0.87 m), outflow direction (90° and 180°) and the effects of the shaft pool or sump (pool height P=0 and 0.32 m); and, b) two historic in-situ geometries were geometrically scaled (with a ratio 3.1). His attention was focused on the effects of the pool shaft, drop height and outflow direction. The experiments of Chanson covered three different flow regimes depending on the nappe effect in the sump, the outflow condition and the opposite sidewall. Chanson also states that the presence of a reservoir (pool height $P\neq$ 0 m) that allowed a pool at the bottom of the shaft had little effect on energy losses. On the contrary, larger losses were observed in a dropshaft in the direction of 90°. The drop height has little effect on energy losses when comparing dropshafts with 90° outlet and without a sump. Similarly, outflow direction, the shaft pool and shaft height had little impact on the dimensionless water level in the shaft pool. A relatively close fit between the model and the prototype was observed in terms of pool height and energy losses. Instead, observations on recirculation times and bubble penetration depths revealed significant differences between model and prototype. In the prototype, smaller bubble swarm depths were observed (Chanson, 2004).

To advance the available information on the dropshafts, de Marinis et al. (2007) designed a flexible test device that allows systematic analysis of the outstanding flow parameters at relatively wide test ranges. The thing includes the Froude number of approach flow; diameters of inlet and outlet pipes, dropshaft drop height and dropshaft base shape. The new experimental setup facilitates studying the behaviour in both the absence and presence of external airflow. The absence case was carried out with hermetic dry seals; it is useful to analyze prototype-operating conditions of dropshafts where a sufficient ventilation system is not frequently available.

Jalil (2009) examined a variable dropshaft with variable drop heights. The results obtained show that the air entrainment for a given shaft height increases with increasing water discharge, and for a certain discharge, dropshaft height increases with increasing discharge, more increased for $s/D_s \geq 6.6$. Energy dissipation in plunging. The dropshaft is also increased as the dropshaft height increases, and as the water drop increases, the height of a given dropshaft decreases.

Related to a construction project in Edmonton, Canada, a model study on a special offset SDM is conducted by Camino et al., (2009). Instead of a large drop of 50 meters, a series of stacked dropshafts was proposed. The SDM option was estimated to reduce the total cost by approximately 70% of the large reduction shaft option, which is about $ 1 million (Canadian Dollar). The offset and symmetric SDM correspond to the alignment of the inflow direction with the centreline of the opening portion connecting the two chambers (*Figure* ***2.6***). Symmetric SDM has been proposed to extend the previous results in offset design to a more compact and simplified arrangement that will help standardize its use.

Granata et al. (2010) conducted laboratory studies at the University of Cassino to investigate the choking characteristics of dropshafts in sewage systems. Details of the study are given in the next sections 2.2-2.3. Geometric data can be found in the table.

Specific jet breaker devices have been contemplated by Granata et al. (2014) to improve flow conditions. In the study, two different types of jet breakers, namely wedge jet breaker (WJB) and plane jet breaker (PJB) have been examined. In the study results, both are effective in increasing the overall performance of the wells and inducing adequate energy loss if they are appropriately sized. The selection and sizing of the jet-breaker element should take into account the supplementary features of the dropshaft hydraulics, including air entrainment events, pool depth, as well as other practical considerations, including the risk of clogging, cost-effectiveness and the ease of realization. The study provides a hydraulic foundation for the design of the jet breakers, PJB, in particular, having the generally optimum performance, as demonstrated by laboratory experiments.

Table 2.1 Geometry of previous models on plunging drop manholes and dropshafts (after Camino, 2011)

Author	**Inlet cross-section**		**Approach flow**	**Shaft section**			**Outlet conduit**
				Shape	**D_s/d**	**Slenderness ratio s/D_s**	
Gayer (1984)	circl	D_{in}=0.30m	$F_0 > 1$	circl	3.3	0.5~0.8	D_{in}
Christodoulou (1991)	circl	D_{in}=0.19m	$F_0 > 1$	circl	2.6	0.1~2.6	D_{in}
Rajaratnam (1997)	circl	D_{in}=0.15m	$F_0 < 1$	circl	1.9	6.6	$1.9D_{in}$
Calomino et al. (1999)	circl	D_{in}=0.10m	$F_0 > 1$	circl	1.5~1.4	0~3.3	D_{in}
Chanson (2004)	rect	b=0.50m b=0.16m	$F_0 < 1$	rect rect	1.5	2.2~3.6	1.3b; b 1.3b
De Marinis (2007)	circl	D_{in}=0.20m	$F_0 > 1$	circl	5.0	2.0	D_{in}
Jalil (2009)	circl	D_{in}=0.15m	$F_0 < 1$	circl	2.0	10.8 7.4	D_{in}; $2D_{in}$
Granata et al. (2010)	circl	D_{in}=0.20m	$F_0 > 1$	circl	5.0	2.1; 2.5; 3.1	D_{in}
62 Avenue dropshaft city Edmonton	circl	D_{in}=1.20m	variable	circl	1.0	19.7	$1.33D_{in}$
Camino (2011)	circl	D_{in}=0.19m	$F_0 < 1$	circl	2.0	19.8	$2D_{in}$
Kumcu & Kokpinar (2013)	circl	D_{in}=0.20m	$F_0 < 1$	circl	1.78	1.35	D_{in}
Zheng et al. (2017)	circl	D_{in}=0.20m	$F_0 < 1$	circl	2.7	1.72; 2.78; 4.44	D_{in}

b=inlet width; d=inlet diameter; circl = Circular; rect=Rectangular; F_0= Approach flow Froude number

2.2 Regime Classification & Energy Dissipation

For an ideal dropshaft, the total energy loss should be nearly equal to the drop height. There is a strong correlation between the energy dissipation and the inflow jet impact location, which the flow regimes classified by. Because of the geometric simplicity, all possible jet impingement locations are just as follows; shaft pool, opposite wall, or outflow conduit upstream invert. However, the possible regimes and their classification become diversified due to the hydraulic complexity. Previous studies regarding comprehend the phenomena will be summarized below in chronological order.

Gayer (1984) investigated the local energy losses in dropshafts firstly. Losses were associated with a parameter containing the height of the drop and the flow velocity. Likewise, Christodoulou (1991) attributed local losses and pool depths to a dimensionless number called the Froude number F_0, which is essentially the same as that proposed by Gayer.

Chanson explored the hydraulics of the Roman dropshafts at the Hydraulic Laboratory at the University of Queensland. At low flow rates ($0.15 \geq d_c/L_s$), the free-falling nappe hits the shaft pool; Chanson classified this scenario as regime R1. Significant air entrainment is observed in the pool in this type of flow. When there is no backwater flow effect in the downstream channel, the flow is determined as supercritical. Regime R2 is classified for the situations where the discharge rate is larger and the jet impacts the outflow channel obvert. In R2, the energy dissipation rate is smaller; the free surface level of the pool increases substantially and less air entrainment is noticed. At large flow rates ($d_c/L_s \geq 0.30$), the free-jet strikes above the outflow channel (regime R3). The pool free surface climbs to the outflow conduit and the water level fluctuates significantly. R3, the third type of regime is common in modern dropshafts, which takes place only at large flow rates. Chanson stated that regime R3 is unlikely to be seen in Roman aqueducts (2000).

According to detailed acoustic measurements of Chanson (2003) with a 1:3.1 scaled model, the experimental observations assisted previous flow regime classification (2000). The energy dissipation rate was about 95% at low flow rates (Regime 1). The probability distribution functions of the particle residence times showed a bi-modal distribution in this flow regime. Some particles dipped into the shaft pool and quickly escaped to the outlet pipe. Others have been stuck in large-scale swirl structures for up to 20 minutes. The gap fraction measurements showed all flow regimes, but the shaft pool for the regime R2 was strongly aerated. The void fraction measurements showed that the shaft pool was strongly aerated for all flow regimes except for the regime R2. With an analytical solution of the air bubble advective diffusion equation for low flow rates, void fraction distributions were identified successively. Bubbly flow acoustic signatures showing some inconsistencies between model and prototype results, accurately characterized changes in the flow regimes of dimensionless bubble penetration depths and neutral particle residence times. These differences are believed to emphasize the limits of a Froude simulation for air entrainment, mass transfer studies and residence times in the dropshaft. In regime R3, the particles are sometimes entrained down the shaft pool but are rapidly escaped from the shaft (Chanson, 2003).

To advance the level of comprehension of the phenomena, de Marinis et al. (2007) performed a detailed analysis taking into account the additional factors determining the transition between the R1-R2 and R2-R3 regimes. The jet impact zone for the regime R2a is the region between the manhole outlet and the manhole base (*Figure* **2.2*d***). A portion of the discharge then flows directly into the downstream sewer, while the remaining circulates in the manhole pool, forming a roll on the jet axis above the impact zone. Two more lateral rollers close by the manhole outlet may be formed. In regime R2c, the upper part of the jet affects the sidewall of the manhole immediately above the outlet, while the lower part directly departs from the manhole (*Figure* **2.2*f***). The formation of a water curtain spread by the jet effect on the wall is observed. Because of these, the regeneration of R2b occurs when the jet directly impacts the outlet conduit (*Figure* **2.2*e***). Depending upon the approach flow Froude number, different forms of Regime 3 have also been proven by experiments. When the jet strikes against the dropshaft wall, the streamlines that are affected by gravity progress a vertical veil, and the veil covers the shaft outlet (Regime R3a). If the number of Froude increases, the water veil spreads radially and a small roll formation is observed above the jet impact zone (Regime R3b).

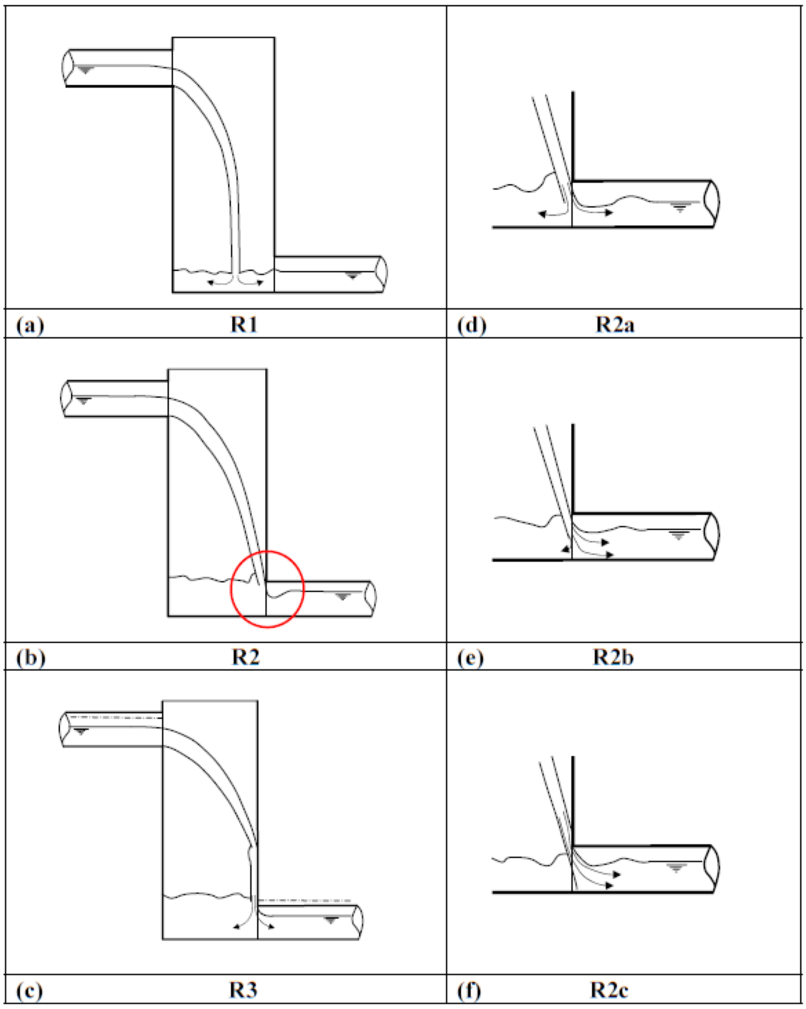

Figure 2.2 Jet impact locations and flow patterns (de Marinis et al., 2007).

As introduced previously, flow regimes significantly affect energy losses. According to the results of de Marinis et al., (2007), for the regime R1 energy losses reach nearly 96%, so almost all of the kinetic energy is dissipated by the R1 regime's physical conditions. Energy losses of approximately 82% were observed in the regime R2b. Regime R3 initially tends to increase in energy loss, probably due to higher F_0 values, which include a larger roller on top of the water veil. As the Froude number F_0 increases, the vertical water veil of regime R3a returns to another shape of a water veil, which spreads radially (R3b). The impact zone of the water veil expands at the manhole outlet, which includes the entire perimeter of the shaft bottom. *Figure* **2.3** shows that the data for the R1 and R2 regimes followed a similar curve, while the data were placed along divergent curves for the R3 regime, by a specific filling rate characterization. The approach flow conduit-filling ratio y_0 is defined as h_0/D_{in}.

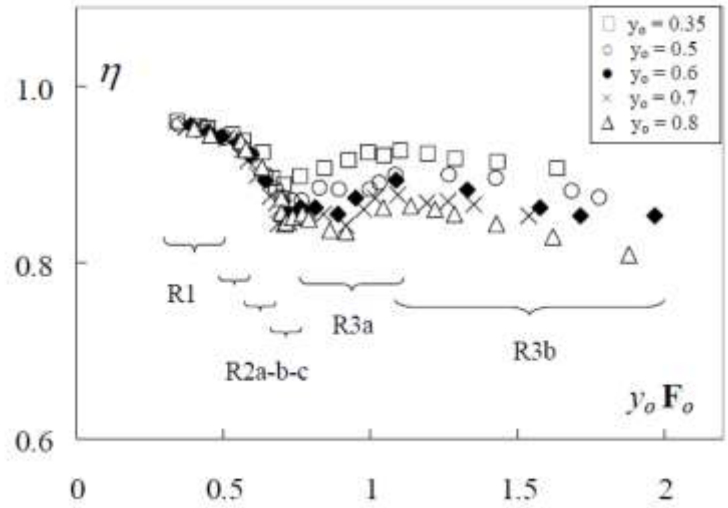

Figure 2.3 Dimensionless parameter y_0F_0 with the relative energy head loss η (de Marinis et al., 2007).

$$\eta = {}^{(H_0 - H_d)}\!/_{H_0} = 1 - {}^{E_d}\!/_{(E_0 + s)} \qquad 2.1$$

Granata et al. (2009) made further studies to uncover the energy dissipation mechanisms. It is claimed that dissipation is interrelated with an increase in flow turbulence, jet spread and shaft bottom jet impact. Concerning the production of turbulence, the energy distribution is mainly due to the impact losses on the manhole walls and bottom. Furthermore, if the incoming jet affects the counter wall, the dissipation is also propagated by the jet spread. In cases in which the free-falling jet hits downstream inlet, almost all the incoming discharge flows into the downstream conduit, and the through flow is influenced by a less diffusive effect. These conditions can result in unsatisfactory operations with unexpected characteristics of downstream flow. Besides, the effect of the height of the drop and the shaft diameter is also a significant issue, indicating that the decrease in the drop height decreases the relative energy loss. Also, as the shaft diameter decreases, the relative energy dissipation tends to be increased. Granata et al., (2009) discovered the relation between the energy dissipation and the shaft working conditions, the phenomena defined by an impact number that refers to the flow regimes. The flow regimes with a Froude type $F_I = V_0/(gD_M^2/2s)^{0.5}$ impact number I is

$$I = \left(\frac{2s}{g}\right)^{0.5} \frac{V_0}{D_M} \qquad 2.2$$

Where g is the gravitational acceleration and V_0 average approach flow velocity. The impact number stands for both the dimensionless drop height $S = s/D_M$ related manhole geometry and for the velocity head $V_0^2/(2g)$ type expressed approach flow properties. The impact number margin for regimes R1-R2 is 0.6, for regimes, R2-R3a is 0.95~1, and for regimes, R3a-R3b is 1.5.

$$\eta = 1 - \frac{E_d/s}{(E_0/s + 1)} = 1 - \frac{0.05 + 1.5\,E_0/s}{E_0/s + 1} \qquad 2.3$$

Equation (2.3) (a nondimensionalized form of Equation (2.1)) points out that corresponding to maximum downstream heads decreases as E_0/s increases.

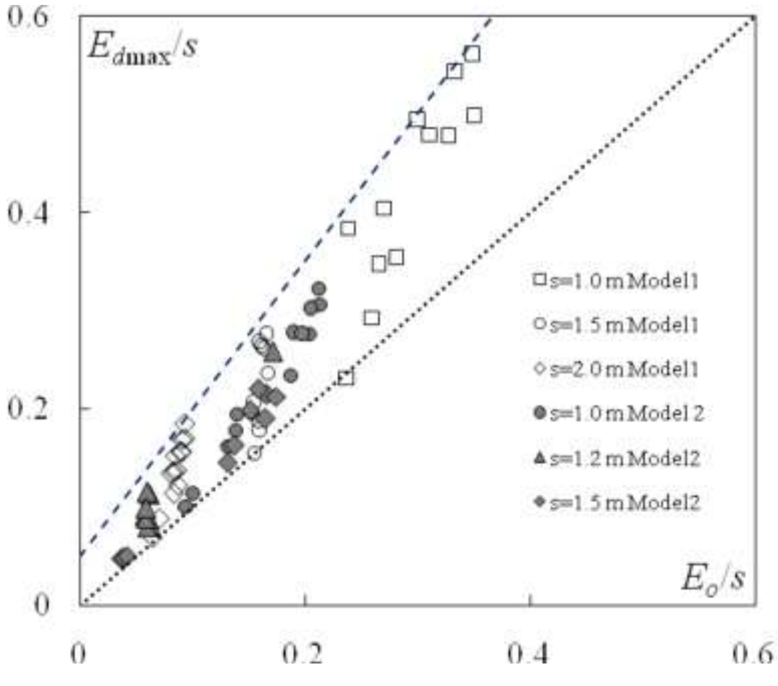

Figure 2.4 Maximum observed downstream energy head E_{dmax}/s versus E_0/s for various drop heights and manhole diameters, (---) Eq. (2.3), (···) $E_{dmax}/s = E_0/s$. (Granata et al., 2009)

As shown in *Figure 2.5*, Granata et al. (2010) showed that the depth of the pool increases with the impact number. In the R1 regime, the height of the pool is not affected by the upstream filling rate. In the R2 regime, the height of the pool increases, while slight differences are observed in regime R3a. Besides, a remarkable increase is seen in the R3b regime. The effects of the approach flow depth h_0 and jet shape gain importance during the transition from the R2 to R3 regime. For a given I value, the depth of the pool increases with h_0.

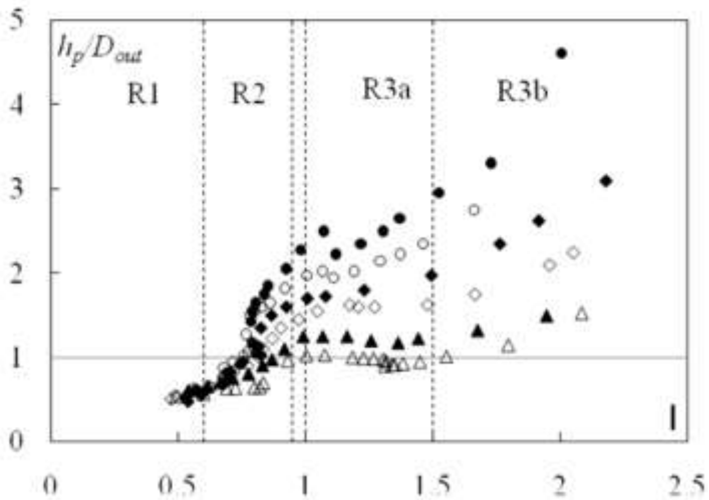

Figure 2.5 Pool height h_p/D_{out} versus I for D_M= 1.0 m, s = 2.0 m, jet-box opening (⌂) 30%, (▲) 40%, (◊) 50%, (♦) 60%, (○) 70%, (●) 80% (Granata et al., 2010)

Considering the momentum for the R1 and R2 regimes, it can be shown that the h_p/D_{out} the ratio depends on the ratio of $Q^*/y_0^{0.7}$, where $Q^* = Q/(gD_{out}^5)^{0.5}$ is the Froude number of the manhole. Analysis of test data for R1 and R2 regimes tends to fit Equation 2.4. While the manhole is operating under the regime of R3 (normally h_p/D_{out} > 1.3), the outflow of the manhole outlet resembles the orifice flow. With data analysis and energy considerations, R3 tends to fit Equation 2.5.

$$^{h_p}\!/_{D_{out}} = 0.3 + \left(1 + {}^{s}\!/_{D_M}\right) {}^{Q^{*2}}\!/_{y_0^{1.4}} \tag{2.4}$$

$$^{h_p}\!/_{D_{out}} = 0.6 + \left(7.3 - {}^{D_M}\!/_{D_{out}}\right) Q^{*2} \tag{2.5}$$

As evidenced by the experimental indications, choking usually occurs in the R3 regime. However, if the s/D_{out} the ratio between the outlet diameter and the drop height is less than 3 to 5, choking may occur in the R2 regime. Approach flow Froude number F_0 (Hager, 1999) and the approach flow filling ratio y_0 affects the downstream flow choking as shown by experiments. The inception of choking is described by a new parameter ψ where F_{och} refers to approach flow choking Froude number. Choking inception points are fit for 0.3 < y_0 < 0.75 by (*Figure* ***2.6***)

$$\psi = y_0\left[F_{och} - \left(h_p/D_{out}\right)\right] \qquad 2.6$$

$$\psi_{ch} = -5.9.y_0 + 3.5 \qquad 2.7$$

Equation (2.7) divides the plane (y_0,ψ) into a “no choking zone” and a “choking zone” (*Figure* ***2.6***), considered for aerated manhole flow is provided. Equation (2.7) stands for the verification of the downstream of a manhole choking risk (Granata et al., 2010).

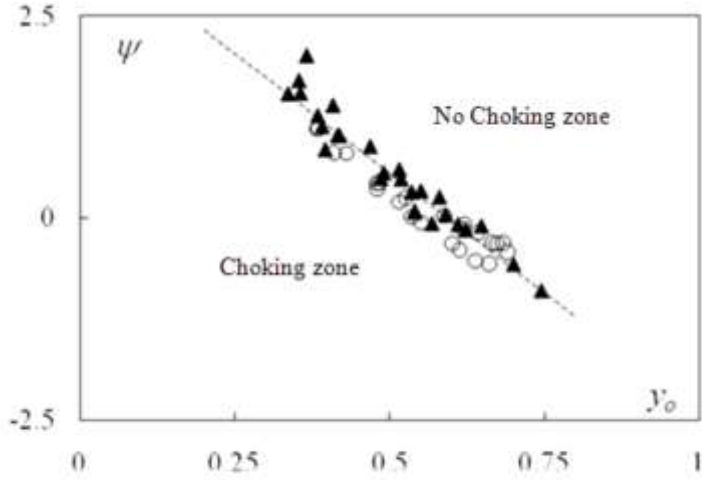

Figure 2.6 Choking inception from (▲) Model 1, (○) Model 2, Eq. (2.7) (- - -) (Granata et al., 2010)

Camino (2011) investigated stacked drop manholes in her doctoral thesis. Considering the design, classified four different regimes were related to the specific geometry of the manhole and water depths in chambers (*Figure* ***2.7***). While the first regime achieved energy dissipation at an average of 86%, the second regime reduced about 70%. The third and fourth regimes dissipated to an average of 56 % and 45 % of total energy, respectively.

The Froude number at the inflow does not seem to have a notable impact on energy loss, as opposed to the single drops. However, for a given Froude number, a reduction in energy losses can be observed with increased discharge. Inflow and outflow energy head component’s deeper assessments demonstrate that the incoming

Froude number F_0 is less than about 3, the total head of inflow is the piezometric head, taking into account the data at the invert of the outlet pipe. Then the piezometric head is roughly constant at the drop height level. As the approaching momentum increases, the incoming kinetic energy gains importance. For example, the velocity head is as big as the piezometric head for Froude numbers F_0 greater than five (Camino, 2011).

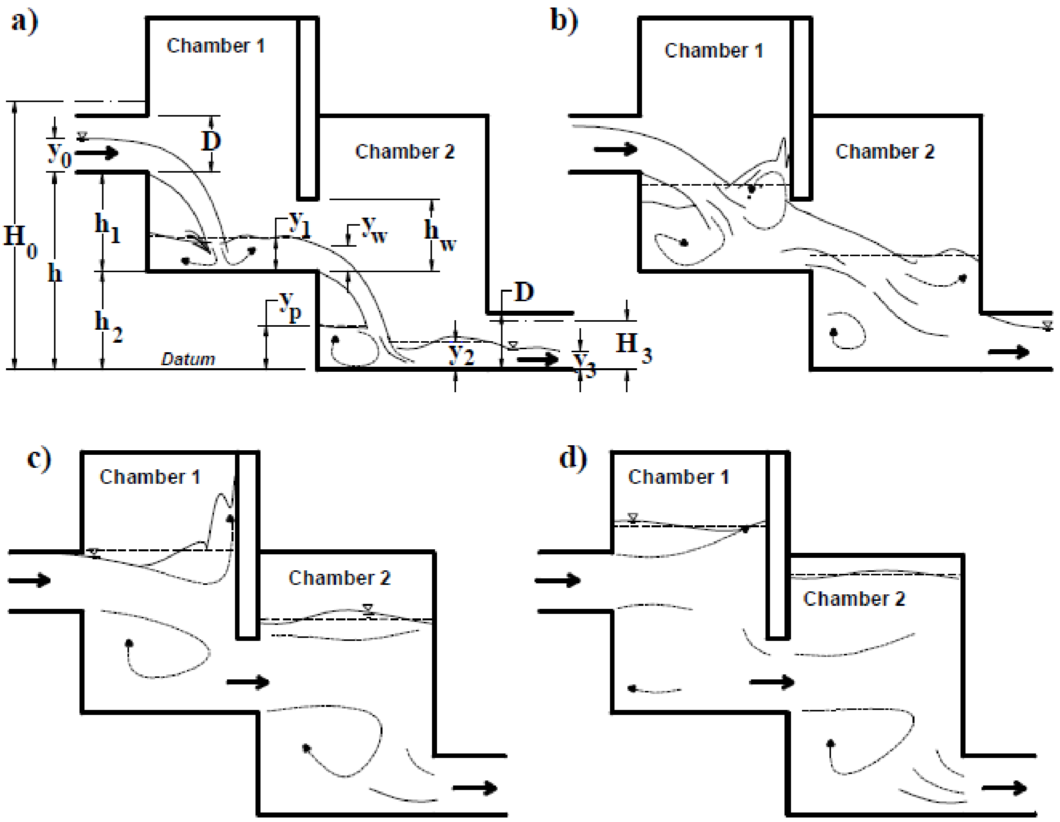

Figure 2.7 Flow regimes in SDM: a) Free overfall; b) Surface jet 2; c) Submerged sharp-edged opening; d) Fully submerged (Camino, 2011)

Granata et al. (2014) carried an experimental study on the effect of two different jet-breaker devices to dissipate excessive energy. The first device named the plane jet breaker (PJB) is designed to disperse the jet under the regime R2. For practical and operational reasons, it consists of a flat beam, which is properly positioned in the diameter plane perpendicular to the direction of the approach flow pipe. The second device, named wedge jet breaker (WJB), increases the energy dissipation by jet separation to prevent direct jet shock on the outflow conduit invert. WJB is placed just below the inlet so it affects the approach flow under nearly all operating conditions.

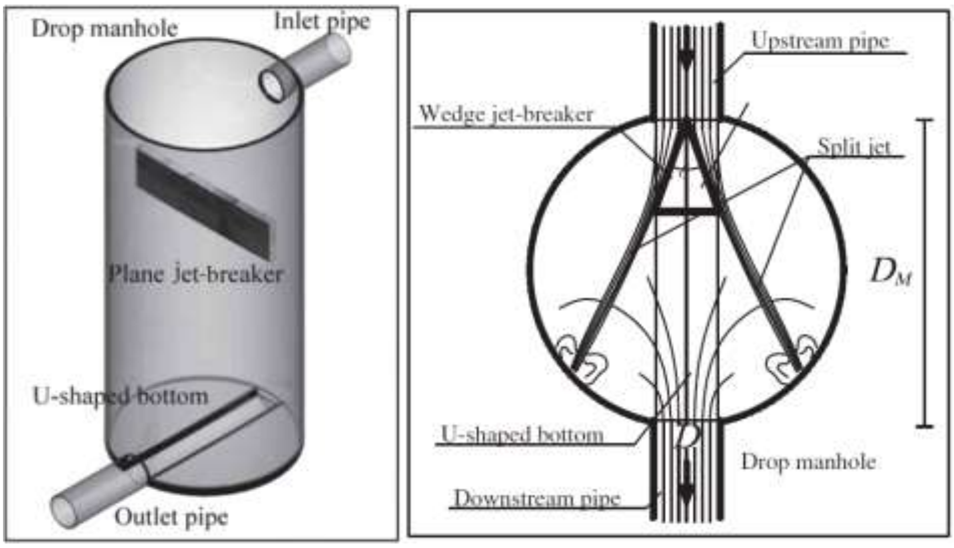

Figure 2.8 Jet-breaker elements: (a) PJB and (b) WJB (Granata et al., 2014).

The experimental studies of Granata et al. (2014) showed that the PJB presence does not affect R1 regime flows. The pool depth is slightly affected by PJB (*Figure* **2.9**).

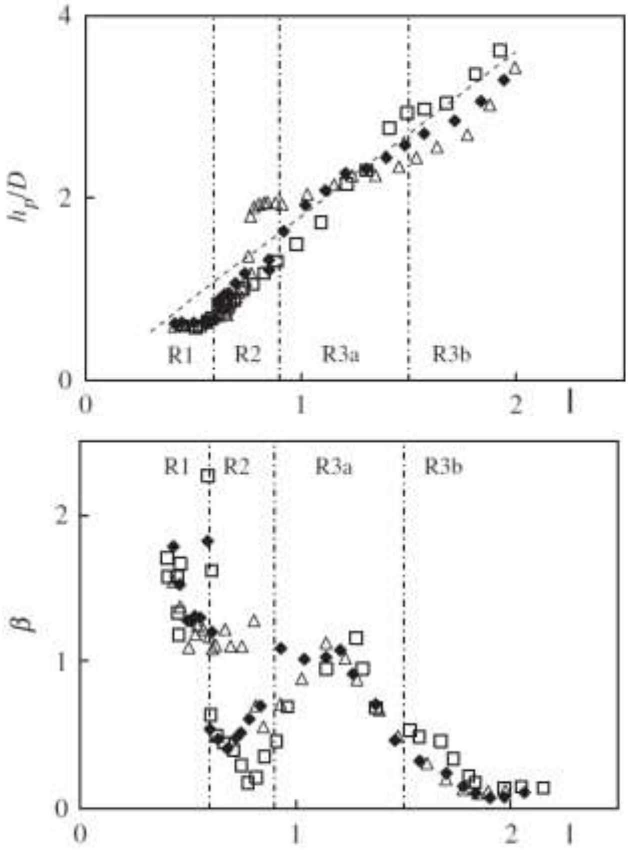

Figure 2.9 y_0 = 0.7 for upper figure, y_0=0.5 for below figure: (⌂) without jet-breaker, with (♦) PJB1, (□) PJB2 and (- - -) $h_p/D = 1.9I$ (Granata et al., 2014).

A PJB significantly affects the relative air demand $\beta = Q_a/Q$ (*Figure 2.9b*), in which Q_a is the air discharge supplied by the atmosphere. During the transition from R1 Regime to R2a Regime, the free-falling jet impacts the PJB in such a way that it causes a significant splash and additional drops with entrained air as it falls. However, under R3 Regime conditions, PJB does not affect the interaction between water and air, β is not significantly affected by the presence of PJB. The choice of a jet-breaker element should take into account the practical considerations and the risk of clogging. These aspects support the PJB, which prevents the manhole outlet from the plunging jet effect. Regarding hydraulic and practical aspects, an appropriately dimensioned PJB arises to be a useful improvement (Granata et al., 2014).

Based on pattern recognition and computational learning theories, many topics can be addressed through machine learning algorithms. Granata & de Marinis used the algorithms to investigate the energy dissipation in the drop manholes. The M5P model provided a good estimation power, while the Bagging algorithm could not bring enhancements, unlike Random Forest. All the algorithms considered are effective approaches. Concerning air entrainment, only the Random Forest algorithm performed good predictive power among the others. Finally, by referring to predicting lateral outflow discharge rate along the side weir, Bagging and Random Forest did not bring improvements to the excellent predictive capability shown by the M5P. The algorithms discussed were compared with more classical models. Investigated algorithms showed greater accuracy and complexity (Granata & de Marinis, 2017).

Seven experimental series under various outflow conditions were carried out by Zheng et al. (2017) to inspect the energy dissipation in circular manholes. The first three series were operated by the non-pressurized flow in the outflow pipe. In the fourth series, experiments were operated to investigate the sudden transition from free surface to pressurized flow, i.e. outlet choking. Series 5-7 were run at the restricted outlet conditions where the back pressures were applied to the outlet flow from the downstream pool. Zheng et al. indicated a large dissipation effect in the choking flow, which means that the energy dissipation of the manhole is substantially increased when the outlet pipe free surface flow shifts to the pressurized flow. This can be explained by the strong mixing mechanism between the water and entrained airflow in the outlet pipe; this can be demonstrated by a notable increase in Q_a/Q as the dimensionless air demand. After the flow in the outlet pipe is choked, large inconsistent fluctuations occur on the surface of the pool water indicated by a sudden decrease in the height of the shaft pool and by large standard deviations. Based on the experimental observations of Zheng et al., different forms of the free fall nappe were seen before the impact. The sides of the nappe form a "centre ridge" when a shaft with a large drop height with low flow rates, and the nappe is usually horseshoe-shaped for small drop heights or higher flow rates (Zheng et al., 2017).

In another aspect, Ma et al., (2017) proposed four basic flow regimes in dropshafts (*Figure* **2.10**): Regime I, free fall flow; Regime II, orifice flow; Regime III, pressurized outflow; and Regime IV, fully submerged condition. Regime I is similar to the free flow of a drop occurring at a relatively low flow rate (*Figure* **2.10***a*). In Regime II, the outflow inlet is submerged in the shaft, while the outflow is not, similar to the orifice flow conditions (*Figure* **2.10***b*). In regime III, the outflow conduit is full and the outflow is pressurized (*Figure* **2.10***c*). In regime IV, the pool surface in the manhole exceeds the inflow pipe inlet, which means the inflow submergence. (*Figure* **2.10*d***). While Regimes II, III and IV are controlled by the flow conditions of the downstream side, Regime I can be interpreted by upstream flow conditions. This type of classification causes the performance of the dropshafts and the associated energy dissipation from a different perspective and bypasses the detailed progress of energy dissipation conditions. It is more appropriate to evaluate the theoretical energy dissipation estimation based on this classification.

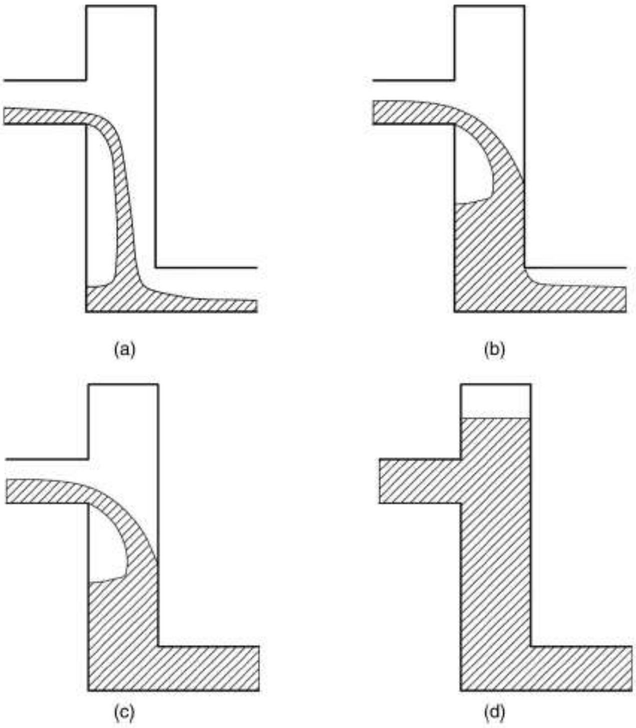

Figure 2.10 Regimes in a drop manhole: (a) I, free overfall flow; (b) II, orifice flow; (c) III, pressurized outflow; (d) IV, fully submerged manhole condition (Ma et al., 2017)

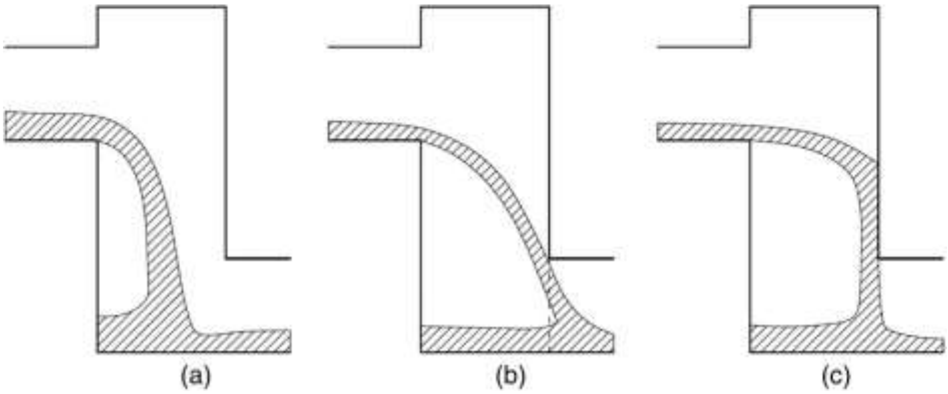

Figure 2.11 Subregimes of Regime I: (a) IA, $I < 0.6$; (b) IB, $0.6 \leq I \leq 1.0$; (c) IC, $I \geq 1.0$ (Ma et al., 2017)

Ma et al. (2017), proposes conservative designs, which can be carried out with the operations under Regime I or II with a design discharge. Considering the desire for economic efficiency, manholes can be designed to work in Regime III in the design discharge. In all four regimes, regime IV may cause choking problems and must always be avoided due to the risk of possible adverse effects of the sewage system operations. Criteria for distinct regimes are defined quantitatively:

1. Free overfall for $Q/(gD_1H^4)^{0.5} < 1.5(D_2^2/(HD_m))^{1.56}$,
2. Orifice flow for $Q/(gD_1H^4)^{0.5} \geq 1.5(D_2^2/(HD_m))^{1.56}$ and $Q^* = Q/(gD_2^5)^{0.5} > 0.90$,
3. Pressurized outflow for $Q/(gD_1H^4)^{0.5} \geq 1.5(D_2^2/(HD_m))^{1.56}$, $Q < C_dA_2(2gH)^{0.5}$, $Q^* \geq 0.90$ & $C_d = 0.64$,
4. Fully submerged condition for $Q \geq C_dA_2(2gH)^{0.5}$ & $C_d = 0.64$.

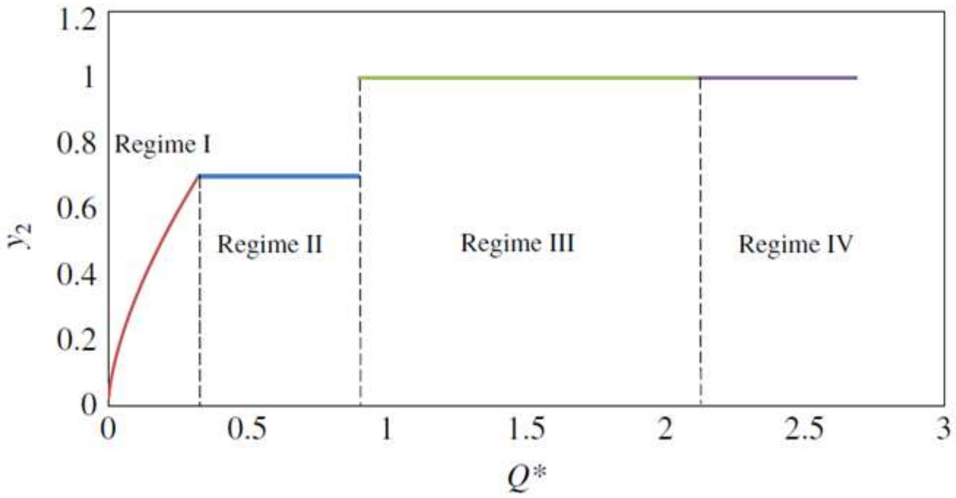

Figure 2.12 Outlet pipe filling ratio y_2 and flow regimes changing with dimensionless flow rate Q^* (D_M=1.0 m, H=2.0 m, $D_{in} = D_{out}$ = 0.2 m, with a nearly horizontal outlet pipe) (Ma et al., 2017)

2.3 Air Entrainment

A considerable amount of air can be entrained by plunging water. The demanded bulk air by a dropshaft is a product of the combined action mechanisms of air entrainment, air movement and air release. Air bubble entrainment may occur due to local or continuous operations along with the air-water interface. The bubbles are locally entrained at the impinging jet intersection (Chanson, 2004). In drop structures, both the continuous and local air entrainment processes are common (Falvey, 1980;

Rajaratnam et al., 1997; Granata et al., 2011; Gualtieri & Chanson, 2013). Different behaviours of the investigated various drop structures may stem from the disintegration of the inflow into drops with large drop heights. The water drops increase the interaction between the air and the water, leads to a huge amount of air entrains into the dropshaft. The entrapped air may cause the air pressure in the head gap of the downstream conduits and the odour complains when the sewage odour escapes from the sewage systems (Edwini-Bonsu & Steffler, 2006; Zhang et al., 2016). Therefore, a better understanding of the air movement in the shafts is needed in sewage ventilation and odour control. The main types of air entrainment mechanisms are (1) entrainment by the vertical shaft wall jet impingement, (2) drag of air by the water streams and falling drops, (3) plunging flowing into the pool bottom and (4) turbulence of the flow (Ma et al., 2016). Researches on air entrainment in different height drop structures indicate that a greater drop height leads to higher relative air demands (i.e., the ratio of air in water flow). Relative demand of air was recorded as 1.4 from a dropshaft with 2.1 m in height (Rajaratnam et al., 1997), 40 from a dropshaft with a height of 7.72 m drop (Camino et al., 2015) and 160 from a prototype dropshaft with an approximate height of drop with 22m. The rate of average energy dissipation was over in a dropshaft with 7.72 m in height as 80% (Camino et al., 2015).

Besides, since the manholes are sealed to prevent odour from the sewage system (Ma et al., 2017) and this, unfortunately, increases the risk of choking (Granata et al., 2015). Compared to the dropshafts, the mechanisms associated with air entrainment may not be important because of the smaller drop height of the SDM. However, the relative contribution can be significantly increased when the outflow conduit is partially filled. In these types of cases, the inflow of water drives an airflow in the outflow conduit (Gargano et al., 2008).

Chanson (2003) carried out detailed air-water two-phase flow and acoustic measurements on the prototype dropshaft with a 1: 3.1 scale model under controlled flow conditions. The experimental data distribution was well-matched with an analytic diffusion equation solution for air bubbles. The equation of the two-dimensional free falling plunging jet is as follows:

$$C = \frac{1}{2}\frac{Q_a}{Q}\frac{1}{\sqrt{8\pi D^{\#}\frac{z}{d_i}}}\left(exp\left(\frac{-1}{2D^{\#}}\frac{\left(\frac{x-x_i}{d_i}-\frac{1}{2}\right)}{\frac{z}{d_i}}\right)+exp\left(\frac{-1}{2D^{\#}}\frac{\left(\frac{x-x_i}{d_i}+\frac{1}{2}\right)}{\frac{z}{d_i}}\right)\right) \qquad 2.8$$

Where Q_a is the airflow rate, x_i is jet impact coordinate, d_i is the free-jet thickness at impingement location, $D^{\#}$ is the dimensionless air bubble diffusivity. Chanson indicated that the data measurements were collected in the fully developed flow region (i.e. z/d_i > 10).

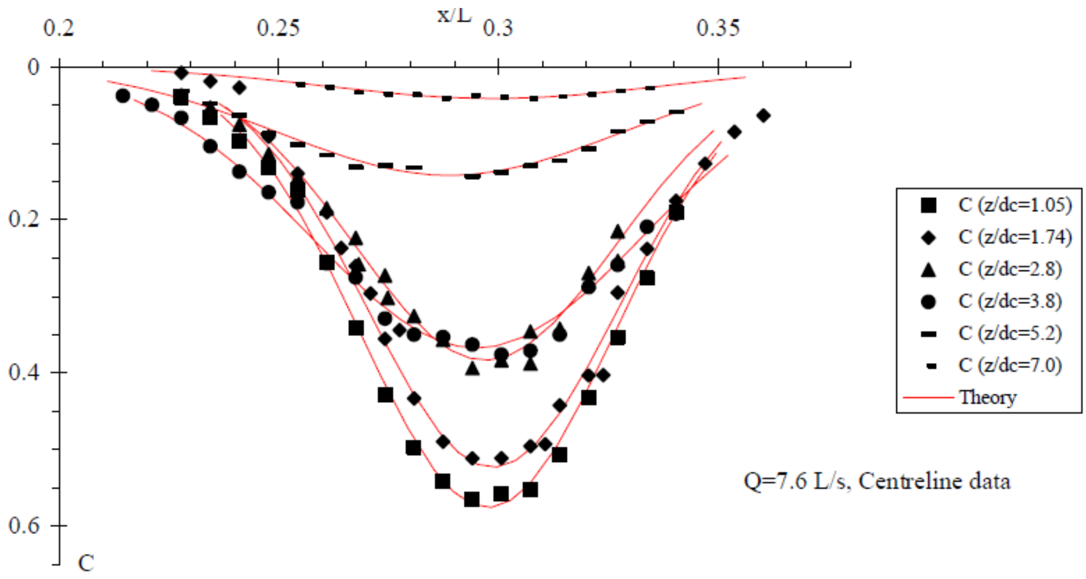

Figure 2.13 Air concentration distributions below the free surface of the pool in the shaft centreline - Prototype data for d_c/L_s= 0.017 (Regime R1) - Compared with Eq. (2.8) (Chanson, 2003).

Chanson made further investigations with similar experimental models in 2007. Four rectangular dropshaft configurations were systematically investigated to examine the effects of the pool depth and the outflow direction on air entrainment and particle residence times. The shaft configurations with deep pools were characterized by 4 to 8 times longer residence times compared to the shafts without a pool. The design with optimum progress was at low flow rates (regime R1) with a deep pool shaft (Model A) having a 180° direction of outflow. A full-scale study with a ratio of 3.1:1 was performed for Model A. However, similar trends were observed in both prototype and model, scale effects were seen in terms of bubble swarm depths and particle residence times. The results of the model overestimate bubble penetration depth $D_{ab}/(y_p + P)$ and the dimensionless residence time $T * V_c/d_c$. Some differences were noted in the outlet channel between the spray and bubble flow zones. In the first, there was no preferred droplet size associated with cluster structures. The drop formation is caused by surface distortion, interactions between eddies and free surface and tip streaming of ligaments. The dominant effect of the droplet ejection process is likely because the response time of droplet is almost two sizes that are not of a preferred size for droplet ejection (Chanson, 2007).

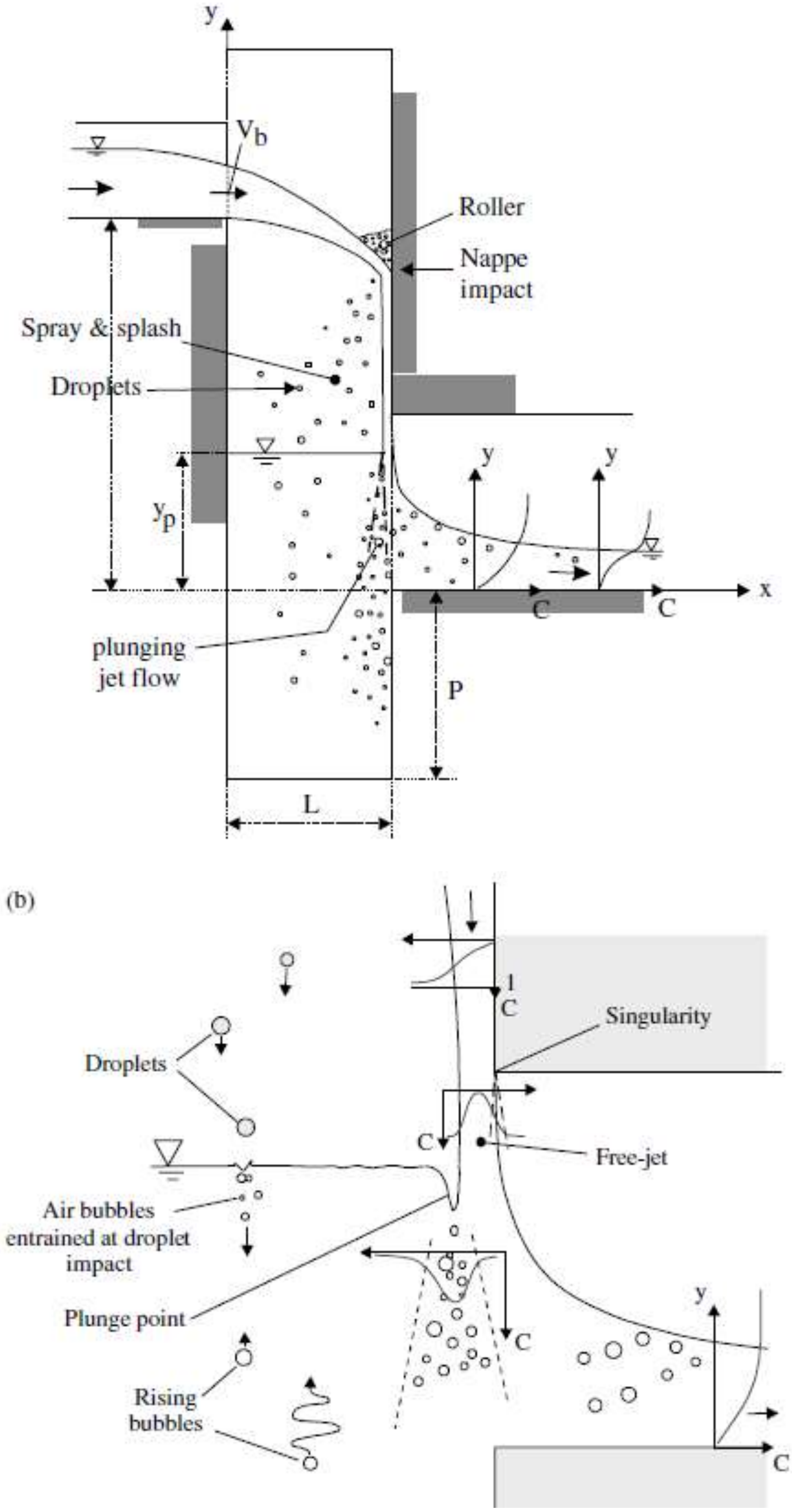

Figure 2.14 (a) Nappe impact onto the opposite wall. (b) Air entrainment processes next to the outflow channel obvert (Chanson, 2007).

Granata et al., (2011) indicated typical results of dropshaft air demand measurements and air entrainment mechanisms (*Figure 2.15*), the ratio β between the air discharge Q_a and the incoming water discharge Q, against the impact number I). It is claimed that only a portion of the entrained air is carried in the downstream conduit. This represents the actual demand for air from the outside of the shaft. By some detrainment mechanisms, the remaining part is released and recirculated in the dropshaft. The mentioned mechanisms are caused by the buoyancy in the bottom pool, the effect of the air-saturated jet at the opposite wall and the turbulent eddies in the air-water interface. The eddy formation at the air-water interface both causes detrainment and entrainment of air bubbles. A small diameter recirculation pipe is examined to be an effective solution to reduce the effects of a lack of aeration, but the result was unsatisfactory. The study indicated that urban sewerage systems need proper ventilation not only for the aerobic condition maintaining within the system, but also to avoid poor hydraulic conditions.

Choking factor ψ and impact number I are effective dimensionless parameters in recognizing the dropshaft performance in both the absence and presence of aeration. The maximum air demand is mainly affected by manhole geometry and incoming flow kinetic energy. Absent or inadequate air supply may cause negative pressure heads, which may reach 60% of the height of the manhole. It is noted that the effects of diameter seem inappreciable. Negative pressure can cause a significant increase in pool depth. For a small height of drops, a pool rise above the manhole inflow elevation can cause undesirable backflow effects to the upstream sewer.

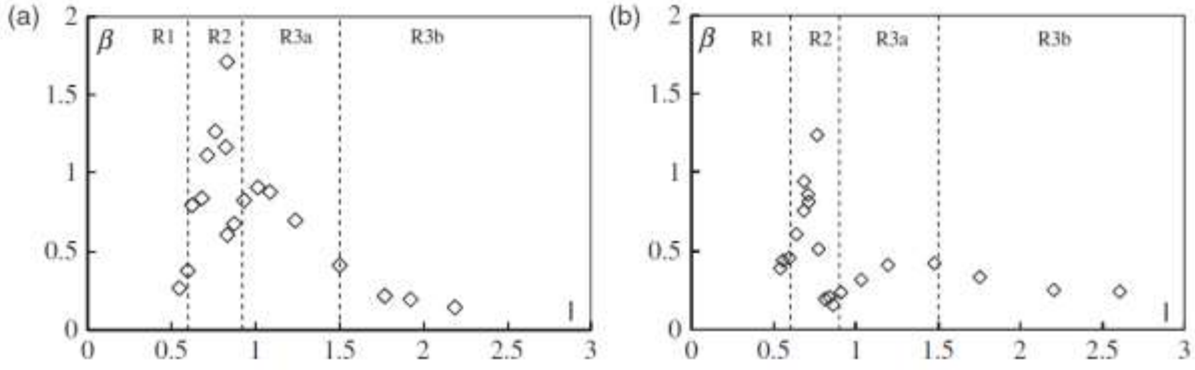

Figure 2.15 Relative air demand β versus impact number I; a) Manhole diameter D_M = 1.0 m, drop height s = 2.0 m, approach flow filling ratio y_0 = 0.6; b) D_M = 0.48 m, s = 1.0 m, y_0 = 0.45.

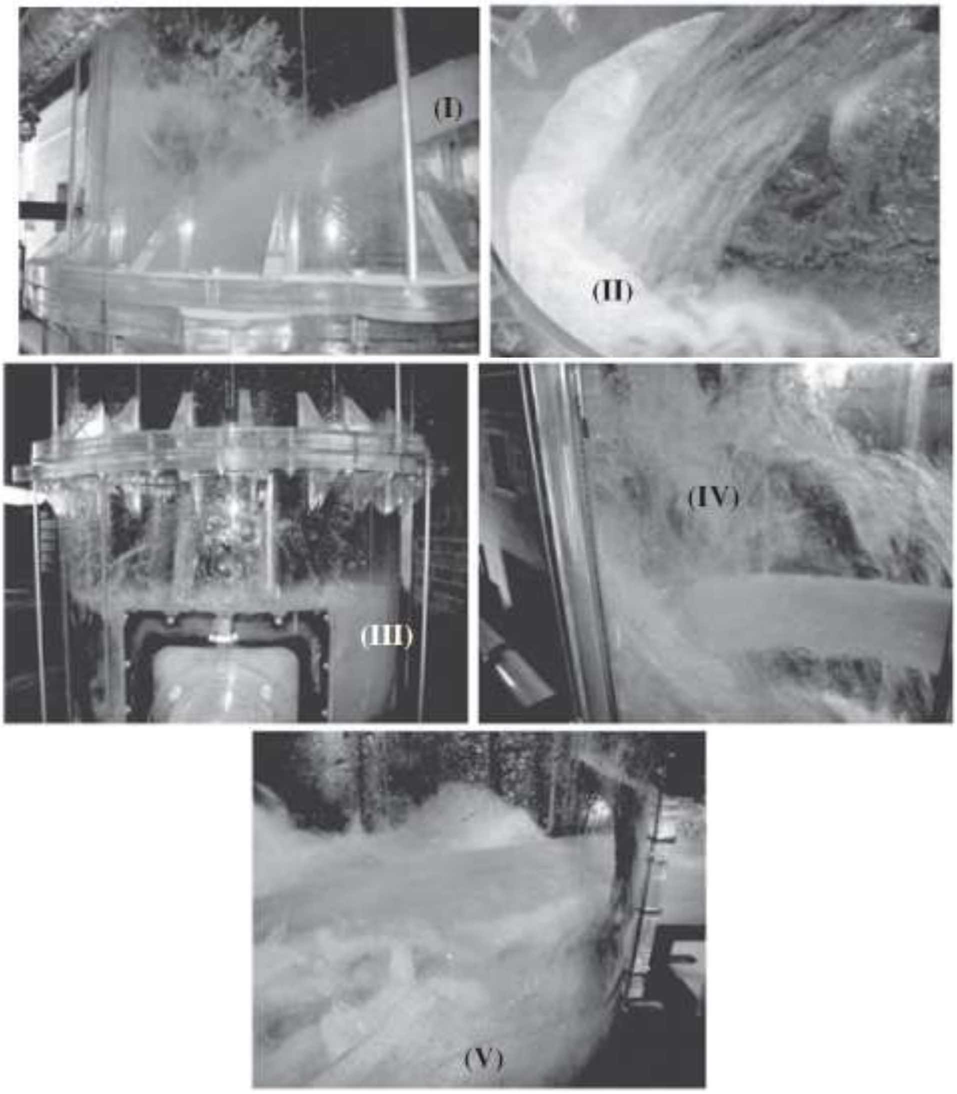

Figure 2.16 Air Entrainment Mechanisms (Granata et al., 2015)

The following air entrainment mechanisms (AEMs) can be recognized:

I) the entrainment by the inflow originated free-falling jet;

II) By the plunging jet into the bottom pool, in the cases without jet impact on the opposite manhole wall;

III) by mechanism due to the water veil flowing along the manhole wall, which follows the jet impact against the opposite wall and plunges into the pool bottom through the boundaries;

IV) Due to the jet split originated droplets;

V) By the fluctuation originated surface entrainment mechanism.

Base shape effects may also be important for aeration. For production and sanitary requirements, there is usually a semi-circular channel at the bottom of the manhole. This configuration of the base affects the air entrainment in the R1 and R2a regimes where AEM I, AEM II and AEM V are common. *Figure 2.17* indicates the typical trends of the relative air demand (β) against the impact number I for a semicircular channel bottom (U-shaped). The significantly higher values of β than the values determined for the plane bottom cases are observed in the R1 and R2a regimes. Because of the droplet formations due to the splashing jet impact on the bottom. However β is notably higher under Regime R3a, the existent air demand is supposed to be lower than the observation (Granata et al., 2015).

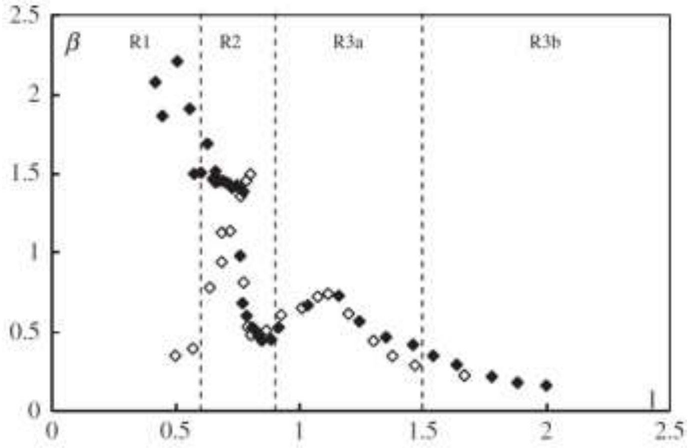

Figure 2.17 Relative air demand β versus impact number I, (◊) plane bottom and (♦) U-shaped bottom, s = 2m, y_0 = 0.7. Granata et al., 2015

Ma et al., (2016) studied the air entrainment mechanism in a dropshaft using a physical large-scale model with a height of 7.7 m. The drop size distribution analysis indicated that the dominant drop size was about 2 mm. The drop size distribution sensitivity analysis for the effect of the drop numbers showed that the distributions obtained from 60, 120, 240 and 300 drops were similar. At different heights and flow rates, an average velocity of about 6 m/s was found for drops. The drop distance required in the shaft to disintegrate the water into the drops was estimated to be approximately 2.6-5.5 m at different water flow rates. The height was affected by the equivalent diameter of the water jet and the water flow rate. By reducing the water jet equivalent diameter, the inflow impingement at the shaft wall accelerates the breakup of the water flow (Ma et al., 2016).

Wei et al., (2018) examined a slender tall dropshaft with a divider to investigate the internal and external air movement under altered boundary conditions. Experimental results were reported in three main cases as the original operating condition, pressurized outflow conditions and reduced air inlet conditions. Under the case of the original operating condition, the air pressure was negative under all test water discharges in the wet shaft and the amount of the negative pressure increased by the water discharge. The average pressure under the original case was nearly constant at the higher section and then increased linearly to the bottom. An air pressure drop due to the obstruction of the air passage was observed nearby the inflow impinging area within the wet shaft. The empirical relationship between this pressure drop and the water flow rate was offered. Under pressurized outflow conditions, created by placing a weir in the outlet pipe, the air pressure in the wet shaft became higher and even indicated a positive outflow air pressure up to 0.28kPa. The outside air entrainment was decreased by more than 50%, in comparison to the original condition. The internal recirculation of the air has increased considerably and the total air demand with a pressurized downstream condition reached up to 0.78. The ratio of $(Q_a^c/Q_a^t)/(Q_a^I/Q_w)$ defines a correlation named as the ‘effectiveness factor’, was suggested to formulate the effective relation of the internal air circulation with total and relative air demand. Internal air recirculation was found to be more effective in decreasing entrained air of the dropshaft under a pressurized outflow condition, which occurs frequently in real situations. Under the reduced air inlet conditions, the amount of the circulated airflow rates were identified to be much higher than the ones under the original operating condition. The consequences of this study support the utilization of an internal divider within a dropshaft in sewerage systems. It also shows a considerable pressure drop at the impinging position and the base of the dropshaft. This provides significant information for future use in the design and implementation of dropshafts with an internal separator (Wei et al., 2018).

2.4 Related Studies Using the Same Code

Sousa et al., (2009) used Chanson's (2002) investigational data and the CFD code to simulate the plunging flow patterned rectangular dropshaft. k-ε and k-ε RNG turbulence options were assessed and the hydraulic parameters of the computation were found to be in a good fit range with the experimental observations. The results show that the CFD modelling of rectangular plunging vertical dropshaft hydraulics is feasible and useful in the evaluation of hydraulic parameters that are essential to provide data to the one-dimensional collection system modelling. Authors reported that using the k-ε models with the "true" VoF technique provides adequate flow feature representations and embedded multi-block feature helps to optimize the mesh, as a significant computational time-saving tool.

Movaheida et al., (2015) also utilized the code and designed a drop manhole, with a discharge of 6 m^3/s and a height of 3 m, at the downstream transmission line of a spillway. The authors reported that the results are consistent

A new vortex dropshaft deprived of air circulation holes has been proposed by Zhang et al., (2018), to overcome the negative pressure and cavitation erosion problems in vortex dropshaft spillways with height increment in aeration tunnel. The shaft is simulated using the code with the k- ε RNG turbulence model. The hydraulic properties of the vortex dropshaft are investigated by comparing the simulation and experiment results. The results of the study demonstrated that the k-ε RNG turbulence model has the capacity for effective simulation of the flow characteristics of the vortex type dropshafts. Including the pressure and velocity, hydraulic parameters were in good agreement and indicated the same trend with the experimental data. With the RNG k- ε turbulence model, hence, similar vortex problems can be simulated. The authors added notes about the limitations of the study as the need for more scale investigation in experimental and numerical simulations. Additionally, the diameters of the slope section, vertical shaft and vortex chamber are required to be optimized regarding existing commercial body sizes to designate the best dimensions (Zhang et al., 2018).

3 MATERIAL AND METHOD

In this section, a previously made experiment, with available data, will be introduced. Then the installation of the CFD model based on the conditions of the relevant model will be given.

3.1 Compared Previous Experimental Study

3.1.1 Geometry & measurements

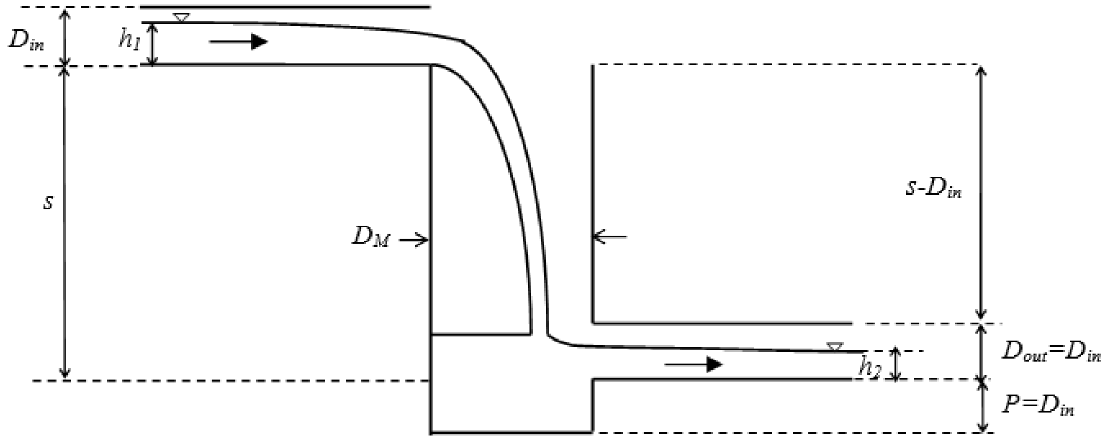

Figure 3.1 Definition sketch of the dropshaft used in the previous experimental model (Kumcu & Kokpinar, 2013)

The experiment was carried out in a setup as illustrated in *Figure* ***3.1*** at the Hydraulics Laboratory of the State Hydraulic Works (DSI), Ankara, Turkey. The main part of the experiment; the inflow pipe, the outflow pipe and the circular shaft were made in Plexiglas. In experimental (and numerical) modelling, geometric properties of the dropshaft are L_1=2 m, D_M=0.358 m, D_{in}=0.12 m and s=0.48 m, besides the slope effects, are not surveyed. The discharges were measured by a portable ultrasonic flow meter (Tokimec-UFP-10) having an accuracy of ±1% from a D_{in}=0.2 m diameter conduit located at the upstream of the scratched inflow pipe. The flow depths in the inflow and outflow pipes were measured with a point gauge of 0.1 mm accuracy. The experimental data were measured from the different shaft elevation points on the centreline cross-sections at, z1=0.1410 m, z2=0.1625 m, z3=0.2235 m & z4=0.2845 m. Three flow rates Q1=1lt/s, Q2=3lt/s and Q3=5lt/s are investigated for three different flow regimes with Impact Numbers (Granata et al., 2011) I1<0.45, 0.45<I2<0.47, and I3<0.47 consequently for R1, R2 and R3.

The air-water flow properties in the two-phase flow region along the dropshaft were measured using a fibre-optic instrumentation system with a sensitive double-tip probe to detect phase change in the high-speed flow region. The tip size of the sapphire probe was 80 μm, which was connected to an optical-electronic amplifier that provides light and emitted an electronic signal by converting optically reflected information. Signals were recorded in a quick acquisition panel (with 1 MHz sampling frequency & nearly 0.033 μs resolution), filtered and interpreted statistically. In each measurement, the signals were scanned for six consecutive measurements of 60 seconds and the data were averaged to obtain a time-based value (Kumcu & Kokpinar, 2013).

3.1.2 Application & results

The inflow and outflow pipes are operated as the free surface flow for all flow conditions studied. The downstream flow was supercritical while the upstream flow was run with a subcritical condition. It has been observed that the upstream flow condition is independent in the cases where the relative length of the pipe is (L_1/d) greater than 15. At low flow rates, the free-falling nappe impacts the shaft bottom as reported by Chanson (2002) (Regime R1, *Figure* ***3.2***a). In regime R1, air bubble entrainment in the shaft basin is observed. The flow in the downstream conduit was supercritical and shock waves were visible. For medium discharges, the free-falling nappe impacted the outflow pipe entrance compliant to the definition of Regime R2 (*Figure* ***3.2***b). Excessive flow instabilities were seen at the entrance of the outflow pipe and the entrained air in the shaft decreased significantly. With the high flow rates in the inflow pipe, the free jet impacted the opposite wall above the outflow conduit and fell with smaller particle sizes (Regime R3, *Figure* ***3.2***c). While a pair of jets were flowing over the wall surface, a fraction was disintegrated due to the splash and spread. During this process in the Regime R3, a considerable amount of air entrainment is observed.

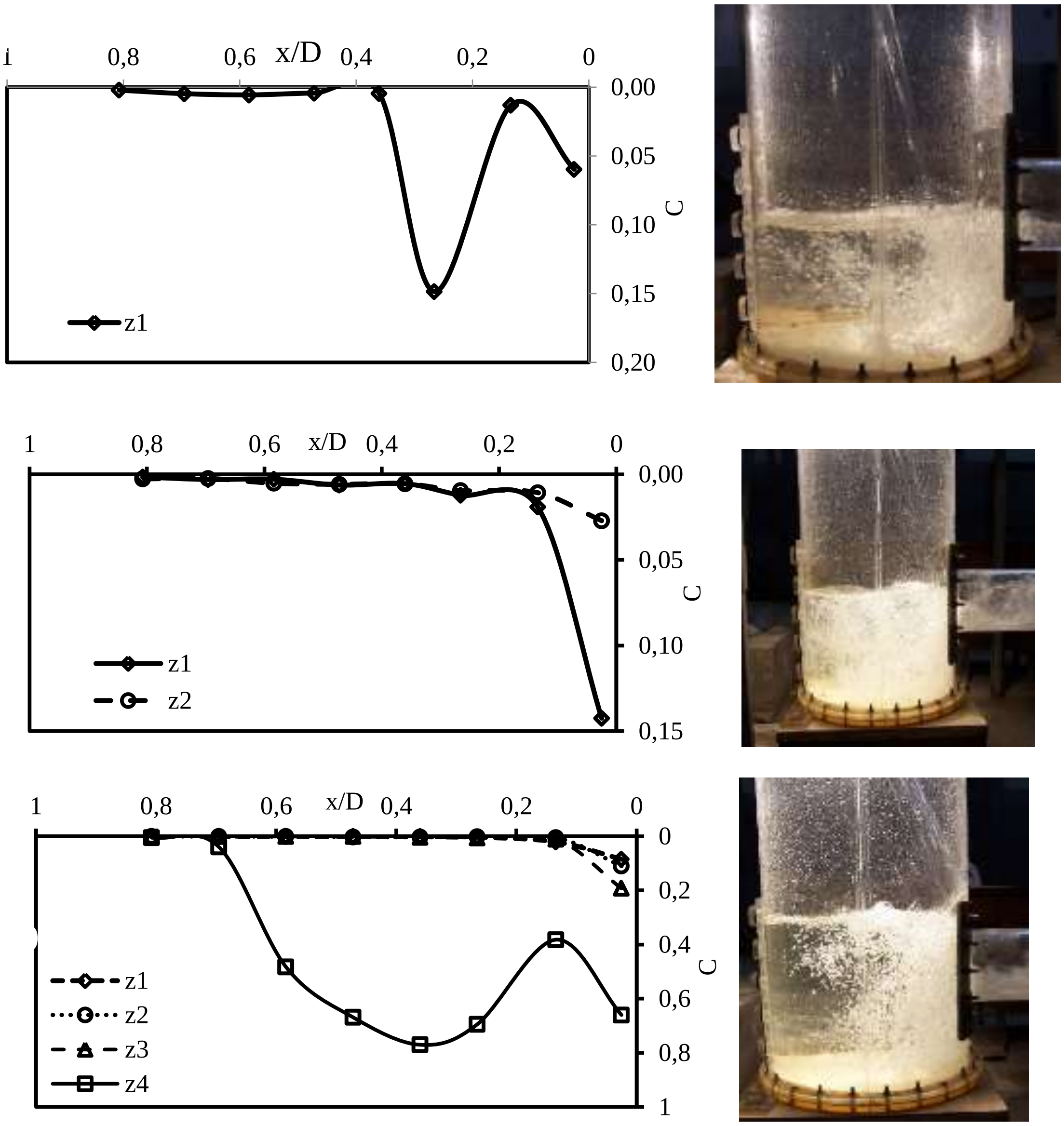

Figure 3.2 Void fraction (C) distribution beneath the pool at different elevations with different flow regimes a) Q=1.0 l/s (Regime R1), b) Q= 3.0 l/s (Regime R2) and c) Q=5.0 l/s (Regime R3)

Figure 3.2 shows images corresponding to the three different regimes (R1, R2 and R3) with relevant data distributions of the void fraction ratio. Highly aerated flow conditions were observed near the outflow pipe in all flow regimes. In Regime R1, the effect of the free-falling plunging jet appears on the void fraction distribution by making a peak away from the outflow pipe (*Figure 3.2*a). Measurements performed in the R3 Regime showed that there was a high void ratio beneath the free surface by splash and spread effect (*Figure 3.2*c). Since the plunging jet affects the inlet of the outflow pipe in the Regime R2, more air bubbles are introduced near the wall.

Energy dissipation in the shaft is observed and classified by various types of AEM’s. In R1 Regime inflow originated plunging jet and the impact to the bottom is the main dissipater agents AEM I, AEM II & AEM V as mentioned by Granata et al., in 2005. In the R2 Regime, the free jet leaving upstream conduit impacts directly into the outflow conduit invert, and limited aeration is seen. Regarding simple naked-eye observations, the dissipation of energy is logically low since the flowing energy of water is transferred from the inflow conduit to the outflow conduit without significant dissipation and AEM mechanism occurrence. For Regime R3, energy dissipation results from AEM I, AEM III, AEM IV & AEM V. Mainly from the jet impact onto the opposite wall and splashed droplets. As shown in *Figure 3.3*, in the R1 Regime, the energy dissipation, η has the highest value of about 0.75 and is decreasing with the increase of Impact Number, I. Then, at the transition to the R2 Regime, η sharply decreases from 71% to 66% and has the lowest value of 62% within the R2 Regime. At the transition to the R3 Regime, energy dissipation increased again to 66%, and then a gradual decrease to 63% with the increase of I is showed (Kumcu & Kokpinar, 2013).

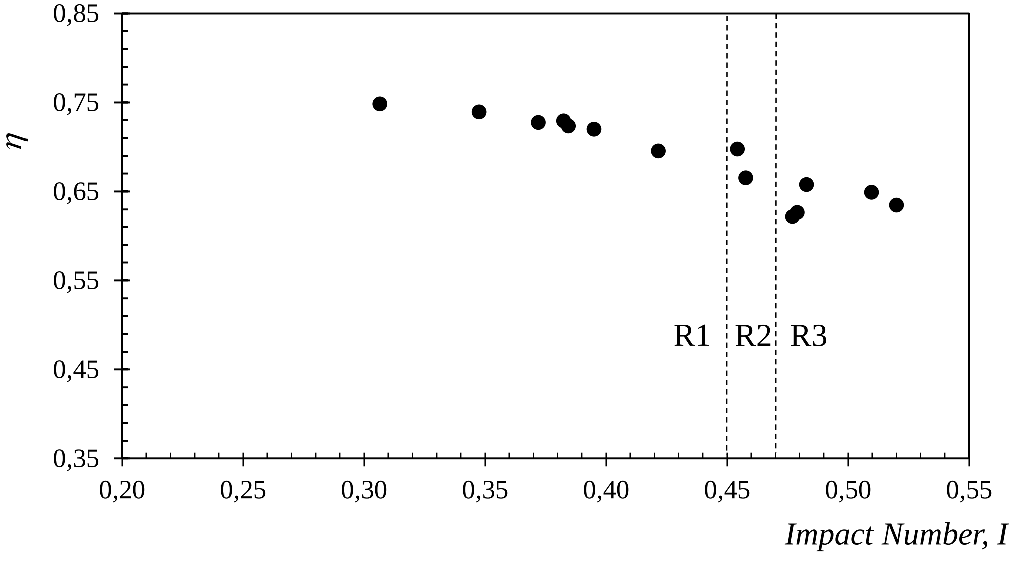

Figure 3.3 Effect of Impact Number on energy dissipation (Kumcu & Kokpinar, 2013).

3.2 Computational Fluid Dynamics

Although physical model studies are the most common and safe way to achieve realistic results, with almost perfect solutions in a range of scale limitations, the physical model has some disadvantages such as high costs and long construction durations. Computational fluid dynamics is an alternative engineering tool for the same purpose as computer-based simulation techniques. CFD codes are continuously being developed to be used for accurate predictions of complex fluid flow patterns in the place of physical models. The technique facilitates the simulation of a fluid flow process in which the standard flow equations are discretized and solved in each calculation cell. CFD technique has reasonable results and is relatively economic in most cases; however, the reliability of simulation for each case type should be assessed before its use in construction. This depends on both the competence and correct use of the codes. After the development of the design has been matured with numerical models, the design process is concluded by performing very little physical experimentation in the final stage. Jacobsen and Olsen (2010) reported that the codes have been used as a standard tool for many fluid mechanics disciplines for more than two decades such as mechanical (Kaya *et al.*, 2018) and aerospace engineering. However, the technique has not yet been fully recognized and is used as an auxiliary tool to reduce the time and cost of physical models. To reduce the need for physical modelling, codes must be improved and validated in many cases. There are many commercially available CFD packages. The packages have complex user interfaces to facilitate the model setup.

There are usually three main stages in CFD codes. These are pre-processor, computation and post-processor respectively. The pre-processing phase generates input parameters of the fluid flow problem into a CFD program by a user interface. In the pre-processing phase, the CFD program processes the user-defined input parameters of the fluid flow problem to the main process; the phase is also used for the last preview.

Numerical modelling and of course the pre-process begins with the generation of computational mesh or grid, which are formed in the computational domain as interconnected calculation discretization elements, or cells. Dividing the physical space by the cells into small volumes with numerous nodes, which store the evaluated values such as temperature, velocity and pressure. Numerically generated grid space effectively replaces the original physical one. At discrete points in a grid, each fluid parameter is represented by a value array. Whilst the actual physical parameters are constantly changing in space, a finer spaced grid better represents the reality than the coarser ones. As the grid spacing decreases, any valid numerical approach converges to the original equations. Refining the mesh increases the size of the numeric model for the same physical space by more elements and nodes. Besides these, timing limitations also force simulation engineers to choose a reasonable grid size including computer hardware and deadline. Achieving a compromise between fulfilling these constraints and achieving the right solutions by the user is not a less balancing technical action than the CFD model development itself (Flow Science, 2012). Therefore, grid production and localization are some of the main steps. Fluid properties, boundary conditions and initial state conditions need to be specified in the pre-processing stage. At the computation stage, each flow parameter is calculated in each calculation cell and is finally recorded as a sizeable data file. For this purpose, many post-processing tools were developed to visualize the results as 2D and 3D surfaces, vectors, contours, flow lines, isosurfaces, geometries and combinations of these graphs. The steps of a CFD analysis can be listed as following *Figure **3.4*** (Flow Science, 2012).

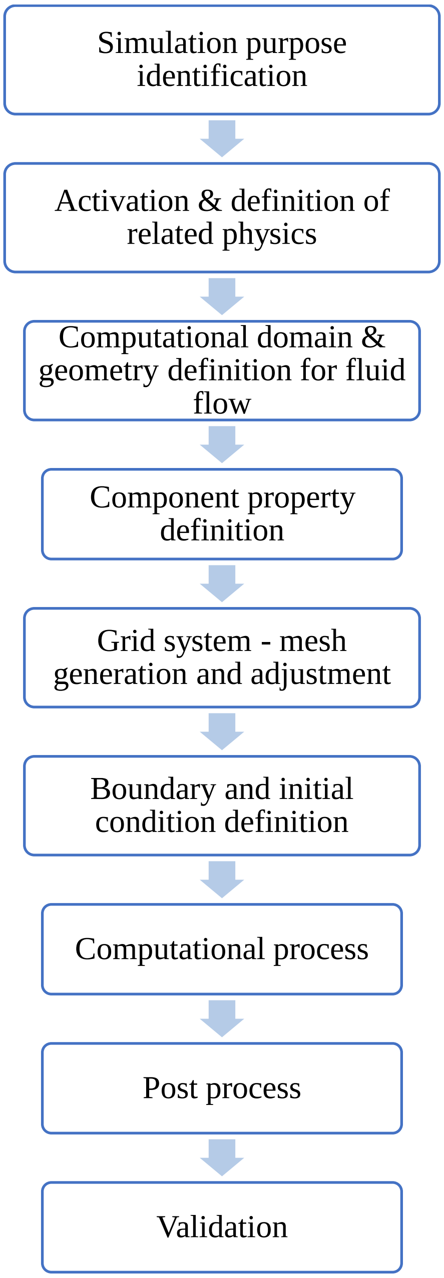

Figure 3.4 Steps of a CFD Analysis (after Usta, 2014)

3.2.1 General flow model of Flow-3D

Flow-3D is a general-purpose commercially available computational fluid dynamics (CFD) package used in the thesis. The package solves the fluid motion equations to obtain three-dimensional transient solutions for multi-physical flow problems with non-linear second-order differential equations. The outline of the numerical solution algorithms in Flow-3D is available in the user manual.

The package can be operated in various modes that correspond to different limiting states of general fluid equations. These elements describe the turbulence effects, heat transfer, surface tension, fluid solidification, Lagrangian particles, sediment scour, moving solids, granular flows, air entrainment, solid deformation, cavitation and porous media. It can be run in different modes such as compressible flow, incompressible flow, or limited compressibility conditions. Besides, Flow 3D has one or two fluid modes. These operational modes are corresponding to different options for motion equations. The one-fluid incompressible model is utilized in the thesis.

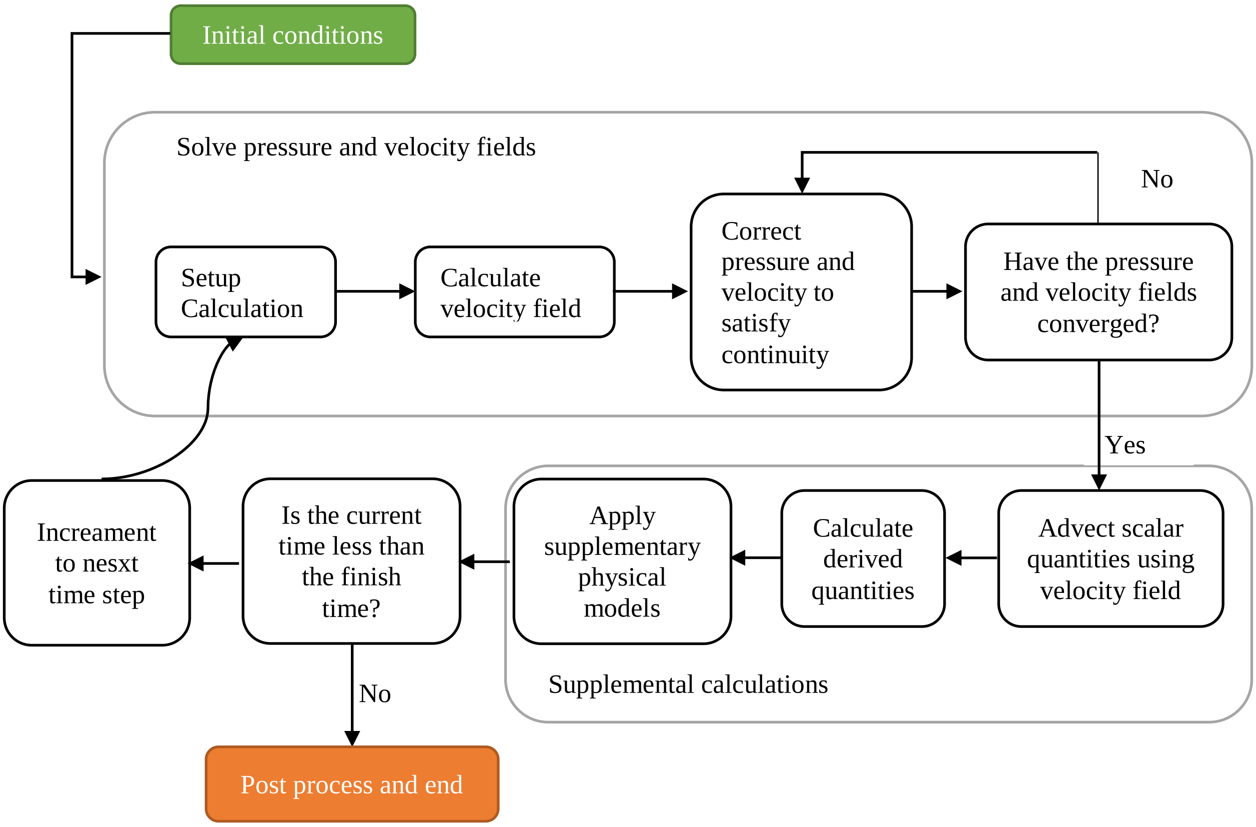

Figure 3.5 General Solution Technique for an Incompressible Flow (Flow 3D General Training Class 2013)

Taking improvement of the specialized air entrainment model and the free interface capture inside, FLOW-3D® was selected for the numerical simulation. Reynaud's Averaged Navier-Stokes, RANS, equations are valid in a domain, which contains the free surface, the solid boundary in the dropshaft and the flow through the inlet and the outlet channel.

Fluid properties such as viscosity, density and temperature should be defined for the numerical model. Fluid and relevant properties are specified using the fluid database tab. The fluid is selected as Water at 20 ° C.

3.2.1.1 Turbulence model

Flow 3D features five models of turbulence, which are the one-equation, the two-equation and the large eddy simulation (LES) models. In this thesis, the two-equation Renormalization group (RNG) turbulence model is selected which solves the same equations with the k - ε model. The difference is that the turbulence equation constants found empirically in the standard k - ε model is explicitly derived in the RNG model. Particularly, the RNG model describes low-intensity turbulence flows and strong shear regions belonging to flows more accurately and it is the recommended turbulence model for the activation of air entrainment is required (Flow Science, 2012).

For numerical discretization, a finite difference technique is implanted in the code. Generalized minimum residual (GMRES) technique selection is decided to solve the algebraic equations. It is assumed that the fluid is incompressible; the basic equations are presented as follows:

Equation for Continuity

$$\frac{\partial u_i}{\partial x_i} = 0 \qquad 3.1$$

Equation for Momentum

$$f_i - \frac{1}{\rho}\frac{\partial p}{\partial x_i} + \frac{\partial}{\partial x_j}\left(\nu \frac{\partial u_i}{\partial x_j}\right) = \frac{\partial u_i}{\partial t} + u_j \frac{\partial u_i}{\partial x_j} \qquad 3.2$$

k Equation

$$\frac{\partial(\rho k)}{\partial t} + \frac{\partial(\rho u_i k)}{\partial x_i} = \frac{\partial}{\partial x_i}\left(\alpha_k \mu_{eff} \frac{\partial k}{\partial x_i}\right) + G_k + \rho\varepsilon \qquad 3.3$$

ε Equation

$$\frac{\partial(\rho \varepsilon)}{\partial t} + \frac{\partial(\rho u_i \varepsilon)}{\partial x_i} = \frac{\partial}{\partial x_i}\left(\alpha_\varepsilon \mu_{eff} \frac{\partial \varepsilon}{\partial x_i}\right) + \frac{C_{1\varepsilon}^*}{k} G_k - C_{2\varepsilon}\rho \frac{\varepsilon^2}{k} \qquad 3.4$$

t is the time, f_i is gravity component, μ, ν and ρ are the coefficients of dynamic viscosity, the kinematic viscosity and density respectively. F is the VoF function, p is the gauge pressure, G_k is the generation of turbulent energy caused by the average velocity gradient, μ_{eff} is the dynamic viscosity revisionary coefficient, $\mu_{eff} = \mu + \mu_t$, $G_k = \mu_t \left(\frac{\partial u_i}{\partial x_j} + \frac{\partial u_j}{\partial x_i}\right) \frac{\partial u_i}{\partial x_j}$, $\mu_t = \rho C_\mu \frac{k^2}{\varepsilon}$, $C_{1\varepsilon}^* = C_{1\varepsilon} - \frac{1-\frac{\eta}{\eta_0}}{1+\beta\eta^3}$, $\eta = \left(2E_{ij} \text{ x } E_{ij}\right)^{\frac{1}{2}} \frac{k}{\varepsilon}$, $E_{ij} = \frac{1}{2}\left(\frac{\partial u_i}{\partial x_j} + \frac{\partial u_j}{\partial x_i}\right)$ (Zhang et al., 2018). Launder & Spalding (1972) provided some constants substantiated by many experiments: C_μ = 0.0845, σ_k = σ_ε = 0.7194, $C_{1\varepsilon}$ = 1.42, $C_{2\varepsilon}$ = 1.68, η_0 = 4.377 and β = 0.012.

3.2.1.2 Air Entrainment Model

In free-surface flows, turbulence in the fluid may be sufficient to disturb the surface where air entrains the flow. An example to illustrate the importance of the process, in rivers and streams to maintain a healthy fish population where water is needed for the maintenance of microorganisms for water purification and the maintenance of a healthy fish population. Air entrainment is technically produced at the spillways downstream of hydropower plants to decrease the cavitation damage possibility at the base of the spillway. The cases where air entrainment is not desired are the filling of liquid containers for consumer products and in the sprue and runner systems used by metal casters (Hirt, 2012).

The air entrainment model is also utilized to approximate fluid flow aeration. The model runs without requiring the two-phase solution. In the scope of this study, three modules of the code for air entrainment are examined to compare the compatibility of the code with real bubble behaviour in the complex dropshaft flows: (a) regular air entrainment model, (b) bulking option activation (density variation with entrained air) and (c) drift flux activation (buoyancy of air bubble).

a- The air entrainment module can be activated from Physics> Air entrainment. The entrainment rate coefficient should be defined as a positive value and the default is 0.5, which is most suitable for each case. Surface tension coefficient entry is optional & can be defined at this mode to include the surface tension effects in the force balance regarding the amount of entrained air without activating the surface tension pattern. In this mode, air entrainment is calculated as a passive tool due to the lack of any effect on the flow. This can be accepted while the amount of entrained air is relatively small.

David & Hirt (2004) offered the air entrainment model in FLOW-3D®. This model assumes that the air entrainment mechanism is caused by the instability force P_t (turbulent kinetic energy per unit volume), which is generated by the turbulence of the free surface. When the level of turbulence exceeds the stability force P_d which is associated with gravity and surface tension, the volume of entrained air into the water δV can be calculated by the basic equations below:

$$L_T = CNU^{0.75} k^{1.5} / \varepsilon \tag{3.5}$$

$$P_t = \rho k; P_d = \rho g_n L_T + \sigma / L_T \tag{3.6}$$

$$\delta V = \begin{cases} C_{air} A_S \sqrt{2(P_t - P_d)/\rho} & \text{if } P_t > P_d \\ 0 & \text{if } \quad P_t < P_d \end{cases} \tag{3.7}$$

where L_T represents the turbulence length scale, k and ε are the turbulent kinetic energy and the turbulent dissipation rate, respectively and CNU is a constant equal to 0.09. g_n is the gravity component normal to the free surface, σ is coefficient of surface tension between liquid and gas, C_{air} is a proportionality coefficient, δV is the volume of entrained air per unit time and A_s stands for the area of the free surface in each cell (Zhang et al., 2018)

b- Otherwise, the flow can be influenced by lighter air entrained into the fluid. The density-conveyed variable-density model should be enabled in the Physics> Density evaluation to consider the changes in fluid density due to the entrained amount of air volume and mass. This variation in the fluid density due to air entrainment is termed macroscopic density and formulated as

$$\rho_{mac} = (1 - C)\rho_w + C\rho_a \tag{3.8}$$

where C is calculated entrained air, ρ is the density of water and ρ_a is the air density. (Valero, 2016).

c- From the observations, the components can receive different flow velocities in the fluids composed of multiple components as mixtures where the components have different densities as particles/fluid, bubbles/fluid, fluid/fluid. In general, the differences in velocities due to the non-uniform body forces are very noticeable, for instance, large raindrops in the air or gravel sinking in the water. However, under many conditions, the relative velocities accepted as small enough to be defined as a “drift” of one component from the other. Examples are silt in the water and dust in the air. The "drift" identification must be related to whether the inertia of the dispersed component moving within a continuous component is meaningful. If the relative motion inertia can be ignored, and the relative velocity reduced to a balance between a driving force and an opposing drag force between the components, then the “drift-flux” approximation arises. Drift velocities are mainly responsible for mass and energy transport. Some momentums are also transportable, but this is usually quite small and neglected in the FLOW-3D drift model. The idea behind the drift pattern is that the relative movement between the components can be estimated as a continuum rather than as separate elements (or particles). This increases the efficiency of the calculation as it does not require the monitoring of the movement and nor require computation for the interaction of the discrete elements (Brethour and Hirt, 2009).

Hirt (2012) reported a similar dropshaft air entrainment event and utilized the variable density model since it was thought that the buoyancy caused by air entrainment could affect the flow features in the shaft reservoir. Hirt reported that the repetitive stimulation with the passive option revealed little differences, probably due to the large jet-speed so that the lifting forces not able to contest with the inertia, at least in the modelled region. The comparison with Hirt's passive entrainment option is argued in the discussion section for the case of this thesis.

The entrainment rate coefficient is set as a default value of 0.5. The surface tension coefficient is also set to the default value of 0.073. The air has a density ρ_a of approximately 1.225 kg/m3 at 15℃, so the density of phase #2 is selected as it.

3.2.2 Volume-of-fluid advection techniques

Computational fluid dynamics (CFD) codes are used for both open channel & closed conduit flows. FLOW-3D®, one of the most popular codes especially for open channel flows, contains alternative techniques under the VoF (Volume of Fluid) advection methodology. The Volume-of-Fluid advection options are used for the control of the fluid fraction, especially the free surface, changes through the mesh. A comparison of three VoF advection techniques is made to assess the proper technique for the location of the free surface; the results are discussed in section 4.2. The details of the compared techniques are introduced below.

The volume-of-fluid advection panel offers several options for sharp interface tracking. The options under the VoF advection for incompressible free surface flow are Unsplit Lagrangian technique, Split Lagrangian technique, one fluid no free surface (confined flow only), Standard one fluid free surface flow technique(TruVoF) & Automatic selection option which is governed by the code for proper conditions. The third and fourth options, Unsplit and Split Lagrangian techniques are compatible with both cases. Although each technique has a different field of use and has strengths and weaknesses related to the case, the default setting (Automatic option), which is selected correctly by the program algorithm for both beginners and advanced users, works well for most cases. In some scenarios, especially the free surface flows along the diagonal (e.g., flow along the vector connecting (x=0, y=0) and (x=1, y=1)), the Lagrangian VoF advection techniques could be used when the mass conservation errors emerged due to the advection technique (Flow Science, 2012). Generally, the Unsplit-Split Lagrangian techniques show decent accuracy in tracking sharp interfaces for complex 3D movements. The Split Lagrangian technique characteristically has a lesser cumulative volume error than the Unsplit technique, whilst the volume error could increase if the technique is used together with a general moving object module (Flow Science, 2012).

For the TruVoF - one fluid free surface mode in the code, F represents the fraction of volume occupied by the fluid, e.g. F=1 means full of fluid in the cell. F=0 reflects the absence of fluid or void region existence. Besides, only partially filled cells have a value between zero and 1, depending on the percentage of volume. Second, an advection algorithm is required to define the surface as a sharp interface between air and fluid. Third, the application of free surface boundary conditions is necessary for the interface. The FAVOR concept provides the volume and area ratios in each staggered cell and the rates are integrated with the conservation equations (*Figure* **3.6**). The main advantage of the FAVOR technique is the domain geometry independence of the grid system. Grid production is not affected by any change in geometry (Flow Science, 2012).

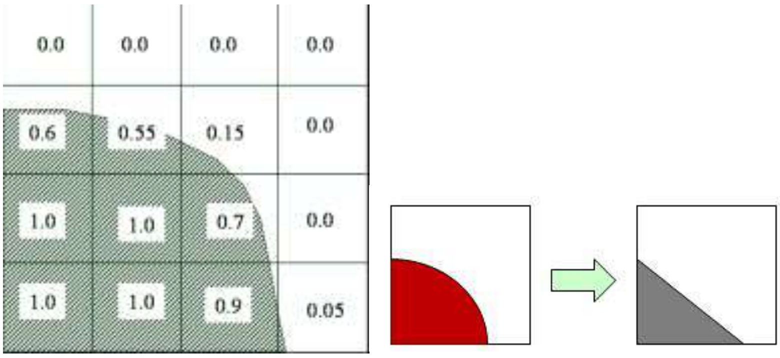

Figure 3.6 Typical values of the VoF function near the free surface (Barkhudarov, 2003) and FAVOR (Introduction to Flow 3D for Hydraulics-2013)

When air water and air are identified and explicitly treated as two different phases, the F function represents incompressible phase volume fraction (water), while the compressible phase (air) is represented with volume fraction 1-F this may have a constant density or a density computed from the fluid state equation. It is significant to know that the F function is defined as a discontinuous function to monitor a two-fluid interface or a sharp free surface accurately. An apriority of a numerical application for the VoF technique is to advance the interface of fluid over time without character demolition as discontinuity. Furthermore, in single-fluid modelling, it is necessary to introduce appropriate boundary conditions on the free surface (Vanneste, 2012).

The FAVOR tool can be used in conjunction with any type of grid, such as grids with rectangular or distorted elements and for the situations, structured or unstructured grids exist. Structural grids are advantageous in that they are easy to produce and the indexes of neighbouring elements are known. The rectangular grid elements facilitate the fractional area and volume of elements computation. In addition to the FAVOR technique, there is a free grid approach consisting of simple rectangular meshing elements and multi-block mesh options. In the free grid approach, the geometry structure does not depend on grid generation, the processes are completed separately. A

VoF methodology should include an algorithm to track the sharp interface between the void and the fluid. Sharp fluid interface representation in Flow 3D is shown in *Figure* **3.6**. TruVoF is the VoF recommendation technique of Flow 3D (Flow Science, 2012).

In FLOW-3D®, free surface tracking is performed using the “True” version VoF technique, as a standard option for beginner users and/or basic problems, which needs three key elements to be applied (Bombardelli et al., 2001). As first proposed by Hirt and Nichols (1981) the one fluid free surface (standard) VoF advection technique in FLOW-3D® is based on the approach of donor-acceptor. The fluid forms are formulated in a VoF function $F(x, y, z, t)$, defines VoF for per unit volume and performs the following equation:

$$\partial F / _{\partial t} + \partial / _{\partial x_i} (F u_i) = 0 \qquad 3.9$$

Where x_i and u_i are coordinate component and the time-averaged velocity, respectively. In contrast with other techniques, the flow is calculated only for the liquid containing cells and the gaseous cells are not considered. Therefore, the VoF technique combines satisfactory accuracy, reasonable computational cost and the benefits of minimum memory storage (only the variable, *F*, must be saved) (Sousa et al., 2009).

In FLOW-3D®, the Unsplit Lagrangian Advection technique based upon a three-dimensional reconstruction of the fluid interface was developed and implemented. When the Fluid Volume (VoF) function is not aligned with the flow coordinate direction, without restoring to an operator splitting technique that affords improved accuracy, the Unsplit Lagrangian Advection technique is carried in one step. For a complex two-fluid flow with/out a sharp interface, various enhancements were made to the original standard technique algorithm to improve stability and accuracy. The standard technique uses the operator splitting function and old time-level values of the VoF function to calculate the fluxes in three main coordinate directions. This approach creates the possibility of overfilling or over emptying the computational cells where the volume fluxes are important in all three main directions and the time step size is close to the local CFL number and Courant stability limit. The Unsplit advection technique was developed to mitigate these shortcomings of the standard algorithm. The fluid interface is reproduced employing a piecewise 3D linear representation, where the interface is considered planar in each cell (or control volume) containing the interface. Then, the volume of fluid confined by the interface and faces of the cell is moved in the Lagrange technique along with the local velocity vector. Lastly, the advanced volume is restored to the Eulerian grid domain to find new values of the function of the fluid fraction F (Barkhudarov, 2003).

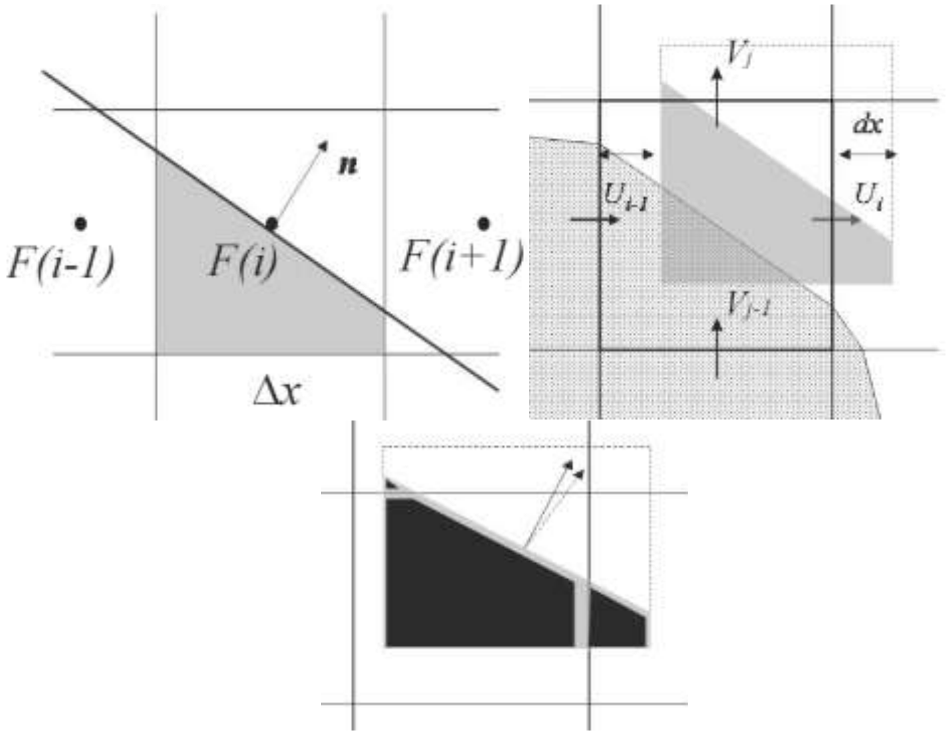

Figure 3.7 a) piecewise linear interface reconstruction with the normal n; b) moving the control volume and c) overlaying the advected volume onto the grid (Barkhudarov, 2003).

No difference exists in how the fluid interface is reconstructed in the Unsplit and Split Lagrangian techniques; the modification between them is just how the fluid moves after reconstruction. Whereas in the ‘Unsplit’ procedure, fluid is relocated along the 3D velocity vector, in the ‘Split’ procedure, by step by step interface reconstruction, fluid is relocated in the directions of x, y, z respectively (Barkhudarov, 2003). Split VoF techniques can be expressed as the advancement of 1D advection steps, carried out by the mapping of a plane onto itself to each direction of a coordinate system. Once the advection has been made, these mappings systematically satisfy the consistency condition $0 \leq Cc \leq 1$. In multidimensional flows, it is required to change the sweep direction to reduce possible asymmetries. In the linear mapping technique, the interface reconstructed at time t^n is mapped at the interface at time t^{n+1} with a linearized velocity field. The variables are nondimensionalized with the mesh spacing and the time step$\Delta t = t^{n+1} - t^{n}$, therefore the velocity component becomes the Courant (CFL) number (Bna et al., 2013).

To capture free surface, impingement point and aeration correctly, all three options of fluid advection models are investigated and compared with each other.

3.2.3 Grid generation

The approach of the code is dividing the flow domain into rectangular grid cells, which is sometimes called brick elements. Due to their structured nature and regularity, rectangular grids are easy to handle and store. Flexibility is facilitated by non-uniform grid spacing for complex geometries. The cells are numbered consecutively using three indices: i, j, k in directions x, y and z, respectively. Similar to the regular coordinates of a point in physical space, each cell is identified by a particular address (i, j, k). Structured rectangular grids benefit from the relative ease of developing numerical techniques, (concerning their relationship) their transparency to the original physical problem, and the precision and stability of numerical solutions. The earliest numerical algorithms based on finite differences and finite volume techniques were initially developed on such basic meshes. The finite-difference technique is mainly based on the direct application of the definition of derivatives by fragmentation and the expansion of Taylor. The technique, which was considered to have been developed by Euler in 1768, is the oldest technique applied to differential equations to obtain numerical solutions. The finite volume technique is directly derived from an integral form of conservation laws for fluid movement and therefore has inherited conservative properties (Flow Science, 2012).

The code uses an orthogonal mesh grid system in the cylindrical or Cartesian coordinates and the latter is selected for the investigation. The geometry in the domain is identified simply and appropriately without the need for a body-mounted grid system so that the grid production and geometry are independent of each other. However, particularly close to the walls, grid space definition is an important model development aspect. A significant grid refinement process should be carried out for the solution of boundary layers.

3.2.4 Initial & boundary conditions

The geometry is generated with a basic geometry tool inside FLOW-3D® since the geometry consists of three basic cylinders. To reduce the computational time, the water filling shaft basin is defined as an initial state (t=0 initial state module is utilized) to pass the transitional unnecessary data. To decrease allocated memory, the out-of-motion zone surrounds the dropshaft system is filled by block volume.

One of the significant stages of numerical analysis of fluid flow is determining the appropriate boundary conditions, which must be matched to the real physical conditions. To compare the results of CFD with the experimental results, appropriate boundary conditions and mesh distributions are needed to be arranged. The code uses orthogonal hexahedral meshes to define the three-dimensional flow field in the coordinate system, so there are six boundaries defined in the rectangular mesh prism as in *Figure **3.8***.

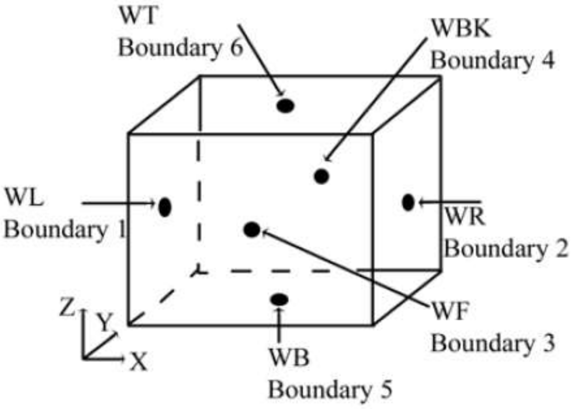

Figure 3.8 Boundary Nomenclature, WL: i=1, WR: i=imax, WF: j=i, WBK: j=jmax, WB: k=1, WT: k=kmax (Flow Science, 2012).

The volume of Flow Rate-VFR Boundary Condition (Q): It is generally appropriate to define a flow rate to a region instead of velocity. The flow is distributed over the wetted area when the fluid height is set as a limit. The VFR boundary condition is compatible with all physical models.

Pressure Boundary Condition (P): There are two options for pressure boundary conditions: the default option is stagnation pressure condition and the other option is a static pressure condition. For the former, $P+\rho U^2/2$, is equal to the specified stagnation pressure value, where U is the incoming flow normal velocity component. In this case, the static pressure can be calculated by subtraction of dynamic pressure from the specified value and therefore the pressure does not remain constant in general. For the stagnation pressure boundary condition, it is assumed that the fluid nearby the boundary is stagnant at the specified approximate pressure value to a large fluid reservoir outside the mesh area. At the specified pressure value, the stagnation pressure boundary condition assumes the fluid next to the boundary is stagnant. This approach relates to a large fluid reservoir outside the mesh domain and the fluid must be accelerated at zero velocity to enter the fluid zone. The static condition assumes the fluid does not perform any acceleration or deceleration when entering or exiting the domain, such as a flow in a fixed diameter pipe. The most realistic physical state to use is the stagnation condition. A static state says nothing about the flow state outside the boundary. This may cause incorrect results, so care should be taken when using this pressure boundary.

A special condition is not required as there is a zero velocity derivative along the boundary at the symmetry boundaries (S) and therefore the production of zero turbulence. Besides, a zero flow area ensures automatically there are no advective or diffusive fluxes. The wall boundary (W) condition is used as a passive non-slip boundary condition.

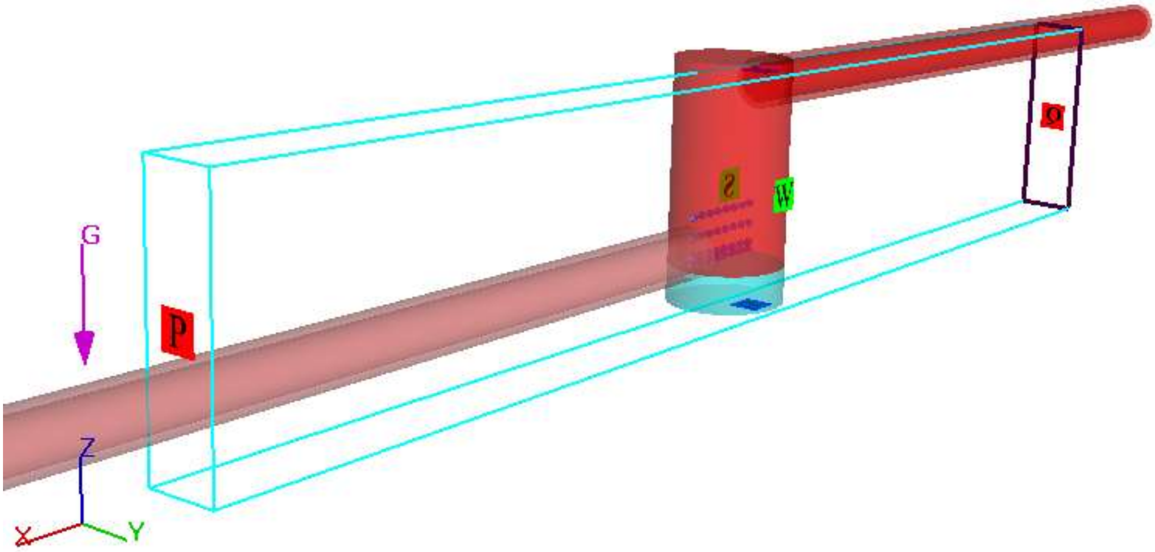

Figure 3.9 Initial & Boundary Conditions for elevation constrained BC, P is changed to Outflow for non-constrained BC

The upstream (X-Min or WL) boundary is set as a volume flow rate by defining water elevation at the upstream boundary. The downstream (X-Max or WR) boundary is set as a pressurized outflow, which means the boundary has little effect on the upstream conditions and the flow at the field has a stable elevation, the fixed water level is assumed. To decrease the computational time, half of the symmetrical system is simulated and (Y-Min or WF) is set as the symmetry boundary. (Y-Max or WBK) and (Z-Min or WB) are set as solid, non-slip wall boundaries that are already (& mostly) covered with block volume.

The boundary conditions used by this study are below.

- WL: Volume flow rate condition
- WR: Stagnation pressure condition (Hydrostatic pressure)
- WT: Stagnation pressure condition with F=0 (Inactive Boundary)
- WB: Wall condition (Inactive Boundary)
- WF: Symmetry condition (Inactive Boundary)
- WBK: Wall condition (Inactive Boundary)

3.2.5 Numerical solver options

Regarding previous explanations about the grid system and the VoF technique, all dependent variables have local average values in each computational cell. As in *Figure* ***3.10***, except for the velocities in the cell faces (due to the staggered grid), all variables are located in the centres of the cells. By identifying fractional face areas and fractional volumes of flow open cells; wall boundaries, curved barriers, or other geometrical properties are embedded in the mesh. Discrete numerical approximations of the governing equations are built to solve the algebraic equations computationally. Surface stresses, surface fluxes and body forces are calculated based on surrounding variable values for each control volume. These are then combined to generate conservation law approximations by the expression of equations of motion. Despite the existence of various implicit options, most of the terms in the equations are explicitly evaluated (i.e., by using the current time level values of the local variables). This provides a simple and efficient computation scheme but needs a limited time-step size to obtain accurate and computationally stable results (Flow Science, 2012).

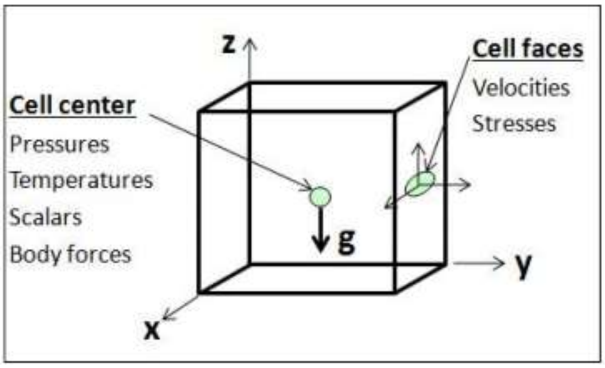

Figure 3.10 Grid System for Flow 3D (Flow 3D Advanced Hydraulic Training-2012)

A significant exception to this explicit formulation is in the treatment of pressure forces. The pressures and velocities are implicitly combined in forwarding time step pressures in the momentum equations and the forward time step velocities in the continuity equation. This semi-implicit like formulation of finite difference equations provides an effective solution for low-speed and incompressible flow problems. However, the semi-implicit formulation ends up with coupled equation sets that must be solved by an iterative technique, which is provided in the code with three options. The successive over-relaxation (SOR) technique is the simpler one, and in some cases, a special alternating-direction line implicit technique (SADI) can be used where a more implicit solution is needed. Depending on the problem characteristics, the SADI technique can be used in one, two, or all three directions. With the generalized minimum residual GMRES technique, the equation system is solved simultaneously by an iterative technique across the domain. This is in contrast to the SOR algorithm that adjusts the cell-based pressure to force the continuity equation and the approach used in the ADI algorithm, which adjusts pressures across each mesh column directed along with the selected directions. Even though the simplicity and memory efficiency of the SOR algorithm, not necessary store the extra information of each cell, a large number of iterations may be required to converge, especially for problems that need to be made to have almost uniform pressure settings over a large domain region. However, as long as the relaxation parameter is equal to or less than one, it will always converge. The number of required iterations for convergence with GMRES is typically 10 times less than for SOR; however, convergence is not always provided. For many problems, therefore, the GMRES algorithm is much more efficient in computational terms, since it can converge with much less iteration than other solver algorithms. This applies in particular to problems in which the pressures on a large area of the domain are closely linked. SOR can still be more efficient in the computation of the shallow free surface problems where the pressure is kept more or less controlled by the position of the free surface; the pressures between the two points in a liquid are not strongly combined (Brethour, 2009).

The basic numerical methodology used in the code has a first-order formal accuracy concerning space and time increments. Although the finite difference mesh is not uniform, special preventions have been taken to maintain this accuracy degree and even second-order accuracy is available. In all cases, boundary conditions are first-order accurate at least. For instance, the technique is equivalent to the first-order interpolation of boundary conditions within the cell for the ones occupied by an obstacle partially (Flow Science, 2012).

Many parameters affect the simulation results and duration, such as solution technique (explicit or implicit), time step size & limits, convergence criteria and numerical approaches. There is a balance between simulation accuracy and run time. To ensure this balance, it is important to select the appropriate numerical options to provide an efficient and optimum solution to a simulation. In this thesis, water was used as a single fluid in all simulations (the two-phase solution was not selected, instead, the air entrainment module was activated). Water is defined as an incompressible Newtonian fluid. The pressure solver is selected as implicit GMRES due to the reasons mentioned above and the stability considerations.

Isolated fluid droplet removal (or misty fluid region clean up) option under the VoF advection options is also activated to ignore minor detached droplets to facilitate stability for faster transient solutions. Some applications need to maintain smooth free surface shapes to achieve accuracy. Especially for the cases when “misty” regions, due to excessive free-surface breakup while splashing, can reduce the quality of numerical solution and time step size. Trying to monitor the movement of small droplets of fluid in all these regions can be inefficient and probably unnecessary. A typical FCLEAN input value shall be between 0.0 and 0.1. The use of this algorithm is only suggested in the cases with excessive free surface deformations where the flow is controlled by the conditions on the free surface substantially. In general, its application causes only minor errors (less than 1%) in the total volume of fluid but provides accurate and efficient solutions (Flow Science, 2012). For this investigation, FCLEAN is selected as 0.02 for TruVoF and 0.005 is selected for two Lagrangian advection techniques.

To prevent void opening inside the continuous fluid regions, the f-packing algorithm is served. The algorithm is used only in single fluid flows, producing small negative divergences in the internal fluid cells where the fluid fraction F value is less than 0.99. The F-packing rate is proportional to the cfpk coefficient. The default value is 1, no packing is performed when it equals 0 (Vanneste, 2012). F-packing is adjusted relevant to the mentor tips and warnings rarely.

The main numerical parameters for numerical options are listed in *Table **3.1***. Parameters not included in this list have default settings.

Table 3.1 Important parameters used in FLOW-3D®

Option	Set up	Parameter
Fluid	Incompressible	ICMPRS=0
Viscosity	Newtonian fluid	IFVISC=1
Turbulence	RNG k – ε Standard convergence criterion	IFVIS=4 EPSADJ=1
Pressure solver	General Minimal Residual (GMRES)	IGMRES=1
Momentum advection	First-order, upwind explicit scheme	IORDER=1, ALPHA=1, IMPADV=0
VoF advection technique	Unsplit Lagrangian, Split Lagrangian & Standard Techniques	IFVoF=5, IFVoF=6, IFVoF=4
Time step control	Automatic	AUTOT=1

4 RESULTS AND DISCUSSION

Despite the missing information in the geometry data, the model setup was completed by making some assumptions and corrections, which of the most important is the length of the protrusion (overlap length of dropshaft and inflow pipe). After some tests and judgements, the length is determined as 5 cm concerning the visual observations on the impingement of the free surface point of R1 Regime Q=1m³/s as seen in *Figure* ***4.1***.

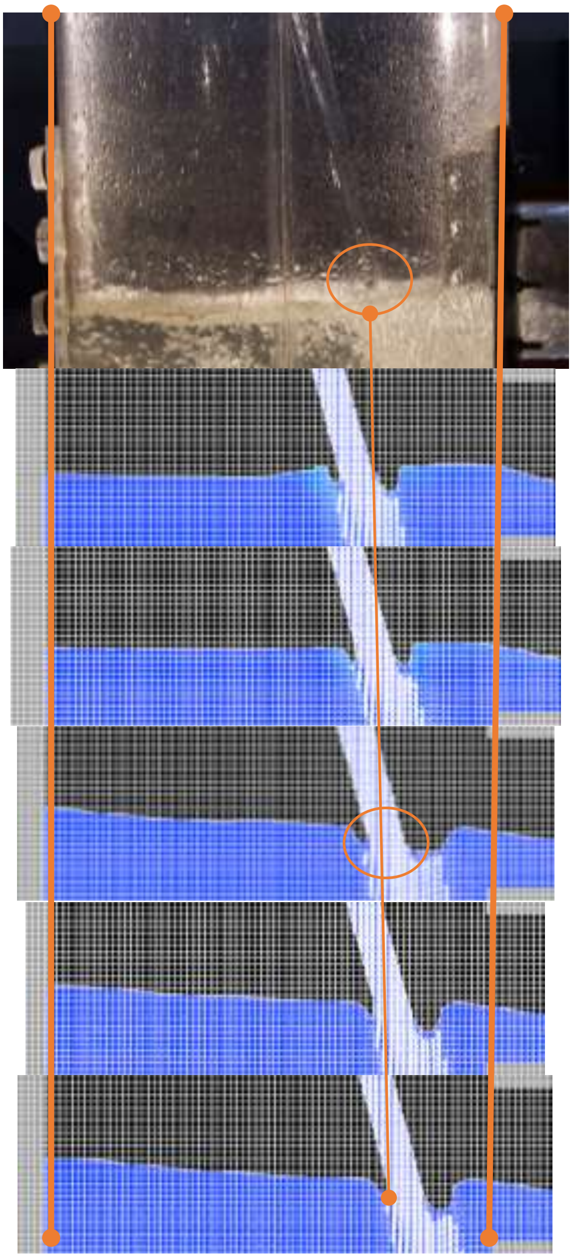

Figure 4.1 Protrusion length investigation under R1 regime Q=1 m³/s with constrained BC elevation, 3 cm, 4 cm, 5 cm, 6 cm & 7 cm from up to down respectively (grid M3 is employed).

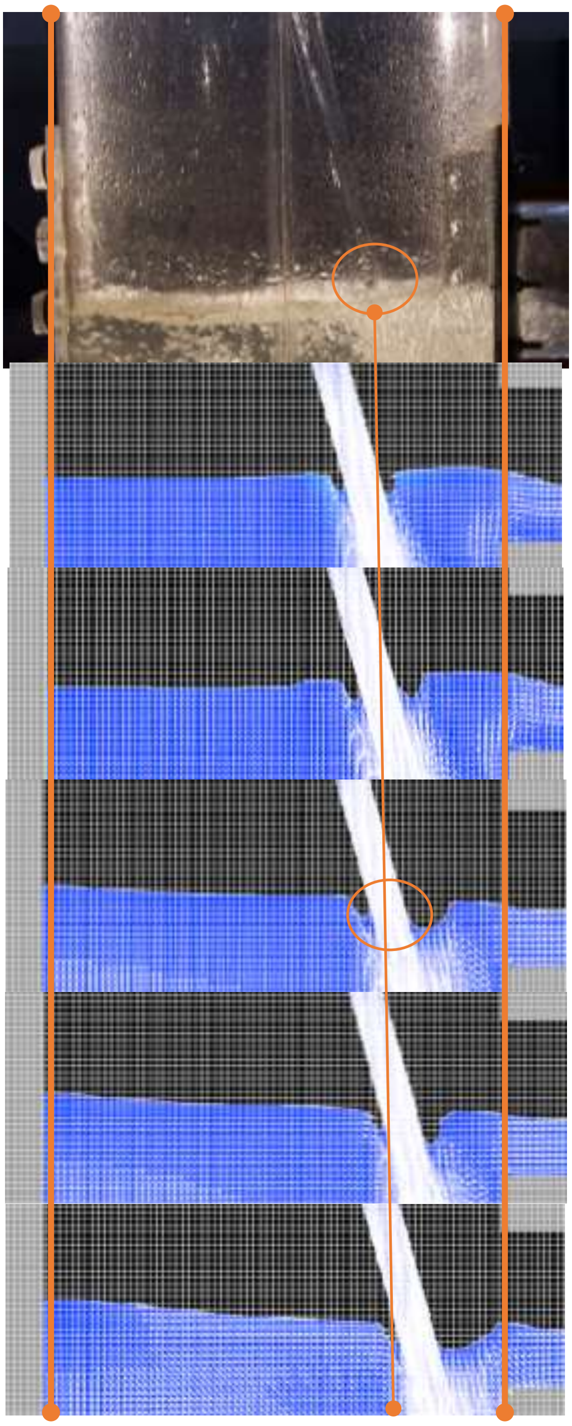

Figure 4.2 Protrusion length investigation under R1 regime Q=1 m³/s with non-constrained BC elevation, 3 cm, 4 cm, 5 cm, 6cm & 7 cm from up to down respectively (grid M3 is employed).

By using one of the most important advantages of the code, the FAVOR technique serves a grid system independent from the geometry of the domain. In other words, geometry variations, such as adding or replacing geometry, does not affect the grid system. Different protrusion lengths were simply solved by changing the length of the upstream pipe, with no touch on the grid.

The internal diameter of the dropshaft is also accepted as 35.5 cm instead of 35.8 cm due to the production considerations, which fits 14 inches. The internal diameter of inflow and outflow pipes are accepted as it is, the wall thickness of both is considered as 0 mm to match with the experimental study measurements, still, the thickness remains negligible compared to the manhole diameter, protrusion length and drop height.

4.1 Mesh Independency Analysis with Energy Dissipation Rates

The selection of the grid is one of the most significant time-consuming parts of this thesis. The mesh served by the code is a structured orthogonal grid, which fits the Cartesian coordinate system but not fitted to the body geometry (e.g. defined independently). Once the geometry is defined either with code-provided primitive geometries or by the imported STL file format. The format is used especially for complex geometries (spillway, tribune blade, etc.) requiring professional sketching programs such as AutoCAD and SolidWorks (Ucar & Kumcu, 2018; Kumcu & Ucar, 2018). Due to the simplicity of the geometry of this case, primitives are utilized for geometry creation. Mesh independency analysis should be carried out in a sense to balance the accuracy and consumed run time. Generally, finer meshes provide more reliable results, but the limitations of run time and computer memory restricts the number of grid points to be used in the simulation. Another restriction is round off error, which is highly dependent on the number of calculations, the error cumulatively increased by the amount of calculation inherited, i.e. the more the calculation, the more the round off error. After the independence analysis is done and the appropriate mesh size is obtained, numerical study and the evaluation of the results can be carried out safely.

Due to the symmetrical geometry of the drop structure, only half of the system is simulated in the flow domain, so half of the calculations are made, which facilitates a significant amount of computational time reduction. A visual option called enable symmetry axis can be employed at the “Symmetry Boundary Conditions” to visualize the complete real system at the post-process stage. The application of symmetrical visualization can be seen in *Figure **4.6*** & *Figure **4.8***.

From the beginning to the end of the mesh refinement process, the FAVORized geometry and mesh adaptation can be controlled with the FAVORize option in the model setup. The FAVORize option visualizes the mesh-mapped geometry as a pre-processing tool before solving the whole system and gives an idea for the proper discretization of the geometry. Due to the hardnesses seen on upstream pipe discretization and the negligibility of the alteration, pipe thickness is exaggerated.

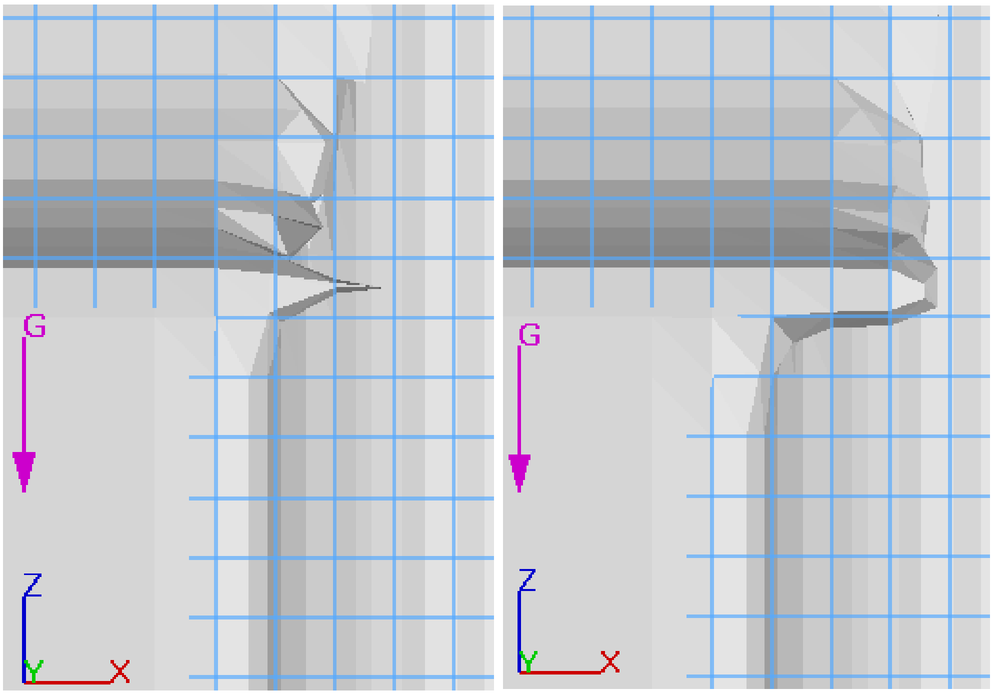

Figure 4.3 Profile view of FAVORized coarsest Grid M1, before & after the thickness exaggeration.

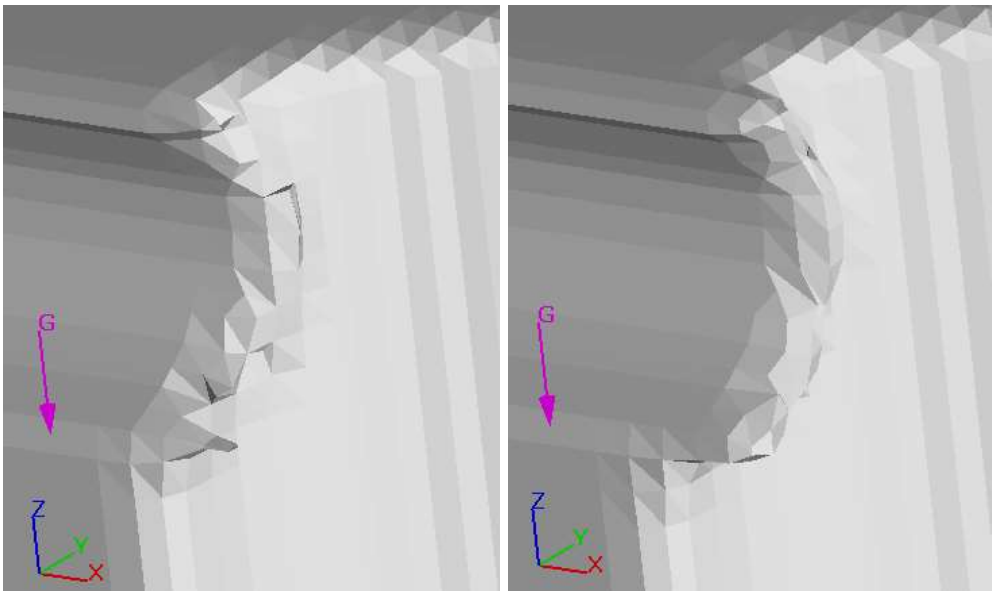

Figure 4.4 Angled view of FAVORized coarsest Grid M1, before & after thickness exaggeration.

After the “FAVORize” check, a relatively coarse mesh should be processed to pass the transitional unnecessary data with rapid convergence. Once the flow convergences using coarser mesh and the water profile is settled more or less, the mesh size needs to be gradually decreased and finer and finer meshes solved. Mesh refinement requires systematic management and the use of the “Restart” option. The “Restart” option is a tool that uses previous last result data to continue the computation and the option facilitates passing the transitional unnecessary data and lessens the computational time. The steps of the mesh refinement are introduced briefly in *Table 4.1*. The finer the mesh the longer the computational time. Thus, grid size selection is also limited by the deadline of the thesis.

Table 4.1 Mesh refinement & gird properties, description implies relative situations.

Grid	Description	Size	Total Cell Number
M1	Course Mesh	15mm	166,608
M2	Fine Mesh	7.5mm	1,381,536
M3	Finer Mesh	5mm	4,608,000
M4	Finest Mesh	4mm	9,000,000

FAVORized initial condition geometries of the structure are shown in *Figure 4.5* & *Figure 4.7*. To introduce the figures, the domain surrounding the manhole is filled with a solid component to lessen the allocated computational memory and so the time. To easily distinguish the difference between the grid sizes, look at the internal edges of the drop manhole and pipes.

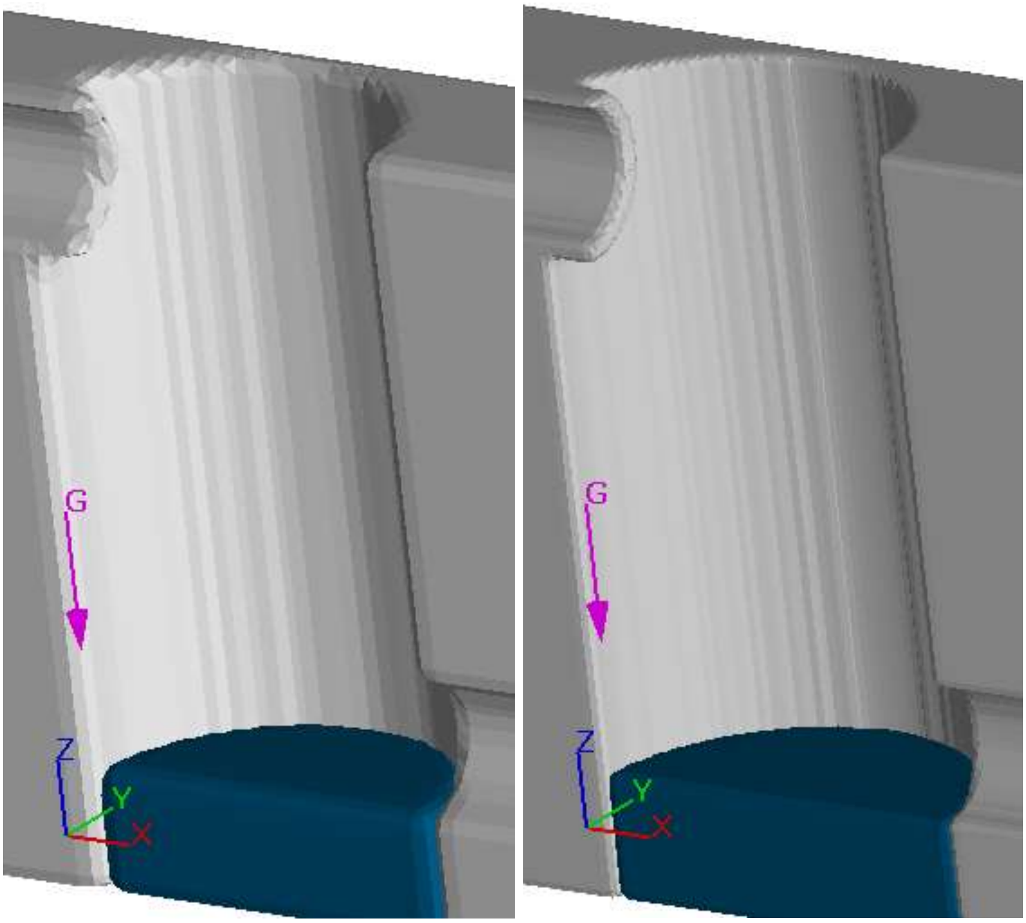

Figure 4.5 Grid M1 & Grid M2 respectively, check the smoothness of the internal edges.

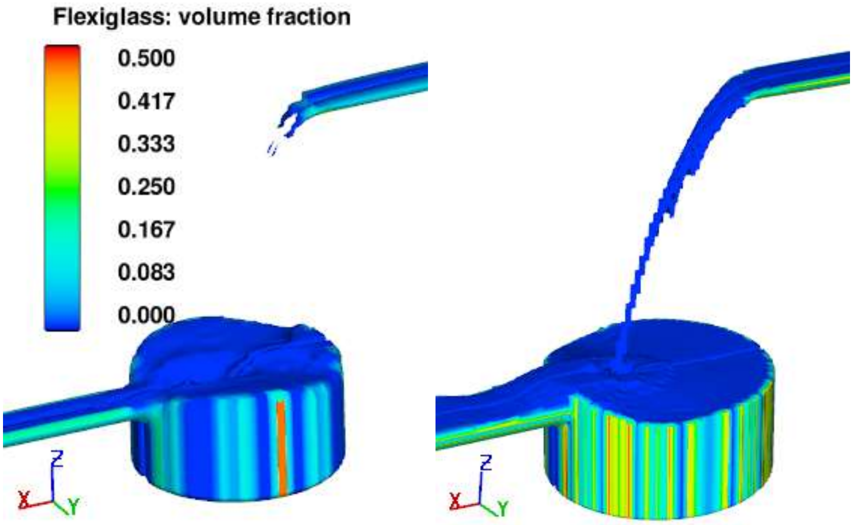

Figure 4.6 Solid component volume fractions in Regime R1 Q=1m^3/s for grid M1 & grid M2 respectively.

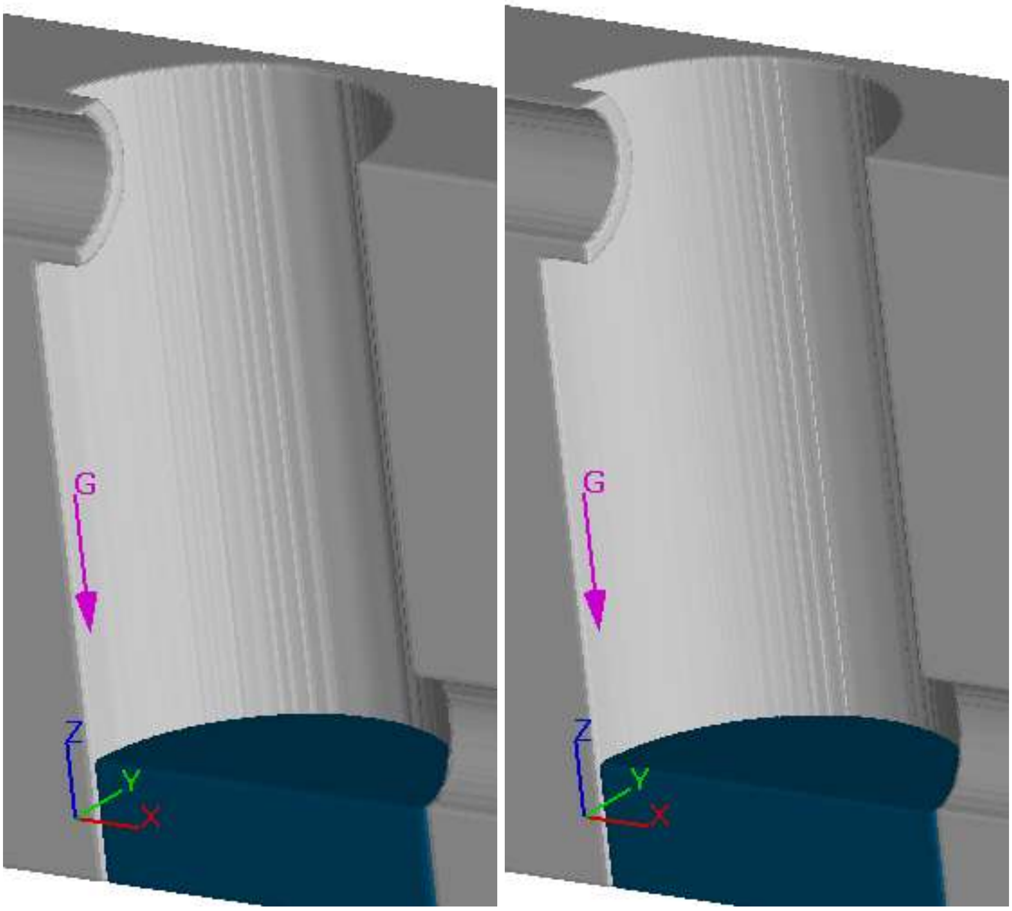

Figure 4.7 Grid M3 & Grid M4 respectively, check the smoothness of the internal edges.

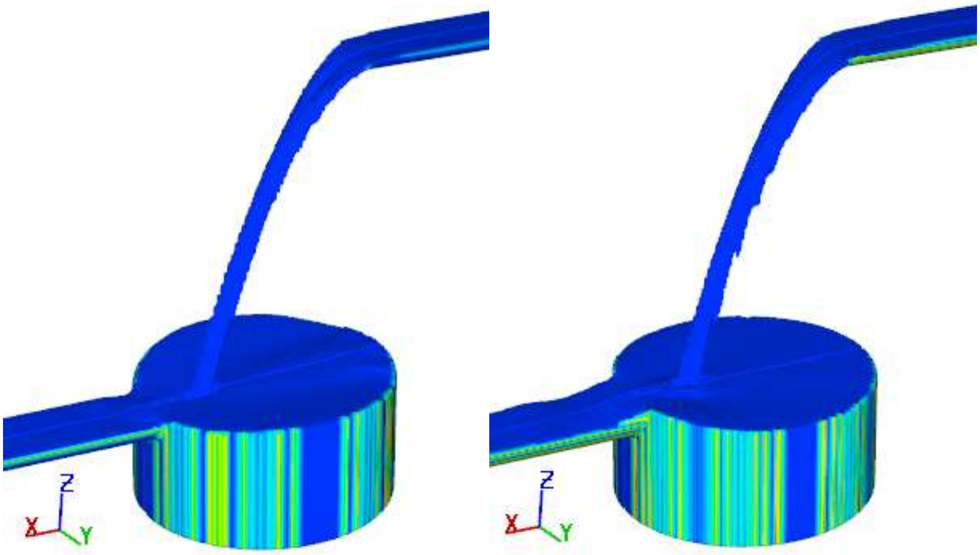

Figure 4.8 Solid component volume fractions in Regime R1 Q=1m³/s for grid M3 & grid M4 respectively, the same legend with Figure 4.5.

Figure 4.6 & *Figure 4.8* indicates the grid mesh compatibilities of the case better than *Figure 4.5* & *Figure 4.7* with the help of the filled water inside the drop manhole. This illustration is another FAVOR mode usage, which allows easier discernibility. However, the advantage of the other technique is that it offers the opportunity to make a pre-evaluation without any computation at the pre-processing stage.

For the grid independence study, the energy dissipation ratios were assessed with different grid sizes with all of the air entrainment types; however, only the averaged values are presented below.

Table 4.2 Mesh independency comparison, standard VoF advection technique, AC=0.5

Description	Q (m^3/s)	Grid	Avrg. elaps. clock time /siml. time	Cumulative volume loss	Average energy loss	Average energy loss difference
Experiment	1.0				0.74818	0.00%
Constrained BC	1.0	M1	13	-0.007%	0.74994	-0.67%
Unconstrained BC	1.0	M1	5	-0.010%	0.74349	0.24%
Constrained BC	1.0	M2	68	0.010%	0.74732	-0.37%
Unconstrained BC	1.0	M2	57	0.000%	0.74295	0.33%
Constrained BC	1.0	M3	296	-0.002%	-0.00185	-0.23%
Unconstrained BC	1.0	M3	250	0.000%	0.74320	0.24%
Constrained BC	1.0	M4	839	-0.003%	0.74689	-0.23%
Unconstrained BC	1.0	M4	704	-0.003%	0.74313	0.28%
Experiment	3.0				0.69773	0.00%
Constrained BC	3.0	M1	7	0.023%	0.62860	9.22%
Unconstrained BC	3.0	M1	8	0.020%	0.60587	12.59%
Constrained BC	3.0	M2	71	0.010%	0.70156	-1.42%
Unconstrained BC	3.0	M2	67	-0.003%	0.70323	-1.42%
Constrained BC	3.0	M3	361	-0.010%	-0.00679	-1.10%
Unconstrained BC	3.0	M3	380	0.003%	0.69336	-0.05%
Constrained BC	3.0	M4	1028	0.003%	0.61552	10.81%
Unconstrained BC	3.0	M4	1161	-0.007%	0.68520	1.14%
Experiment	5.0				0.63475	0.00%
Constrained BC	5.0	M1	27	0.243%	0.53059	16.07%
Unconstrained BC	5.0	M1	12	0.000%	0.52324	17.23%
Constrained BC	5.0	M2	228	0.003%	0.49762	21.38%
Unconstrained BC	5.0	M2	203	0.007%	0.50502	20.19%
Constrained BC	5.0	M3	1056	0.000%	0.22619	20.96%
Unconstrained BC	5.0	M3	928	0.003%	0.49835	20.97%
Constrained BC	5.0	M4	3444	-0.003%	0.49955	21.03%
Unconstrained BC	5.0	M4	2166	0.007%	0.50657	19.72%

According to *Table 4.2* and the following figures, M3 is the clear appropriate mesh size for the simulation among the trials considering the averaged energy loss difference and averaged volume loss among the grids and the time limitation of the thesis.

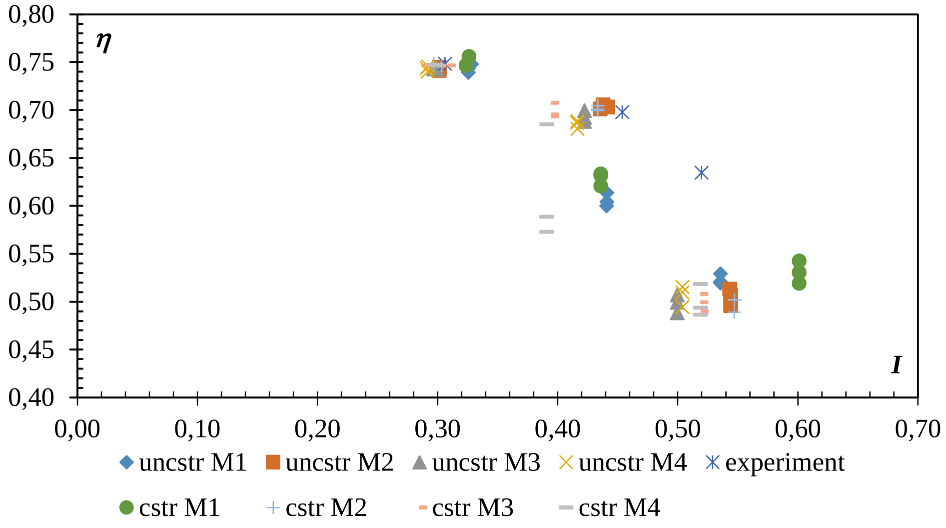

Figure 4.9 Energy dissipation comparison under various mesh types for Impact number

Almost all of the results in regime R1 yield right on target results; however, the results of regime R2 and R3 are not such well. Further comparison of the energy dissipation rate is discussed in the next sections to comprehend the phenomena.

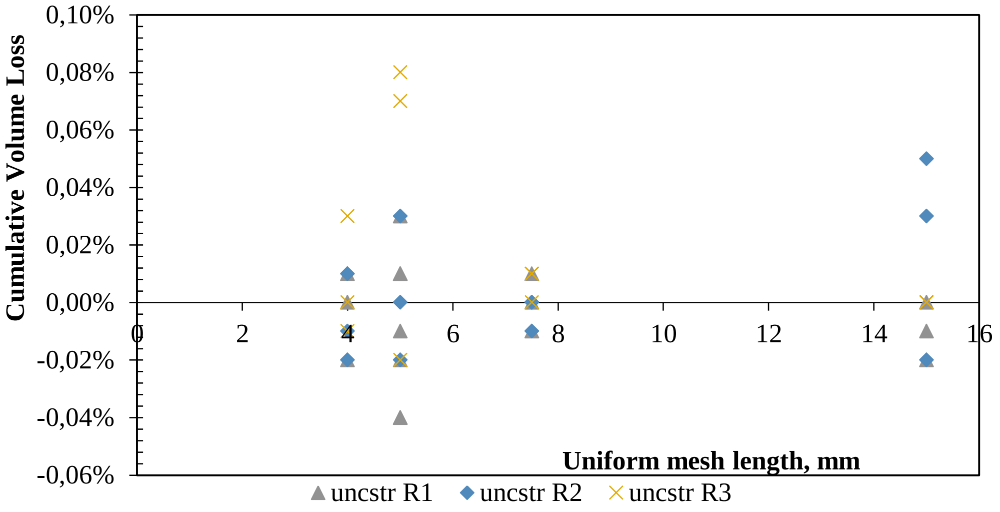

Figure 4.10 Cumulative volume losses on mesh sizes and regimes

According to *Figure **4.10***, it is shown that the smaller the grid the less the cumulative volume loss. It is noted that R3 is the remarkably worst case due to the split droplets after jet impingement on the opposite shaft wall.

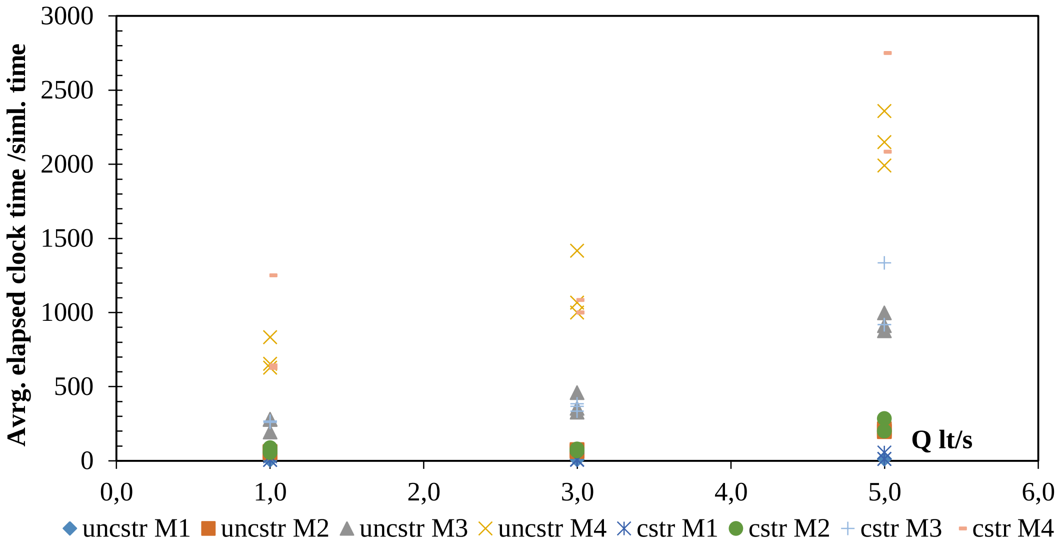

Figure 4.11 Simulation durations on grid types

Averaged elapsed clock time per simulation time stands for the ratio between the duration of the simulation computation and the determined simulation time. Therefore, the graphic shows how the smaller grid sizes boost the duration.

Finally, the Finer mesh M3 is determined for the investigation. The selection of air entrainment type is restricted as eb type just for the energy loss and impact number investigation on discharge rates due to the time consuming complex process of the dispersed bubble movement of ebf type. The effect of entrainment module activation is discussed in the next sections.

Table 4.3 Data of energy loss and impact number on various discharge rates

Description	Q (m^3/s)	Avrg. elaps. clock time /siml. time	Volume error (%lost)	H_1	H_0	y_0F_0	%loss	% loss difference	I	% I difference
Experiment	1.0		0	0.16172	0.64221	0.17659	0.74818	0.0%	0.30621	0.0%
Constrained BC	1.0	260	0.01%	0.16364	0.64424	0.18541	0.74600	0.3%	0.30137	1.6%
Unconstrained BC	1.0	193	0.03%	0.16595	0.64495	0.18697	0.74270	0.7%	0.29661	3.1%
Experiment	1.4		0.00%	0.16951	0.64999	0.21611	0.73921	0.0%	0.34678	0.0%
Constrained BC	1.4	280	-0.01%	0.17166	0.65272	0.22376	0.73701	0.3%	0.33458	3.5%
Unconstrained BC	1.4	275	0.00%	0.17300	0.65258	0.22177	0.73489	0.6%	0.33296	4.0%

Experiment	1.9		0.00%	0.17823	0.65867	0.25715	0.72941	0.0%	0.38234	0.0%
Constrained BC	1.9	301	-0.02%	0.18122	0.66218	0.26171	0.72633	0.4%	0.36073	5.7%
Unconstrained BC	1.9	294	0.01%	0.18307	0.66210	0.26145	0.72350	0.8%	0.36114	5.5%
Experiment	2.0		0.00%	0.18015	0.66115	0.25770	0.72752	0.0%	0.37202	0.0%
Constrained BC	2.0	296	-0.01%	0.18351	0.66436	0.26593	0.72378	0.5%	0.35856	3.6%
Unconstrained BC	2.0	311	-0.03%	0.18526	0.66450	0.27047	0.72121	0.9%	0.36305	2.4%
Experiment	2.2		0.00%	0.18380	0.66477	0.27238	0.72351	0.0%	0.38025	0.0%
Constrained BC	2.2	295	0.00%	0.18675	0.66687	0.28730	0.71996	0.5%	0.38475	-1.2%
Unconstrained BC	2.2	308	-0.01%	0.18869	0.66655	0.28418	0.71691	0.9%	0.38337	-0.8%
Experiment	2.5		0.00%	0.18746	0.66932	0.29133	0.71992	0.0%	0.39468	0.0%
Constrained BC	2.5	324	-0.07%	0.19006	0.67190	0.30223	0.71714	0.4%	0.39039	1.1%
Unconstrained BC	2.5	325	0.01%	0.19196	0.67195	0.30207	0.71432	0.8%	0.38986	1.2%
Experiment	2.9		0.00%	0.20545	0.67475	0.32134	0.69551	0.0%	0.42131	0.0%
Constrained BC	2.9	362	0.00%	0.19557	0.67835	0.32752	0.71170	-2.3%	0.40497	3.9%
Unconstrained BC	2.9	352	0.00%	0.19340	0.67740	0.33381	0.71450	-2.7%	0.41913	0.5%
Experiment	3.0		0.00%	0.20393	0.67465	0.34070	0.69773	0.0%	0.45394	0.0%
Constrained BC	3.0	364	0.04%	0.20194	0.68150	0.33109	0.70369	-0.9%	0.39493	13.0%
Unconstrained BC	3.0	353	0.03%	0.21176	0.67926	0.34187	0.68825	1.4%	0.42246	6.9%
Experiment	3.4		0.00%	0.22784	0.68085	0.35984	0.66536	0.0%	0.45757	0.0%
Constrained BC	3.4	316	-0.02%	0.22251	0.68573	0.35895	0.67551	-1.5%	0.42528	7.1%
Unconstrained BC	3.4	299	-0.01%	0.22411	0.68525	0.36172	0.67296	-1.1%	0.43138	5.7%
Experiment	3.8		0.00%	0.25938	0.68605	0.38593	0.62192	0.0%	0.47657	0.0%
Constrained BC	3.8	301	0.01%	0.23830	0.68996	0.38932	0.65461	-5.3%	0.45632	4.2%
Unconstrained BC	3.8	296	-0.02%	0.23598	0.69105	0.38547	0.65852	-5.9%	0.44503	6.6%
Experiment	4.2		0.00%	0.25863	0.69218	0.40365	0.62635	0.0%	0.47866	0.0%
Constrained BC	4.2	711	0.03%	0.31285	0.69415	0.41574	0.54931	12.3%	0.48204	-0.7%
Unconstrained BC	4.2	819	0.00%	0.31748	0.69521	0.41279	0.54333	13.3%	0.47178	1.4%
Experiment	4.3		0.00%	0.23733	0.69342	0.40966	0.65774	0.0%	0.48283	0.0%
Constrained BC	4.3	749	-0.01%	0.31449	0.69552	0.42243	0.54784	16.7%	0.48614	-0.7%
Unconstrained BC	4.3	726	0.00%	0.30277	0.69553	0.42236	0.56469	14.1%	0.48603	-0.7%
Experiment	4.9		0.00%	0.24593	0.70068	0.44738	0.64902	0.0%	0.50966	0.0%
Constrained BC	4.9	911	-0.02%	0.35254	0.70252	0.46065	0.49817	23.2%	0.51571	-1.2%
Unconstrained BC	4.9	909	0.01%	0.35026	0.70385	0.45667	0.50236	22.6%	0.50303	1.3%
Experiment	5.0		0.00%	0.25618	0.70139	0.45651	0.63475	0.0%	0.52006	0.0%
Constrained BC	5.0	932	0.01%	0.34832	0.70370	0.46619	0.50502	20.4%	0.51943	0.1%
Unconstrained BC	5.0	910	0.07%	0.34793	0.70600	0.48420	0.50718	20.1%	0.52446	-0.8%

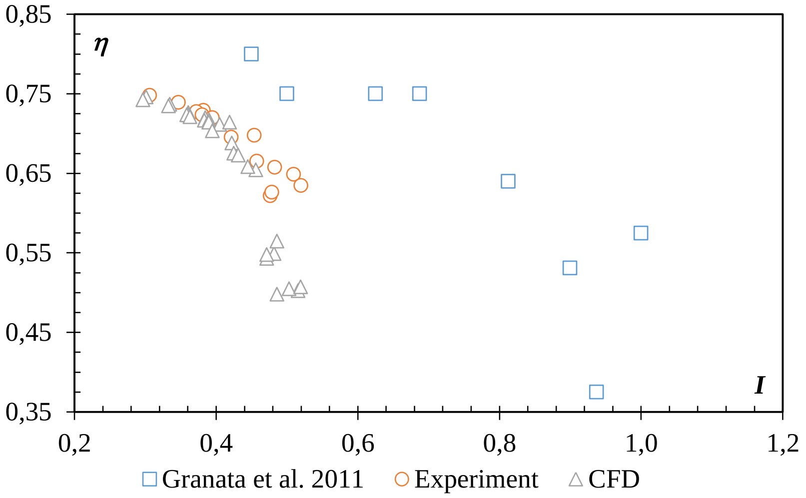

Figure 4.12 Energy dissipation comparison with Granata et al. 2011

Considering the differences in the experimental conditions of Granata *et al.* and the experimental study such as the subcritical-supercritical flow condition contrast, the disharmony in the results can be understood. Besides, relative to this judgment, it can be stated that the compatibility of the CFD-Physical experiment in this figure is self-consistent.

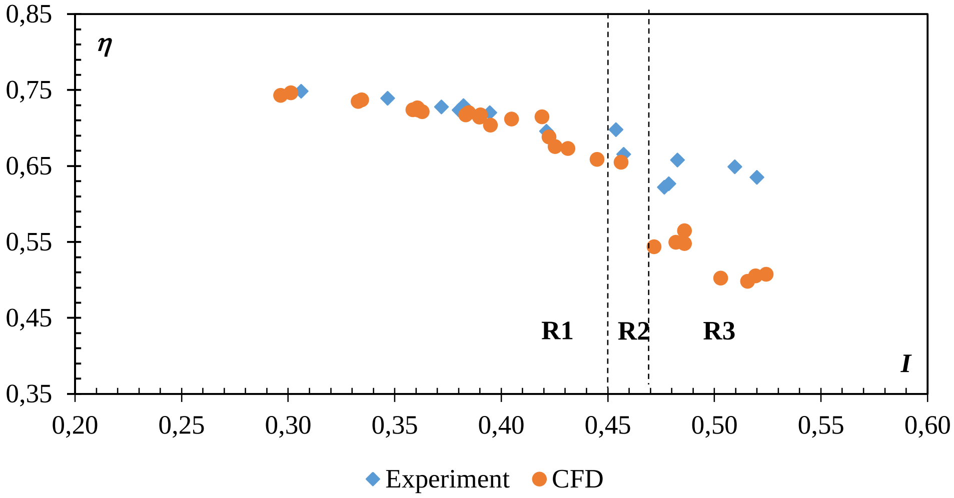

Figure 4.13 CFD energy dissipation compatibility

*Figure **4.13*** is graphed with the data obtained in *Table **4.3*** by the use of various discharges with the same drop height (s). As it is obviously seen from the graph, R1 regime is comparatively efficient than the other regimes through energy dissipation and the CFD results in this regime are compatible with the experiment. As the R2 regime bypasses the shaft due to conditions specified in nature, its interaction is little and the energy dissipation only centres at the intake of the outlet pipe. CFD simulation results on this regime are tolerable regarding the narrow impingement location range. Energy dissipation results of CFD regime R3 are relatively poorer, this is possibly due to the complex turbulent nature of the regime which is identified by the impingement of the opposite wall formerly falling into bits to the shaft. The simulation of this scattered and disintegrated two-phase flow is rather costly in time consumption, check *Figure **4.15***.

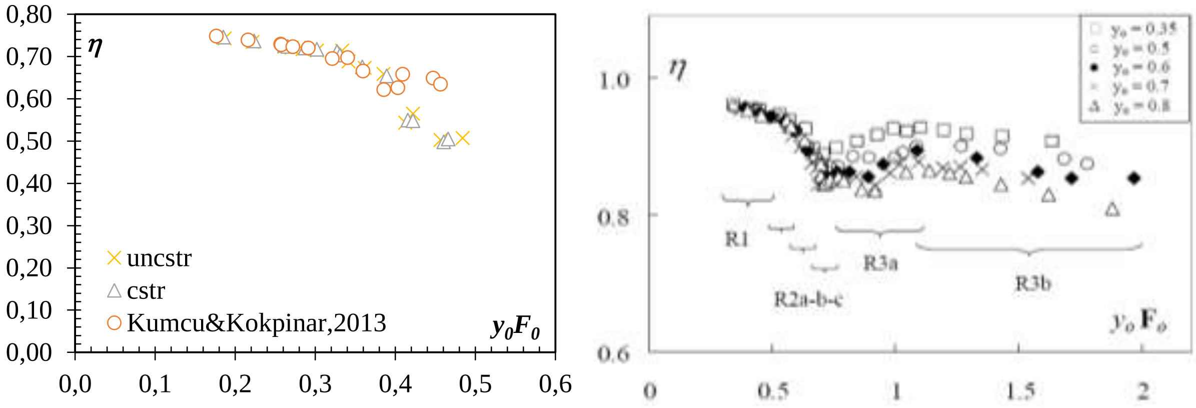

Figure 4.14 Comparison of results with the supercritical condition of De Marinis *et al.* 2007

*Figure **4.14*** reveals that the energy dissipation behaviour of subcritical and supercritical flows in dropshafts distinct from each other. Moreover, both the constrained and the unconstrained condition CFD results overlap each other, which implies independence of boundary condition constraint. More comparisons made on constraints are given in *Figure **4.15*** and *Figure **4.16***.

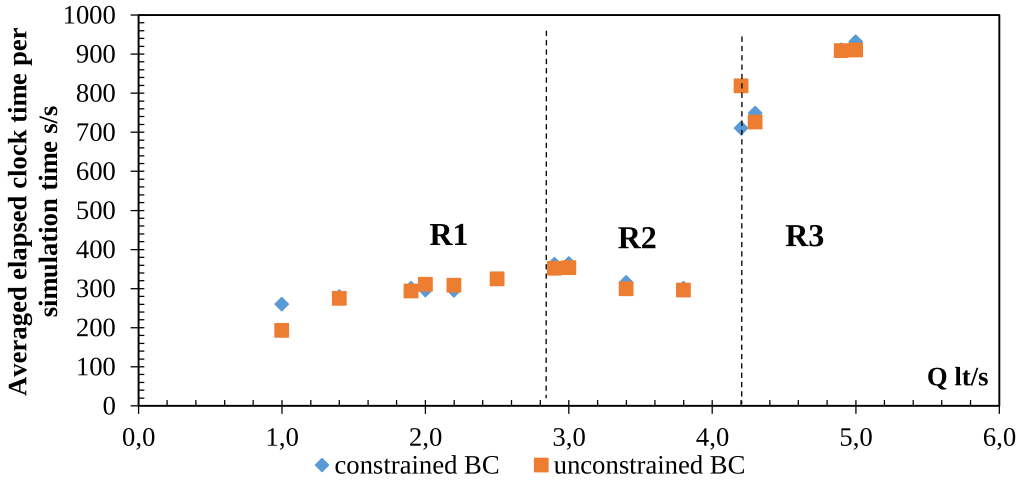

Figure 4.15 The effect of discharge on time consumption

Due to the bypass nature of Regime R2, *Figure **4.15*** indicates that the computation of regime R2 is relatively cheaper in terms of time consumption in contrast with the discharge increment. No circulation occurred at the computational domain around the shaft pool and the pool is almost not disturbed, which consequently reduced the allocated dynamic memory.

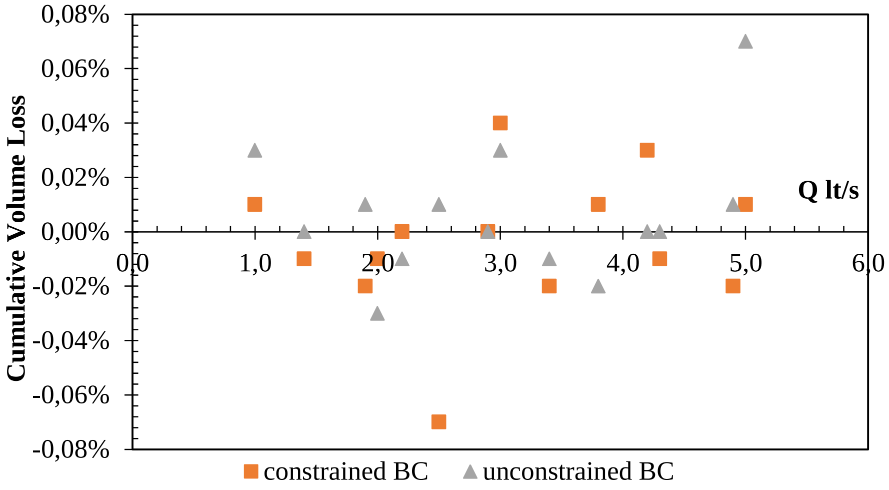

Figure 4.16 Computational efficiency of volume advection in both conditions

Considering *Figure **4.13***, *Figure **4.15*** & *Figure **4.16***, the independence of the boundary condition constraint is revealed. However, the constrained boundary condition is selected for further computations due to the judgment of compatibility.

The effects of the volume advection technique on energy dissipation were discussed in the next section and the whole data table investigated for each constrained BC condition is given in Appendix-A. A similar table with elevation non-constrained BC conditions is given in Appendix-B.

4.2 VoF Advection Comparison

As introduced in detail in section 3.2.2., Volume-of-Fluid advection options are utilized to control how the fluid surface moves through the domain. To determine the location of the free surface and to evaluate the distribution of energy dissipation and aeration, which will vary depending on the free surface location, a comparison of the three VoF advection techniques was made. Considering basic beneficial comparison for VoF advection techniques, the Aeration Coefficient (AC) is primarily determined as the constant value of 0.50. To show the free surface location, impingement points of the advection techniques in each regime is presented below. All the mesh grids given in the figures are sized as an M3 type grid, 5 mm.

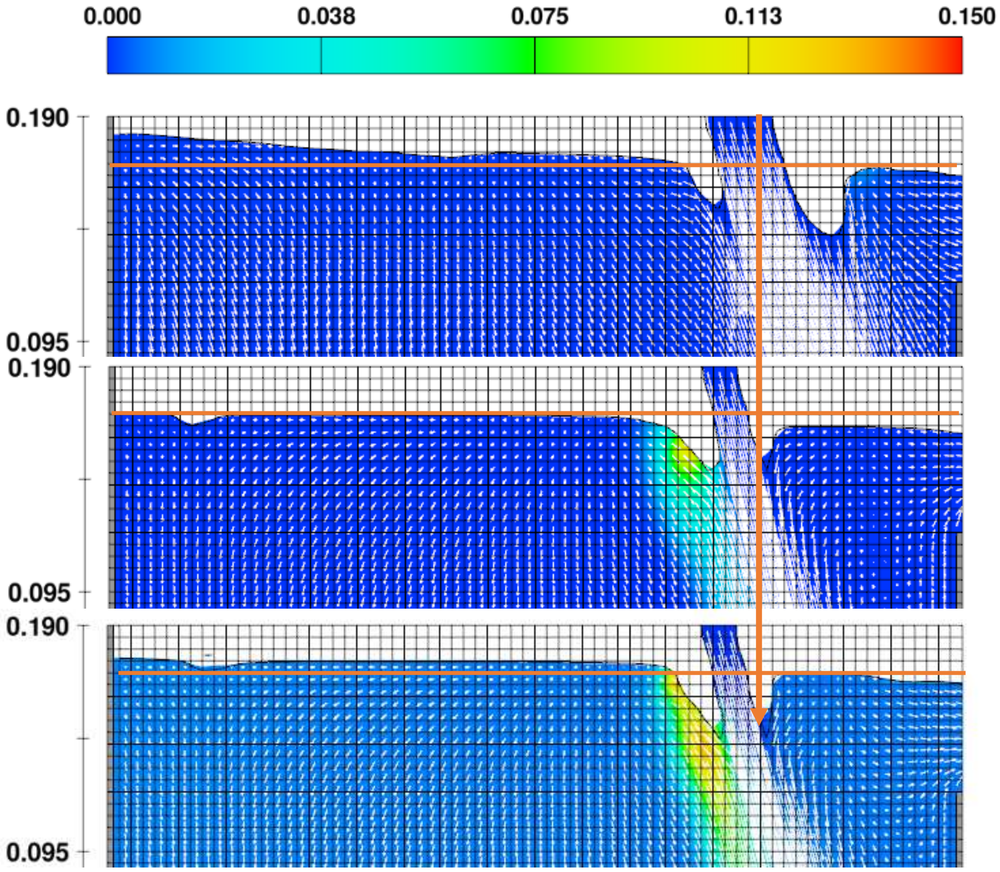

Figure 4.17 R1 regime profile view at the centreline, Standard, Unsplit, Split VoF advection techniques, velocity vectors, impingement location and coloured scale aeration for eb type, AC=0.5.

According to the reference lines and the mesh grid distribution, one can simply understand the difference between the jet thicknesses, impingement locations and pool heights. The Lagrangian VoF advection techniques show similar jet thicknesses and similar impingement locations under the same drop height of *s*=48 cm. However, the standard technique jet thicknesses and impingement location are distinctly different. The jet thickness ratio in the profile view is almost 2 cm and the displacement of the impingement location centre is almost 1 cm, in the manhole with a diameter of 35.5 cm. There is no experimental data to evaluate the matching jet thickness. The entrained air distribution illustrated with colour is also distinct among the techniques and presumably relevant to the jet thickness and the jet velocity. In the light of equations 3.5-3.6-3.7, mentioned in section 3.2.1.2, air entrainment is directly associated with turbulence level and stability force, so the jet velocity gains importance in the computation of air entrainment. Still, the jet thicknesses of both Lagrangian techniques are similar and the distinct coloured aeration distribution around the impingement claimed to be transiently different; however, the colour distribution of the rest of the pool (see also *Figure **4.18***) proofs the effects of advection techniques on air entrainment in contrast with the absence of apparent contribution in the equations.

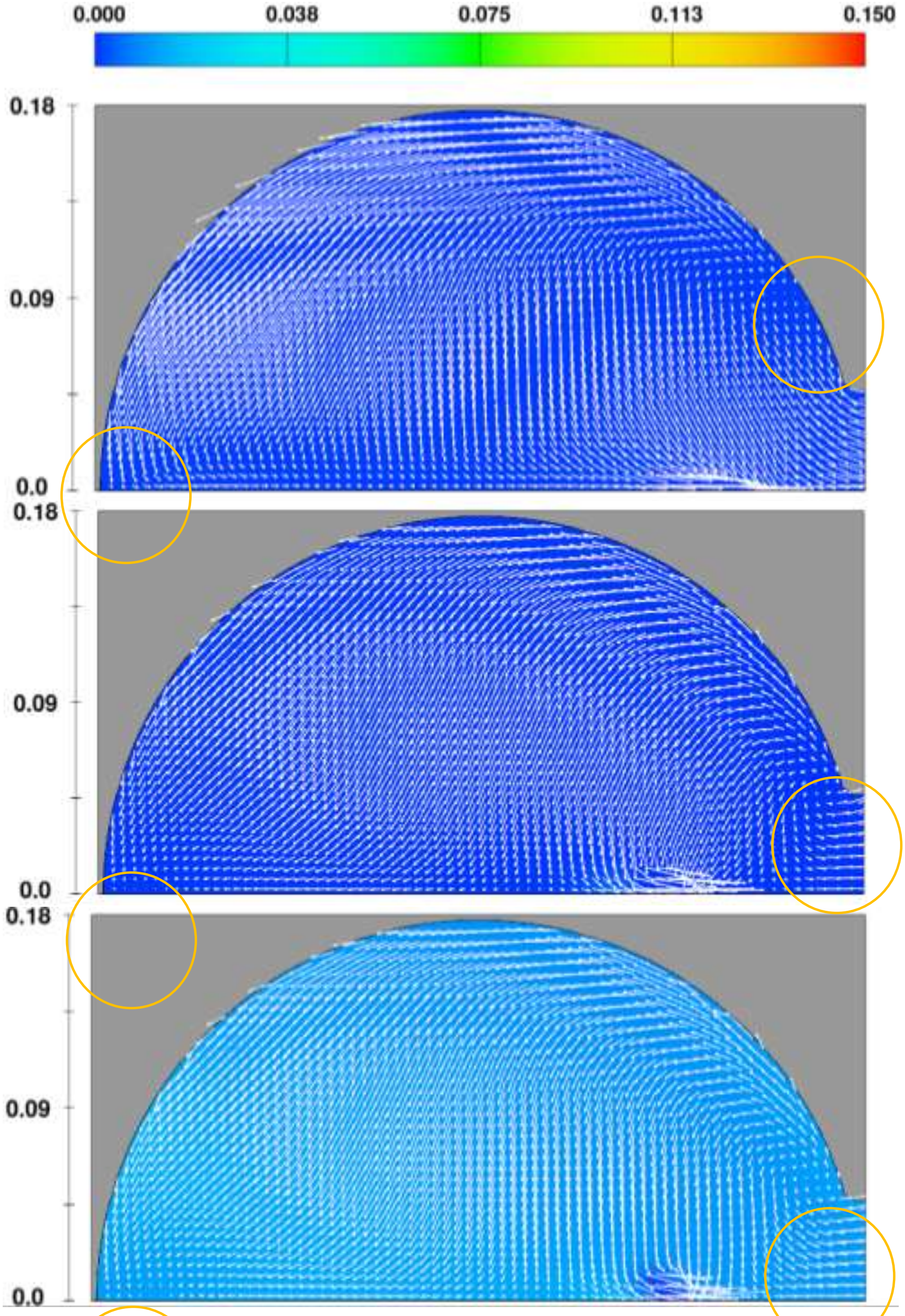

Figure 4.18 R1 regime plan view at z1=0.1410 height, Standard, Unsplit L. & Split L. VoF advection techniques, velocity vectors & coloured scale aeration for eb type, AC=0.5.

A similar velocity field is observed among the Lagrange advection techniques in *Figure* ***4.18***. The standard technique is distinguished by the centre of vortical and so-called stagnant locations and associated redistributed velocity field in the regime R1.

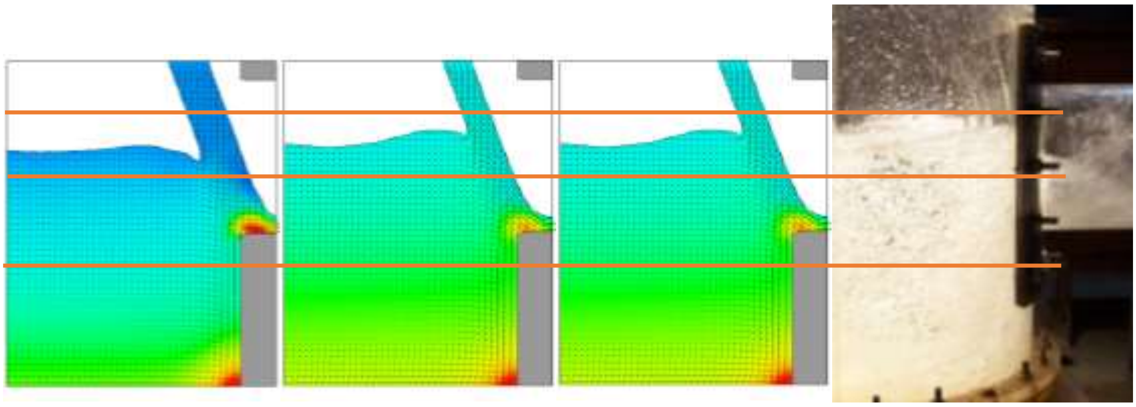

Figure 4.19 R2 regime: Standard - Unsplit L. & Split L. techniques, coloured by pressure to show impingement location.

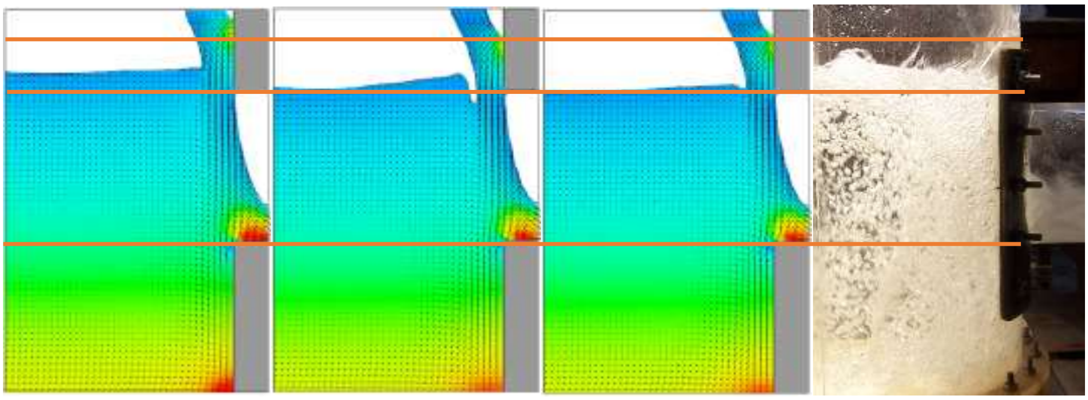

Figure 4.20 R3 regime: Standard - Unsplit L. & Split L. techniques, coloured by pressure to show impingement location.

In *Figure* ***4.17*** & *Figure* ***4.19***, the pool heights of Lagrangian advection techniques are almost equal. The pool height of the Standard technique is higher in regimes R1 & R3, which of both is pool-centred regimes in contrast with pool-bypassed regime R2. Compared to the experiment, *Figure* ***4.20*** proves the compatibility of the Standard technique in pool height. Variation in the intensity of red colour in *Figure* ***4.19*** & *Figure* ***4.20*** shows the similar displacement in R1 is valid for here also.

Detailed computational differences of the VoF advection approaches are graphed in *Figure* ***4.21***, which reveals how high the cumulative volume loss in the Unsplit Lagrangian technique as declared by the user guide in section 3.2.2.

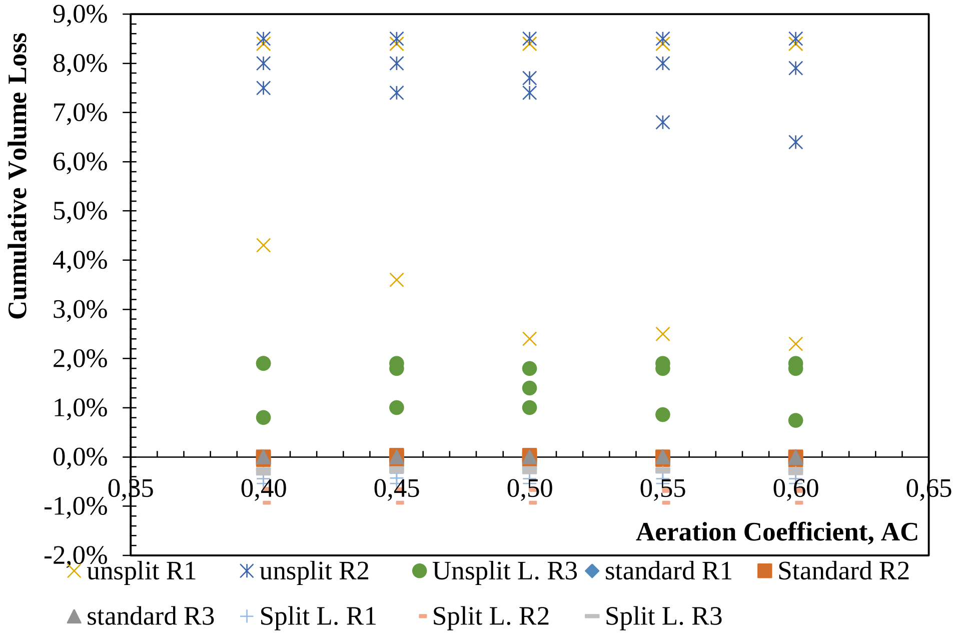

Figure 4.21 Volume loss comparison between VoF advection techniques

The figure expresses that the Unsplit Lagrangian technique produces substantial cumulative volume error comparative to the other approaches in all regimes. The most accurate results are achieved by the standard technique, which produces unimportant volumetric losses under %0.1 averagely. To offer a more broad valuation, detailed graphs are given for Lagrangian techniques with each aeration type in the following figures.

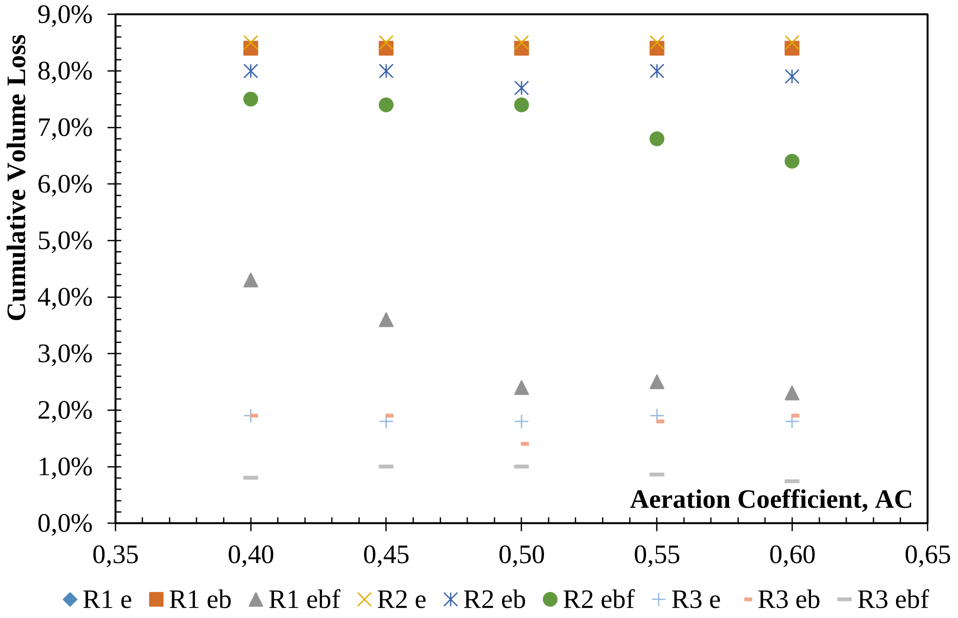

Figure 4.22 Cumulative volume loss on aeration types for Unsplit L. VoF advection technique

Figure 4.22 shows that the cumulative volume loss of the Unsplit Lagrangian technique generates remarkably less cumulative volume loss for ebf type aeration in regime R1. Not as significant as in R1 but still noticeable that the ebf type aeration is preferable for regimes R2 and R3 also. The Unsplit Lagrangian VoF advection technique produces overall better outcomes amongst the regimes for the R3 regime which is fluid-solid collision more than fluid-fluid collision.

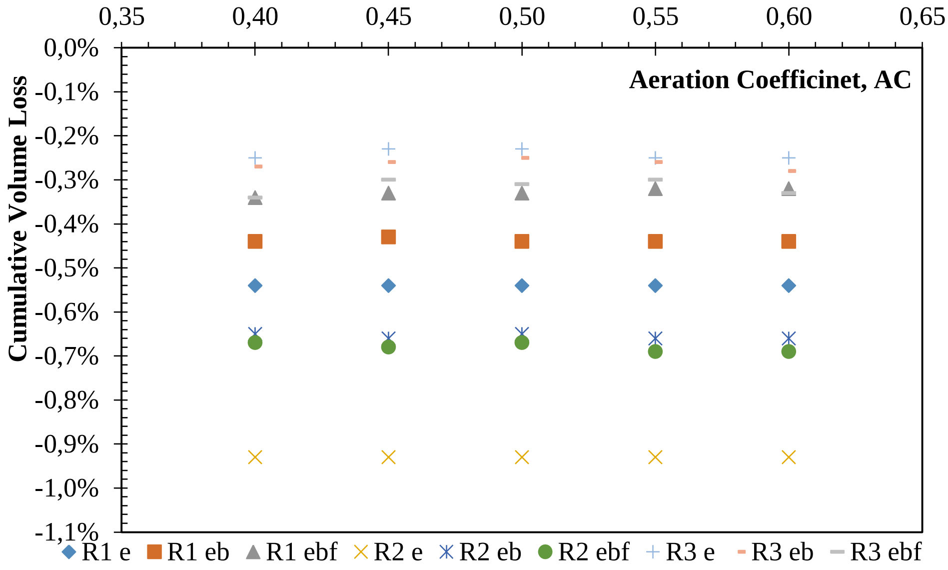

Figure 4.23 Cumulative volume loss on aeration types for Split L. VoF advection technique

Contrary to the previous comparison, the Split Lagrangian VoF advection technique provides negative cumulative volume losses, which means there is an increase in volume. The technique is not consistent to offer any type of aeration for each condition, but the averaged values signals that both the eb and ebf type is preferable. Similar to the Unsplit Lagrangian VoF advection technique, this technique also yields overall better solutions for the R3 regime. Besides, there is no direct relation between the aeration coefficient and the cumulative volume loss.

Figure 4.24 displays the relation between the computational duration and VoF advection techniques. The higher computational cost of regime R3 is basically due to the bigger discharge and turbulence of the regime characteristic. The computational cost of the standard technique is the smallest and the cost of the Unsplit Lagrangian technique is the highest in general.

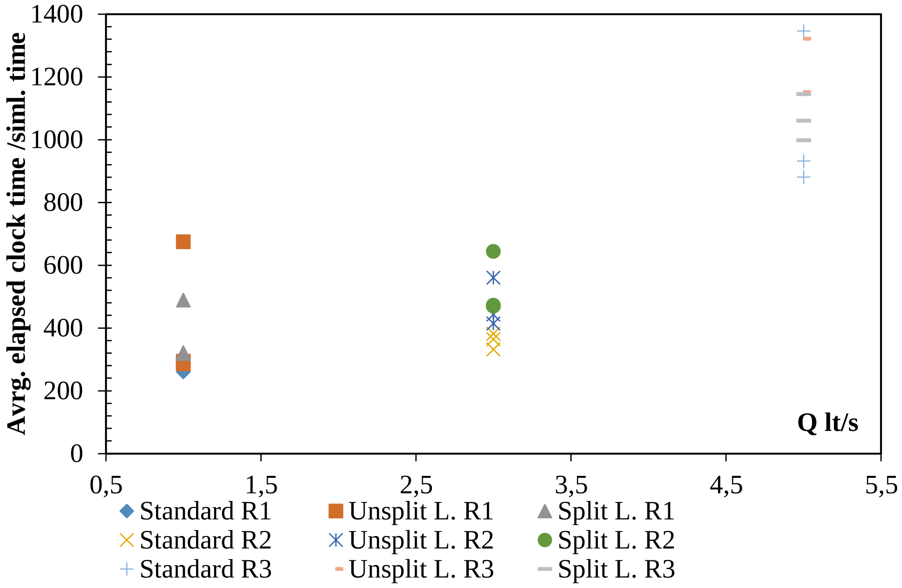

Figure 4.24 Simulation duration relative to Q and VoF advection techniques

4.3 Air Entrainment

To approximate the fluid flow aeration, several options under the air entrainment module is utilized (Kumcu & Ucar, 2017). The air entrainment module works without requiring a long-lasting two-phase solution. Within the scope of this thesis, three different sub-options under the air entrainment module is examined to validate the compatibility of the code with realistic air bubble behaviour in the complex dropshaft flows:

a) The basic “passive” empirical model, neglects entrained air mass & volume

b) Bulking option activated model, enables density variation with entrained air volume & mass, neglects complicated physics and motion of air bubbles

c) Drift flux activation enables creating physical air bubbles and traces the motions under buoyancy, drag and momentum effects.

4.3.1 Passive and Active option comparison

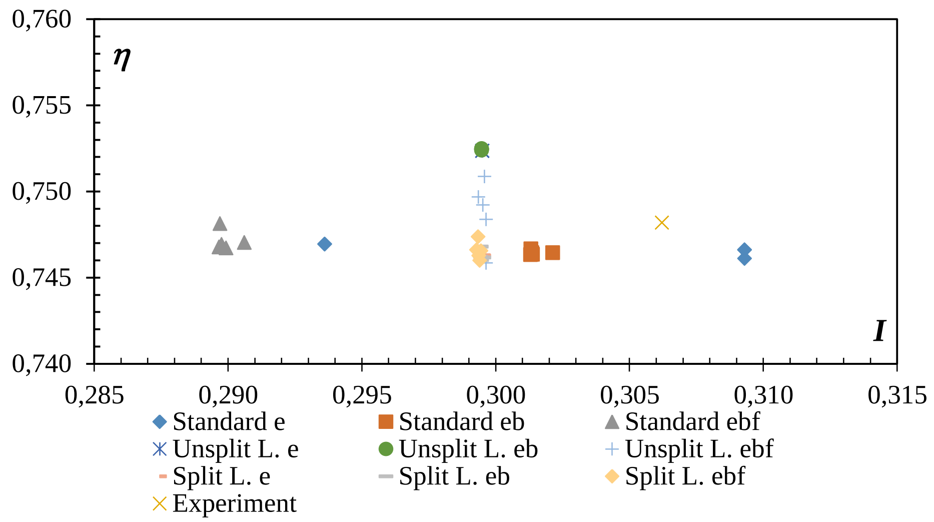

Figure 4.25 Passive and active air entrainment compatibilities on energy dissipation for Regime R1

The graphic related to energy dissipation on impact number for R1 regime shows quite coinciding results around the experiment, the average difference for standard e is -0.19% for η and 1.04% for I. The furthest points have a 5.3% difference in standard technique ebf for I and -0.95% in Unsplit L. Eb for η.

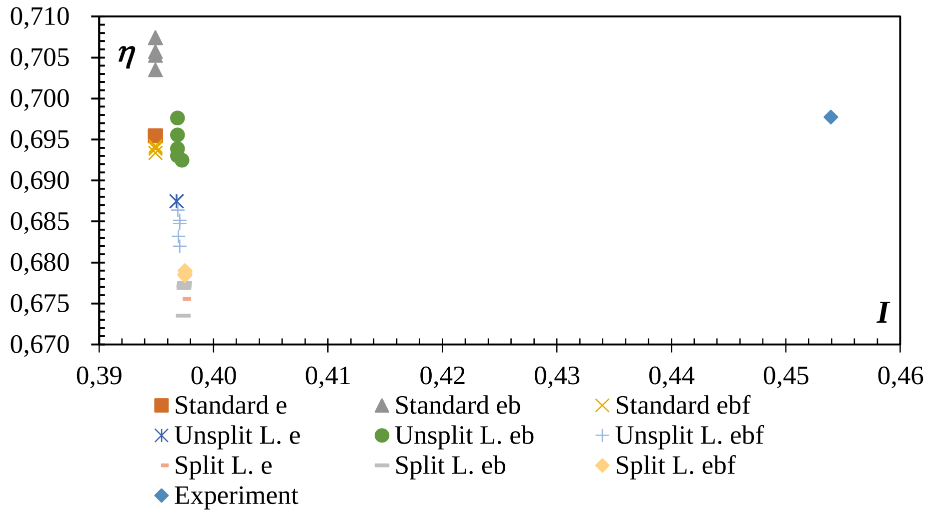

Figure 4.26 Passive and active air entrainment compatibilities on energy dissipation for Regime R2

The figure displays distinct impact number results for R2 simulations concerning the experimental measurements; yet, the standard deviation of the computational results is %0.3, which is remarkably consistent. The difference for energy dissipation rate is better than regime R1, 0.42% on average.

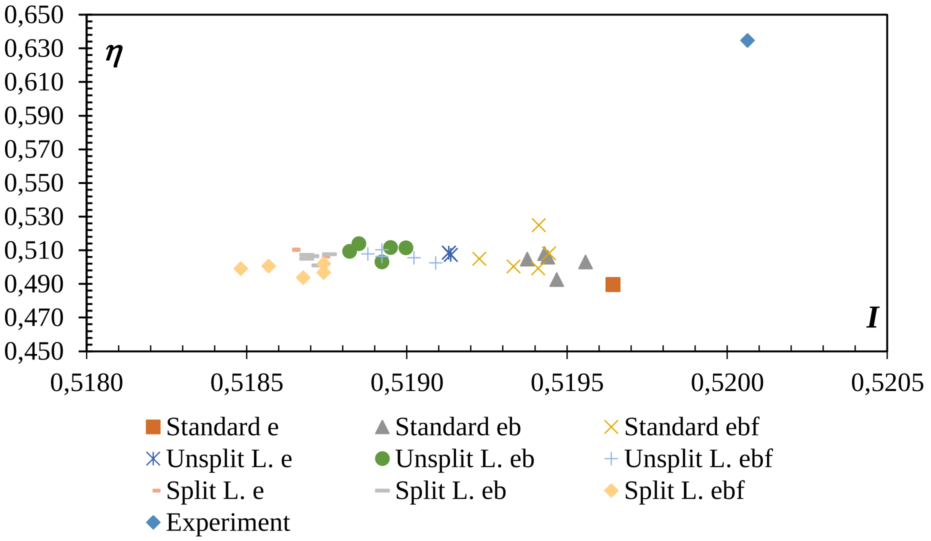

Figure 4.27 Passive and active air entrainment compatibilities on energy dissipation for Regime R3

The results demonstrate dissimilar energy dissipation ratios for R3 solutions relative to the experiment; yet, the standard deviation of the CFD results shows a remarkably consistent behaviour %0.9. The difference for the impact number is 0.19% on average.

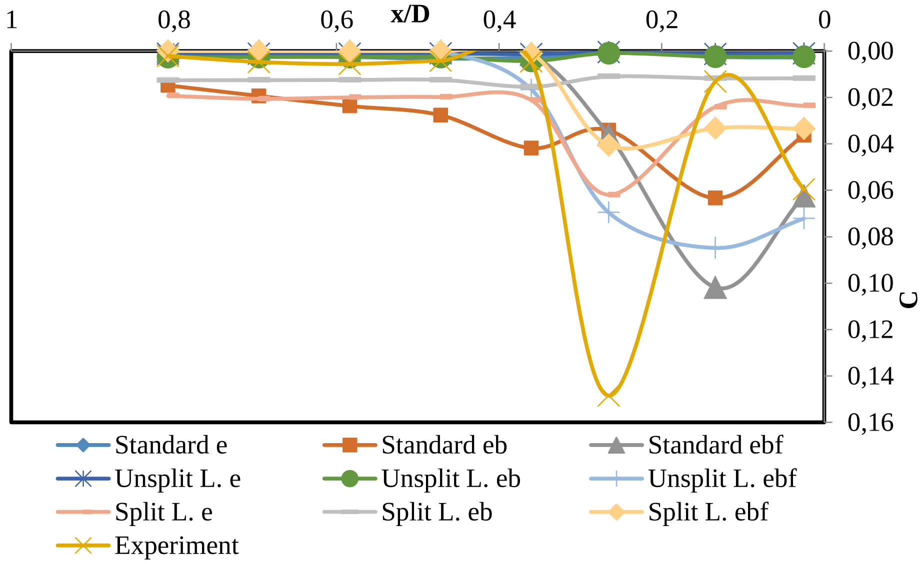

Figure 4.28 Passive and active air entrainment compatibilities on measurement points for Regime R1

While the results of the CFD is far from the experiment in general, the lines of Split L. ebf and Split L. e shows parallel results, which hints the parameters of the advection technique needs to be studied.

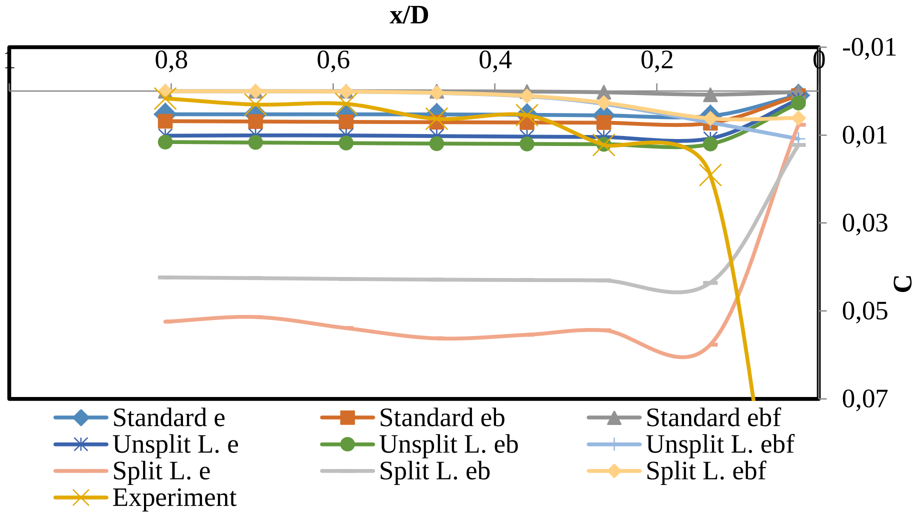

Figure 4.29 Passive and active air entrainment compatibilities on measurement points for Regime R2

At the less turbulent part, the measurements of CFD and experiment more or less fit; still, the results of the last measurement point is irrelevant. This can be fixed by knowing the precise quantity of protrusion length to determine the point of impact (check *Figure* ***4.1***). The need for the knowledge for point of impact is because of the existence of aeration phenomena, which is directly linked to the balance between the stability force and instability force at the free surface. *Figure* ***4.17*** demonstrates that there is a curtain layer of air entrainment separating the jet centre from the aeration zone, so the results extremely depended on positional accuracy.

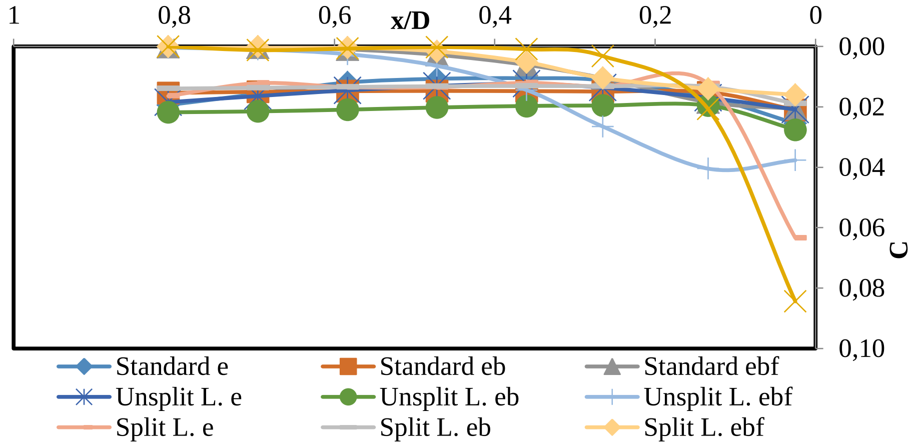

Figure 4.30 Passive and active air entrainment compatibilities on measurement points for Regime R3

Studies on the Regime R3 reveals parallel results for CFD except for the Unsplit Lagrangian technique with ebf type aeration and Split Lagrangian technique with e type aeration. The different results can also be clarified by impact location, the splinter of water jet scatters droplets in a complicated manner and the dependency of computation upon the VoF advection.

The deduction of Hirt (2014) is intended to be argued by the results of this thesis. Although the unsteadiness of this case is incompatible with the case of Hirt, quite different results obtained from the passive and active options. Further information for better approximation regarding the aeration coefficient is discussed in the following section.

4.3.2 Aeration coefficient effect

As presented in the previous sections, the numerical modelling studies coincides with the experimental measurements within an acceptable range of errors, through the water profiles obtained in the R1, R2 and R3 regimes. Until now, the Aeration Coefficient (AC) was determined as 0.50 and the computations were made upon this value. Four more ACs, 0.40, 0.45, 0.55 and 0.60 are preferred to assess the sensitivity of void ratio (C) of the coefficient of aeration for each e, eb, ebf type aerations under Standard, Split & Unsplit Lagrangian VoF advection techniques for each regime. Several simulations were carried out to guide the further air entrainment studies on dropshafts and plunging jets.

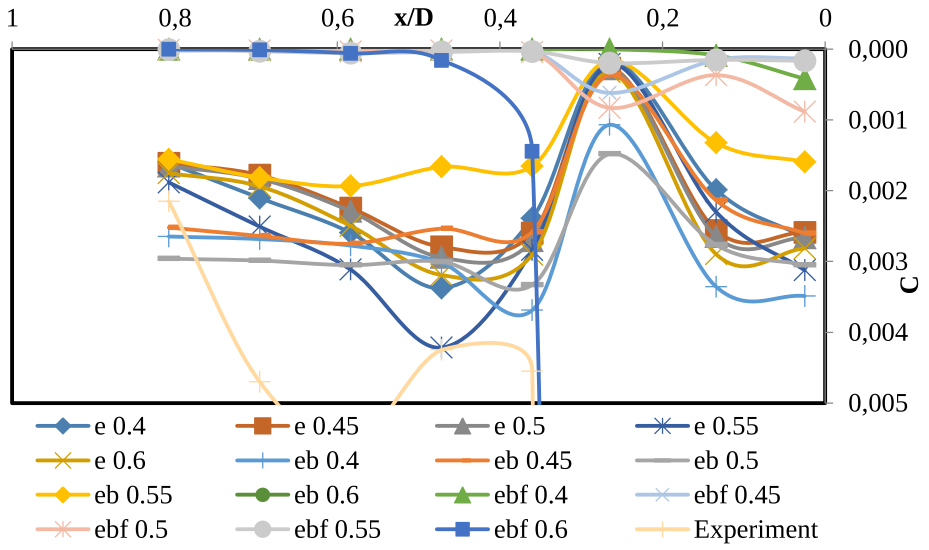

Figure 4.31 AC effect on entrained air distribution for R1 regime Standard VoF advection technique, compare with Figure **4.28**

Comparing *Figure* ***4.28***, this figure shows that the distribution of aeration measured at the probe locations is fairly distant from the experimental results; still, the results are intensified except the ebf type aeration. Regarding the explanations following *Figure* ***4.29***, the contrast between the expected peak and the bottom is reasonable.

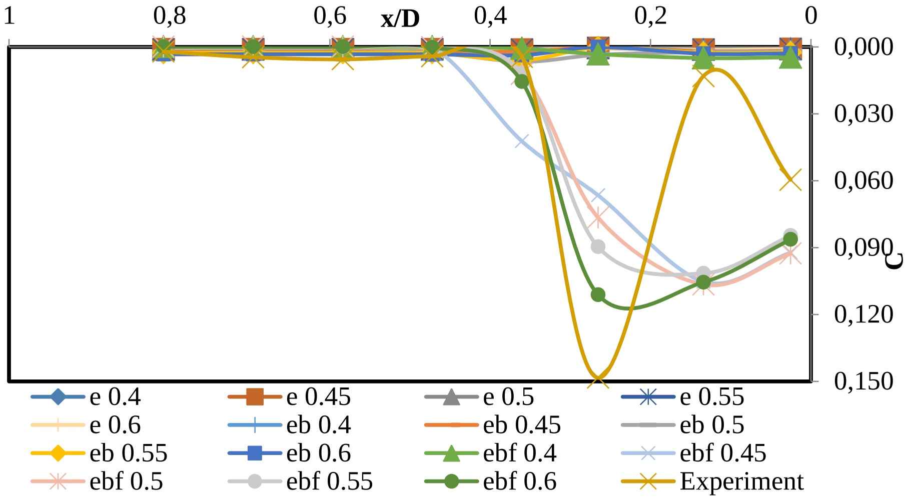

Figure 4.32 AC effect on entrained air distribution for R1 regime Unsplit L. VoF advection technique

Comparative to the Standard technique, the Unsplit Lagrangian VoF advection technique offers healthier results for Regime R1 with ebf type air entrainment. Comparing to the previous figure, ebf type aeration separates from the others for this case also.

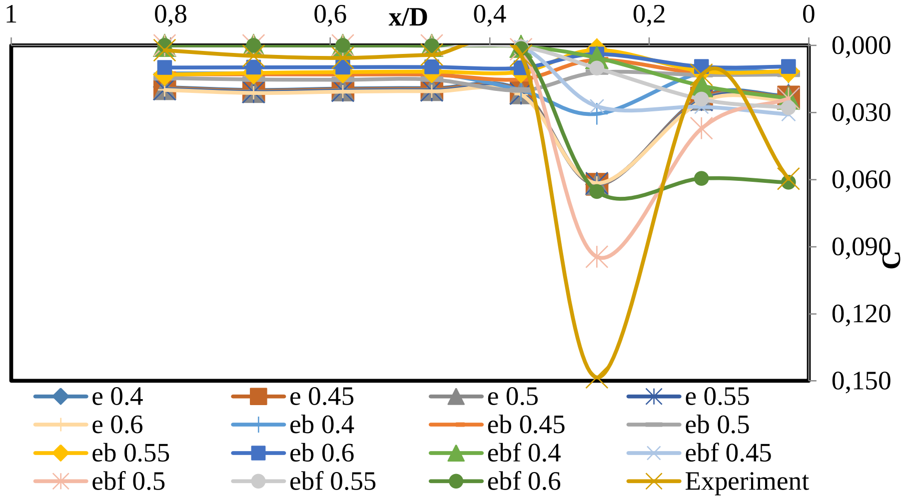

Figure 4.33 AC effect on entrained air distribution for R1 regime Split L. VoF advection technique

Whereas the non-proportional aeration distribution amongst the aeration types and aeration coefficients, the peak point of most of the trials are at the same vertical line. The most compatible result among the VoF advection techniques is obtained by the ebf type aeration with an aeration coefficient of 0.5. Besides, e type aeration results are overlapping.

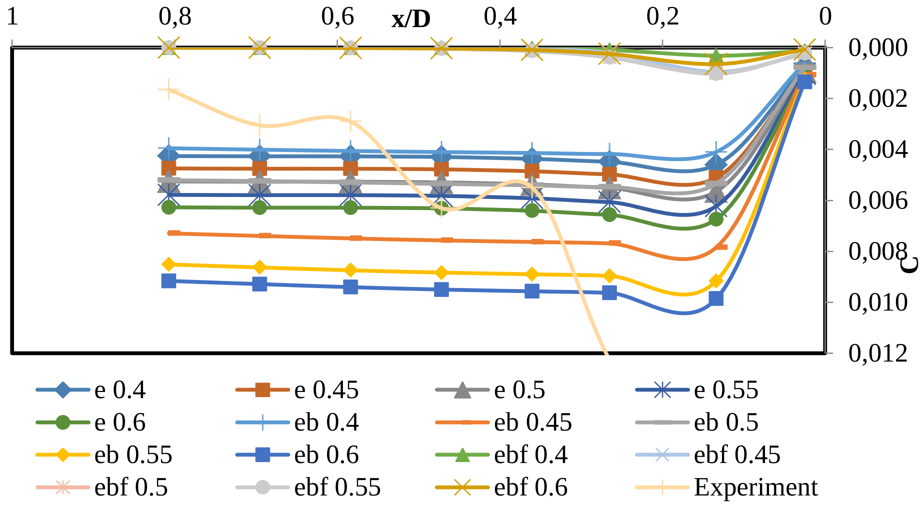

Figure 4.34 AC effect on entrained air distribution for R2 regime Standard VoF advection technique, compare with Figure 4.29

While the experimental results seem far from the CFD, comparing with the Standard VoF solution of regime R1, the figure has parallel aeration distribution lines due to the less turbulent characteristics of regime R2. Hence, it is easy to state that the AC effect on air entrainment computation for less turbulent zones is clear, smooth and proportional.

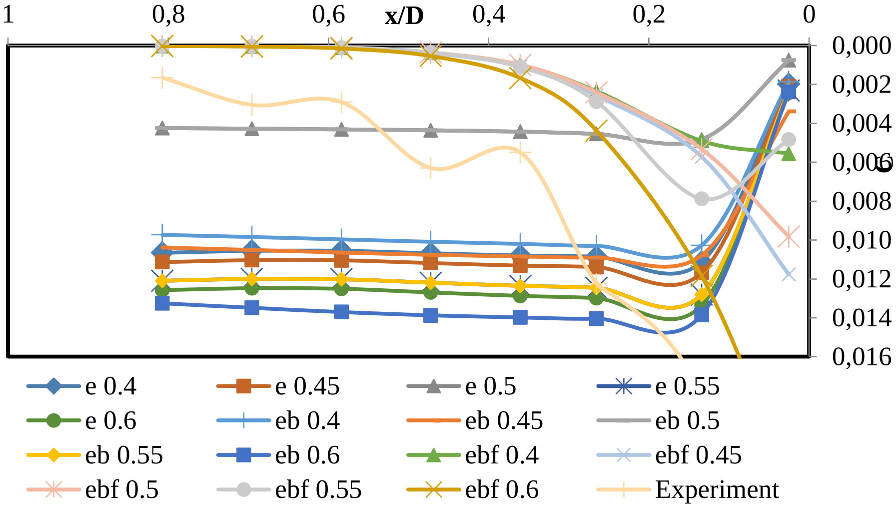

Figure 4.35 AC effect on entrained air distribution for R2 regime Unsplit L. VoF advection technique

Contrary to the rest, ebf type aeration is converging to the experimental measurement. While the VoF advection technique is the same for the whole lines in the graph, a simultaneous undulation may lead to such a result. The proportionality between the aeration types e & eb is broken by the couple for AC=0.5.

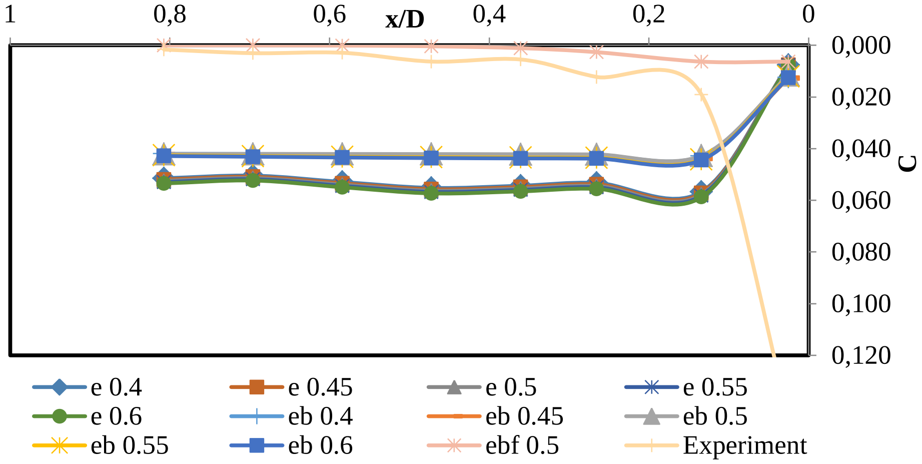

Figure 4.36 AC effect on entrained air distribution for R2 regime Split L. VoF advection technique

Unlike the case in regime R1, the Split Lagrangian VoF advection technique supplies parallel and self-consistent results for the same aeration types with variable aeration coefficients due to the mentioned regime characteristics. The change in aeration coefficient results in small variability alike in regime R1, e type aeration. ebf type aeration presents the most realistic results considering the comments about aeration near the impact location of *Figure **4.29***.

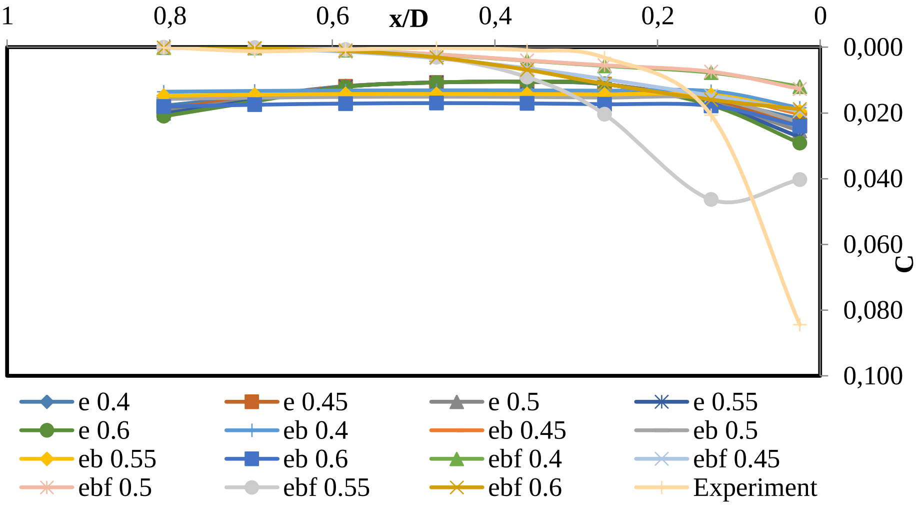

Figure 4.37 AC effect on entrained air distribution for R3 regime Standard VoF advection technique

The standard technique produces the best results for regime R3 among the regimes, yet, the peak points are fairly distant from each other. Bearing in mind that the poorest energy dissipation results are obtained by this regime, and different water levels in the pool, the difference is understandable. Comparing with *Figure* **3.2**, the most aerated zone is at the free surface and the air distribution at the z4 elevation could not be measured by CFD because of the pool height problem.

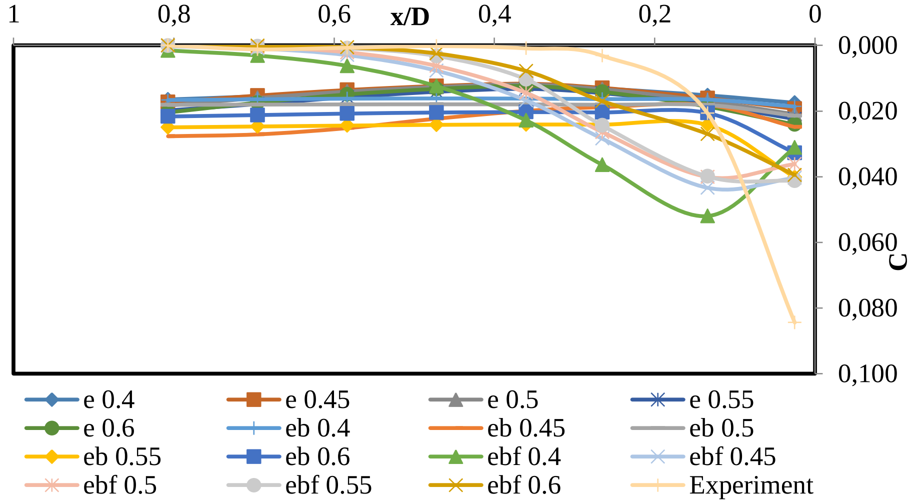

Figure 4.38 AC effect on entrained air distribution for R3 regime Unsplit L. VoF advection technique

Bearing in mind the loss in the volume for the Unsplit Lagrangian VoF advection technique and the parallel results obtained from seven measurement points, the results for ebf type aeration yields relatively acceptable.

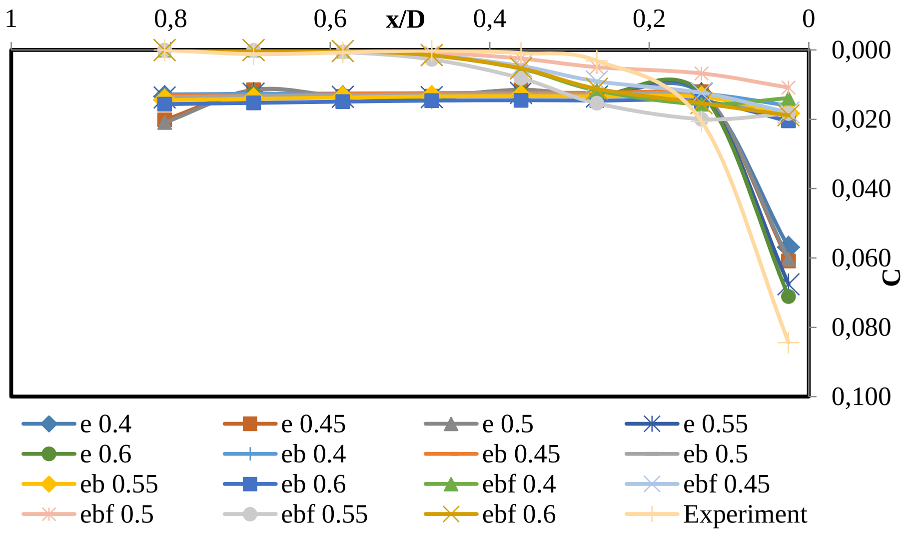

Figure 4.39 AC effect on entrained air distribution for R3 regime Split L. VoF advection technique

Quite compatible results are achieved by the Split Lagrangian VoF advection technique for regime R3. With the same advection technique, aeration coefficient proportionality is more perceivable in this regime comparing to the others.

Among all advection techniques and all regimes, ebf type aeration gives the most accurate results probably due to the bubble behaviour representation. Furthermore, the most accurate VoF advection technique for aeration is revealed as the Split Lagrangian technique. It is not possible to offer a coefficient of aeration providing a global solution.

5 CONCLUSION AND RECOMMENDATIONS

5.1 Conclusions

In the design of hydraulic structures, the role of numerical modelling is increasing and physical models are used less. Although physical model studies (with almost perfect solutions in scale limitations) are the most common and safe way to achieve realistic results, the physical model has some disadvantages such as high costs and long construction times. Computational fluid dynamics tolerating these disadvantages and became an alternative engineering tool that uses computer-aided simulation techniques to be used for accurate estimates of complex fluid flow patterns. The technique facilitates the simulation of a fluid flow process in which the standard flow equations are decomposed and resolved in each calculation cell. The CFD technique has reasonable results and in most cases is relatively economic; however, the reliability of simulation for each type of case should be assessed before use in construction. This depends on both the adequacy and correct use of the codes.

Despite some of the limitations of CFD tools such as long run times and numerical imbalances, these tools make the investigations more economical and provide more detail about hydraulic features from the scaled physical model. Besides, modifications can be easily and robustly adapted to many scenarios to be tested with the numerical model. Thus, numerical models offer the flexibility to work in a wide range of different flow conditions. For an accurate numerical solution, however, it is significant to select the proper grid mesh with the correct boundary and initial conditions to manage the time appropriately.

In this study, FLOW-3D®, which uses the VoF (Volume of Fluid) technique and solves RANS (Reynolds Averaged Navier-Stokes) equations, is used for numerical modelling of two-phase flow research in a single dropshaft geometry. Three types of VoF (Volume of Fluid) advection technique, named Standard technique, Unsplit Lagrangian technique & Split Lagrangian techniques are compared with the result of a previously conducted experiment. The air entrainment model with its sub-options was also examined to assess the sensitivity and calibration of complex air-water flow phenomena.

The main purpose of this study was to explore the numerical flow parameters of dropshafts to guide further investigations of numerical flow field optimizations under the light of this thesis. Further studies may be conducted by using the conclusions and recommendations of this thesis to study the relationships between nondimensionalized variables and propose design ratios of the manhole geometry.

Though as it is presented that the location, water profile and aeration intensity features of the solutions are similar but non-identical, the results observed by the Split Lagrangian technique among the other CFD VoF advection techniques show more compatible flow pattern and aeration as experimental study results for all regimes of R1, R2 and R3.

It is shown that the techniques are similar for water profile on the main symmetry line; however, the collided water jet behaviour and entrained air distribution are different from each other.

The results obtained from the study are:

1- Computational Fluid Dynamics is an effective instrument for analyzing the two-phase free-surface flow occurring in the drop manholes. The correct parameters should be used to obtain results parallel to the physical models. In the results of the numerical model, a parameter validation using the physical model provides confidence. CFD tools can be used as an alternative design aid for the civil engineering discipline as in other disciplines.
2- Fine mesh usage near the wall is required to calculate the energy dissipation and impact number correctly. The balance between the duration and accuracy is required to be judged by the investigator.
3- There is almost neither effect of boundary constraint on energy dissipation, time efficiency nor cumulative volume error.
4- The computation of energy dissipation for fluid-fluid collision is fairly compatible; however, the computation of energy dissipation for the fluid-solid collision depends on the impact location of a water jet in regime R3.

5- Free surface tracking of the standard technique and the Lagrangian techniques differentiated from each other and the consequences affect the velocity field and the entrained air distribution.

6- The air entrainment model in Flow 3D measures the amount of entrained air in the fluid qualitatively and there are some parameters in the sub-options of this model. The parameters are highly influential on the calibration of two-phase flow with one fluid solution. It has been demonstrated how effective the relevant parameters are in the calibration phase and the way to calibrate the two-phase flow numerical model is shown.

7- A passive and active model of air entrainment differs from each other in the cases of highly turbulent dropshafts. Moreover, the active models, the Drift-Flux model and the bulking model are also differentiated from each other with the aeration distribution results. Drift-Flux model utilization is recommended for realistic solutions.

8- For this type of complex flows in drop manholes, impingement location is essential to track the fluid advection accurately and thus to capture the correct air entrainment distribution.

9- The Unsplit Lagrangian VoF advection technique has a significant cumulative volumetric loss. This affects air distribution compatibility negatively.

10- Some parameter range recommendations related to robust computation and air entrainment calibration are mentioned in the recommendations section.

11- For computational time consumption, the most costly ones are; regime R3 among regimes, drift-flux among aeration options, the Split Lagrangian VoF technique among advection options.

5.2 Recommendations

To make a further comparison, experimental measurements with a lower margin of error are required. To decrease the duration of computation, the isolated fluid droplet removal (FCLEAN) option is recommended to be used for the non-finest transitional mesh refinement process.

For the simulations of dropshafts and other types of plunging jets, the Split Lagrangian VoF advection technique is suggested in the cases up to 0.7% cumulative volume increase is tolerable. ebf type aeration is recommended to be used with the Split Lagrangian VoF advection technique.

The contribution of the aeration coefficient on the air entrainment showed linear behaviour as in the equation for the Standard VoF advection technique, but not proportionally equal to the aeration coefficient, and thus, there is no need to simulate intermediate values for model calibration. Instead, linear interpolation is recommended.

REFERENCES

Ardıclıoglu, M., 2017, Kanalizasyon Sistemleri Ders Notu, Kayseri.

Barkhudarov, M. R., 2003, Lagrangian VoF advection Method for FLOW-3D®, Flow Science, Inc.

Bna, S., Cervone, A., Le Chenadec V., Sandro M. and Scardovelli R., 2013, Review of Split and Unsplit Geometric Advection Algorithms, *Proc. of AIP Conference,* Rhodes, Greece, Vol. 1558. 875-878. *https://doi.org/10.1063/1.4825636*

Bombardelli, F., Hirt, C. and García, M., 2001, Computations of Curved Free Surface Water Flow on Spiral Concentrators, Disc., *Hydraulic Engineering*, ASCE, 127(7), 629-631.

Brethour, J. M., 2009, Improved Generalized Minimal Residual (GMRES) Solver in FLOW-3D—How it works and when to use it, Flow Science, Inc.

Brethour, J. M., and Hirt, C. W., 2009, Drift model for two-component flows. FSI-09-TN83Rev. Flow Science, Inc.

Calomino, F., Prega, G., Piro, P., and Veraldi, M. G., 1999, Hydraulics of drops in supercritical flow. *Proc. of 8th International Conference on Urban Storm Drainage ICUSD*, Sydney, Australia.

Camino, G. A., Zhu, D. Z., Rajaratnam, N. and Shome M., 2009, Use of a stacked drop manhole for energy dissipation: A case study in Edmonton, *Canadian Journal of Civil Engineering*, 36, 1037-1050. *https://doi.org/10.1139/L09-036*

Camino, G. A., 2011, Hydraulics of Plunging Drop Structures in Urban Drainage Systems, Doctoral thesis. *Civil and Environmental Engineering. University of Alberta*, Alberta.

Camino, G. A., Zhu, D. Z. and Rajaratnam, N., 2011, Hydraulics of stacked drop manholes, *Irrigation and Drainage Engineering*, 137 (8), 537–552.

Camino, G., Zhu, D. Z. and Rajaratnam, N., 2015, Flow observations in tall plunging flow dropshafts, *Hydraulic Engineering*, *https://doi.org/10.1061/(ASCE)HY.1943-7900.0000939*

Chanson, H., 1999, Energy dissipation and drop structures in ancient times: The Roman dropshafts, *Water 99 Joint Congress*, *Handbook and Proc.*, *Institution of Engineers*, Brisbane, Australia, 987–992. *https://doi.org/10.1680/jencm.16.00023*

Chanson, H., 2000, Hydraulics of Roman aqueducts: Steep chutes, cascades, and dropshafts, *American Archaeology*, 104, 47–72. *https://doi.org/10.2307/506792*

Chanson, H., 2002, An experimental study of Roman dropshaft hydraulics, *Hydraulic Research*, 40(1), 3-12. *https://doi.org/10.1080/00221680209499868*

Chanson, H., 2003, Experimental investigation of dropshaft hydraulics: two-phase flow and acoustics, *Proc. of 30th IAHR Congress*, Thessaloniki, Greece, 353-360.

Chanson, H., 2004, Hydraulics of rectangular dropshafts, *Irrigation and Drainage Engineering*, ASCE, 130(6), 523-529. *https://doi.org/10.1061/(ASCE)0733-9437(2004)130:6(523)*

Chanson, H., 2004, Understanding air-water mass transfer in rectangular dropshafts, *Environmental Engineering of Science*, 3(5), 319–330. *https://doi.org/10.1139/s04-014*

Chanson, H., 2007, Air entrainment processes in a full-scale rectangular dropshaft at large flows, *Hydraulic Research*, 45 (1), 43–53. *https://doi.org/10.1080/00221686.2007.9521742*

Christodoulou, G. C., 1991, Drop manholes in supercritical pipelines, *Irrigation and Drainage Engineering* 117 (1), 37-47. *https://doi.org/10.1061/(ASCE)0733-9437(1991)117:1(37)*

The City of Calgary, T., 2000, Stormwater management and design manual. The city of Calgary. Calgary.

The City of Edmonton., 2015, Design and construction standards, Volume 3: Drainage. The city of Edmonton. Edmonton.

David, T. S., and Hirt, C. W., 2004, modelling turbulent entrainment of air at a free surface, Flow Science.

De Marinis, G., Gargano, R., Granata, F. and Hager, W. H., 2007, Circular drop manholes: Preliminary experimental results. *Proc. of 32nd IAHR Congress* (CD-ROM), Venice, Italy, 1–6 July.

De Martino, F., Gisonni, C. and Hager, W. H., 2002, Drop in combined sewer manhole for supercritical flow, *Irrigation and Drainage Engineering* 128(6), 397-400. https://doi.org/10.1061/(ASCE)0733-9437(2002)128:6(397)

Edwini-Bonsu, S. and Steffler, P. M., 2006, Modelling ventilation phenomenon in sanitary sewer systems: A system theoretic approach, *Hydraulic Engineering*, https://doi.org/10.1061/(ASCE)0733-9429(2006)132:8(778)

Falvey, H. T., 1980, Air-water flow in hydraulic structures. *Engineering monograph* No. 41. Denver, CO, US Bureau of Reclamation.

Flow Science, Inc., 2012, FLOW-3D® User's Manual.

Gayer, J. A., 1984, On the hydraulic role of manholes in urban storm drainage systems, *Proc. of 3rd Int. Conf. on Urban Storm Drainage*, Goteborg, 1984.

Gargano, R., Granata, F. and de Marinis, G., 2008, IL trasporto d'aria nei pozzetti di salto circolari. *Proc. of 31 Convegno Nazionale di Idraulica e Costruzioni Idrauliche*, Perugia, September 9-12, 2008.

Granata, F., de Marinis, G., Gargano R., and Hager W. H., 2009, Energy Loss in Circular Drop Manholes, *Proc. of 33rd IAHR Congress*, Vancouver, Canada, 2285-2292.

Granata, F., Gargano R., de Marinis, G., and Hager W. H., 2010, choking features of drop manholes in sewer systems, *Proc. of 1st European IAHR Congress*, Edinburg, UK.

Granata, F., de Marinis, G., Gargano R. and Hager W. H., 2011, Hydraulics of circular drop manholes, *Irrigation and Drainage Engineering*, ASCE, 137(2), 102-111. https://doi.org/10.1061/(ASCE)IR.1943-4774.0000279

Granata, F., de Marinis, G. and Gargano R., 2014, Flow improving elements in circular drop manholes, *Hydraulic Research*, 52(3), 347-355.

Granata, F., de Marinis, G. and Gargano, R., 2015, Air-water flows in circular drop manholes, *Urban Water*, 12(6), 477–487.

Granata, F., 2016, Dropshaft cascades in urban drainage systems. *Water Science and Technology* 73 (9), 2052–2059. https://doi.org/10.2166/wst.2016.051

Granata, F. and de Marinis, G., 2017, Machine learning method for wastewater hydraulics, *Flow Measurement and Instrumentation*, 57, 1-9. http://doi.org/10.1016/j.flowmeasinst.2017.08.004

Gualtieri, C. and Chanson, H, 2013, Interparticle arrival time analysis of bubble distributions in a dropshaft and hydraulic jump, *Hydraulic Research*, 51(3), 253–264. http://doi.org/10.1080/00221686.2012.762430

Hager, W. H., 1999, Wastewater Hydraulics. Theory and practice. Springer, Berlin.p.628

Hirt, C. W., and Nichols B. D., 1981, Volume of Fluid (VoF) Method for the Dynamics of Free Boundaries, *Computational Physics*, 39, 201-225. *https://doi.org/10.1016/0021-9991(81)90145-5*

Hirt, C. W., 2012, Modelling Turbulent Entrainment of Air at a Free Surface, Flow science report 01-12. Flow Science Inc.

Jalil, A., 2009, Experimental and numerical study of plunging flow in vertical dropshafts, Doctoral thesis, *Civil and Environmental Engineering. University of Alberta*, Alberta, 215.

Jensen, H., Biggs, C. A. and Karunakaran, E., 2016, The importance of sewer biofilms, *WIREs Water*, 3(4), 487-494. *https://doi.org/10.1002/wat2.1144*

Kaya, M. N., Kose, F., Ingham, D., Ma, L., & Pourkashanian, M., 2018, Aerodynamic performance of a horizontal axis wind turbine with forward and backward swept blades. *Journal of Wind Engineering and Industrial Aerodynamics*, 176, 166-173.

Kumcu, S. Y. and Kokpinar M. A., 2013, Air-Water Flow Structure in a Circular Dropshaft, *Proc. of World Environmental and Water Resources Congress*, Ohio, USA.

Kumcu, S. Y. and Ucar, M., 2017, Dairesel kesitli düşülü bacalarda hava-su karışımının deneysel çalişma ve CFD modelleme ile analizi, *DSİ Teknik Bülteni*, 124, 34-43.

Kumcu, S. Y. and Ucar, M., 2018, Effect of Experimental and Mathematical Modelling of Spillway on Dam Safety, *Proc. of AHFE 9th*, 369-305, Orlando, USA.

Ma, Y., Zhu, D. Z. and Rajaratnam N., 2016, Air Entrainment in a Tall Plunging Flow Dropshaft, *Hydraulic Engineering*, 142 (10) 04016038. *https://doi.org/10.1061/(ASCE)HY.1943-7900.0001181*

Ma, Y., Zhu, D. Z., Rajaratnam N., and van Duin B., 2017, Energy Dissipation in Circular Drop Manholes, *Irrigation and Drainage Engineering* 143(12).

Moeller, W. P., and Natarius E., 2000, The Vortex Drop Structure Implementatıon for Odour and Corrosion Control, Metropolitan Council Environmental Services 3565 Kennebec Drive Eagan, Minnesota 55122-1036 *https://doi.org/10.2175/193864700784545577*

Movaheida, A., Delavari A. and Farahi M., 2015, Designing Manhole in Water Transmission Lines Using FLOW-3D® Numerical Model, *Civil Engineering*, 1(1). *https://doi.org/10.28991/cej-030987*

Pagliara, S. and Dazzini, D., 2002, Energy dissipation on stepped fall manholes. *Proc. of 9. ICUD Conf. Urban Drainage*, Portland, Oregon. *https://doi.org/10.1061/40644(2002)315*

Rajaratnam, N., Johnston, G. A. and Barber, M. A., 1993, Energy dissipation by jet diffusion in stormwater dropshafts, *Canadian Journal of Civil Engineering*, 20(3), 374–379. *https://doi.org/10.1139/l93-052*

Rajaratnam, N., Mainali A. and Hsung C. Y., 1997, Observations on Flow in Vertical Dropshafts in Urban Drainage Systems, *Environmental Engineering*, ASCE, 123 (5), 486-491. *https://doi.org/10.1061/(ASCE)0733-9372(1997)123:5(486)*

Sousa, V. F., Bombardelli, F. A. and Chanson, H, 2009, Numerical simulation of rectangular dropshafts using a Volume-of-Fluid (VoF) Method, *Proc. of 33rd Congress of the IAHR.*

Ucar, M. and Kumcu S. Y., 2018, Comparison of physical modelling and CFD simulation of flow over spillway in the Arkun Dam, *Proc. of 5th International Symp. on Dam Safety*, Istanbul, Turkey.

Valero, D., García-Bartual, R., 2016, Calibration of an Air Entrainment Model for CFD Spillway Applications. In: Gourbesville P., Cunge J., Caignaert G. (eds) Advances in Hydroinformatics. Springer Water. Springer, Singapore. https://doi.org/10.1007/978-981-287-615-7_38

Vanneste, D. F. A., 2012, Experimental-and-Numerical-study-of-Wave-Induced-Porous-Flow-in-Rubble-Mound-Breakwaters, Doctoral Thesis, *Ghent University*, Ghent, *https://doi.org/10.13140/RG.2.1.4666.9925*

Wei J., Ma Y., Zhu D. Z. and Zhang, J., 2018, Effect of boundary conditions on the performance of a dropshaft with an internal divider, *Water Science and Tech*nology 2, 441-449. *https://doi.org/10.2166/wst.2018.163*

Zhang, W., Wang, J., Zhou, C., Dong, Z. And Zhou, Z., 2018, Numerical Simulation of Hydraulic Characteristics in A Vortex Dropshaft, *Water*, 10(0), *https://doi.org/10.3390/w10101393*

Zhang W., Zhu D. Z., Rajaratnam N., Edwini-Bonsu S., Fiala, J. and Pelz, W., 2016, Use of Air Circulation Pipes in Deep Dropshafts for Reducing Air Induction into Sanitary Sewers, *Environmental Engineering*, ASCE, 142(4). *https://doi.org/10.1061/(ASCE)EE.1943-7870.0001046*

Zheng, F., Li, Y., Zhao, J. and An, J., 2017, Energy Dissipation in Circular Drop Manholes under Different Outflow Conditions, *Water*, 9(752). *https://doi.org/10.3390/w9100752*

APPENDIX-A

Table A.1 Energy dissipation data for each condition type tested with elevation constrained BC.

Q (m^3/s)	Grid Type	Aeration Type	VoF Advection	Aeration Coefficient	Volume error (%lost)	Energy Dissipation (m)	% Dissipation	I	y_0F_0
1	M1	e	Standard	0.50	-0.04%	0.48757	0.75602	0.32637	0.20302
1	M1	eb	Standard	0.50	0.00%	0.48146	0.74638	0.32403	0.20262
1	M1	ebf	Standard	0.50	0.02%	0.48211	0.74741	0.32409	0.20263
1	M2	e	Standard	0.50	-0.01%	0.48173	0.74673	0.30369	0.19235
1	M2	eb	Standard	0.50	0.01%	0.48202	0.74683	0.29704	0.19021
1	M2	ebf	Standard	0.50	0.03%	0.48304	0.74841	0.29703	0.19020
1	M3	e	Standard	0.40	0.00%	0.48214	0.74694	0.29361	0.18842
1	M3	e	Standard	0.45	0.00%	0.48099	0.74661	0.30930	0.19015
1	M3	e	Standard	0.50	0.00%	0.48099	0.74661	0.30930	0.19015
1	M3	e	Standard	0.55	0.00%	0.48214	0.74694	0.29361	0.18842
1	M3	e	Standard	0.60	0.00%	0.48066	0.74611	0.30930	0.19015
1	M3	eb	Standard	0.40	0.00%	0.48108	0.74643	0.30135	0.18717
1	M3	eb	Standard	0.45	0.00%	0.48101	0.74632	0.30130	0.18715
1	M3	eb	Standard	0.50	0.00%	0.48103	0.74634	0.30137	0.18717
1	M3	eb	Standard	0.55	0.01%	0.48110	0.74644	0.30213	0.18771
1	M3	eb	Standard	0.60	0.01%	0.48123	0.74666	0.30132	0.18716
1	M3	ebf	Standard	0.40	0.00%	0.48219	0.74691	0.28976	0.18652
1	M3	ebf	Standard	0.45	0.00%	0.48298	0.74814	0.28970	0.18650
1	M3	ebf	Standard	0.50	-0.01%	0.48211	0.74678	0.28966	0.18648
1	M3	ebf	Standard	0.55	0.00%	0.48206	0.74672	0.28992	0.18659
1	M3	ebf	Standard	0.60	0.00%	0.48224	0.74704	0.29060	0.18682
1	M3	e	Unsplit L.	0.40	8.40%	0.48502	0.75236	0.29949	0.18694
1	M3	e	Unsplit L.	0.45	8.40%	0.48502	0.75236	0.29949	0.18694
1	M3	e	Unsplit L.	0.50	8.40%	0.48502	0.75236	0.29949	0.18694
1	M3	e	Unsplit L.	0.55	8.40%	0.48502	0.75236	0.29949	0.18694
1	M3	e	Unsplit L.	0.60	8.40%	0.48502	0.75236	0.29949	0.18694
1	M3	eb	Unsplit L.	0.40	8.40%	0.48507	0.75245	0.29947	0.18691
1	M3	eb	Unsplit L.	0.45	8.40%	0.48506	0.75243	0.29948	0.18693
1	M3	eb	Unsplit L.	0.50	8.40%	0.48508	0.75245	0.29947	0.18692
1	M3	eb	Unsplit L.	0.55	8.40%	0.48509	0.75248	0.29948	0.18693
1	M3	eb	Unsplit L.	0.60	8.40%	0.48504	0.75240	0.29948	0.18694
1	M3	ebf	Unsplit L.	0.40	4.30%	0.48367	0.74920	0.29952	0.19265
1	M3	ebf	Unsplit L.	0.45	3.60%	0.48398	0.74967	0.29935	0.19257
1	M3	ebf	Unsplit L.	0.50	2.40%	0.48405	0.75086	0.29959	0.18700
1	M3	ebf	Unsplit L.	0.55	2.50%	0.48081	0.74584	0.29964	0.18700
1	M3	ebf	Unsplit L.	0.60	2.30%	0.48244	0.74836	0.29963	0.18700
1	M3	e	Split L.	0.40	-0.54%	0.48108	0.74627	0.29955	0.18689
1	M3	e	Split L.	0.45	-0.54%	0.48108	0.74627	0.29955	0.18689
1	M3	e	Split L.	0.50	-0.54%	0.48108	0.74627	0.29955	0.18689

1	M3	e	Split L.	0.55	-0.54%	0.48108	0.74627	0.29955	0.18689
1	M3	e	Split L.	0.60	-0.54%	0.48108	0.74627	0.29955	0.18689
1	M3	eb	Split L.	0.40	-0.44%	0.48100	0.74616	0.29955	0.18680
1	M3	eb	Split L.	0.45	-0.43%	0.48094	0.74607	0.29946	0.18676
1	M3	eb	Split L.	0.50	-0.44%	0.48140	0.74678	0.29946	0.18678
1	M3	eb	Split L.	0.55	-0.44%	0.48090	0.74600	0.29947	0.18678
1	M3	eb	Split L.	0.60	-0.44%	0.48102	0.74619	0.29944	0.18676
1	M3	ebf	Split L.	0.40	-0.34%	0.48089	0.74600	0.29940	0.18663
1	M3	ebf	Split L.	0.45	-0.33%	0.48125	0.74660	0.29928	0.18638
1	M3	ebf	Split L.	0.50	-0.33%	0.48124	0.74656	0.29945	0.18664
1	M3	ebf	Split L.	0.55	-0.32%	0.48106	0.74628	0.29936	0.18659
1	M3	ebf	Split L.	0.60	-0.32%	0.48178	0.74737	0.29934	0.18661
1	M4	e	Standard	0.50	0.00%	0.48156	0.74681	0.29890	0.18763
1	M4	eb	Standard	0.50	-0.01%	0.48151	0.74672	0.29885	0.18761
1	M4	ebf	Standard	0.50	0.00%	0.48178	0.74715	0.29885	0.18761
1	-	-	-	-	-	0.48049	0.74818	0.30621	0.17659
3	M1	e	Standard	0.50	0.13%	0.43051	0.63333	0.43615	0.35556
3	M1	eb	Standard	0.50	-0.04%	0.42196	0.62075	0.43597	0.35551
3	M1	ebf	Standard	0.50	-0.02%	0.42942	0.63171	0.43596	0.35550
3	M2	e	Standard	0.50	0.00%	0.47605	0.69956	0.43362	0.35801
3	M2	eb	Standard	0.50	0.01%	0.47686	0.70073	0.43320	0.35785
3	M2	ebf	Standard	0.50	0.02%	0.47933	0.70439	0.43372	0.35805
3	M3	e	Standard	0.40	-0.05%	0.47392	0.69540	0.39493	0.33107
3	M3	e	Standard	0.45	-0.06%	0.47391	0.69540	0.39494	0.33107
3	M3	e	Standard	0.50	-0.06%	0.47391	0.69540	0.39494	0.33107
3	M3	e	Standard	0.55	-0.05%	0.47392	0.69540	0.39493	0.33107
3	M3	e	Standard	0.60	-0.06%	0.47391	0.69540	0.39494	0.33107
3	M3	eb	Standard	0.40	-0.02%	0.48208	0.70738	0.39492	0.33108
3	M3	eb	Standard	0.45	0.03%	0.48095	0.70572	0.39492	0.33108
3	M3	eb	Standard	0.50	0.03%	0.48211	0.70741	0.39493	0.33108
3	M3	eb	Standard	0.55	-0.02%	0.48062	0.70523	0.39492	0.33108
3	M3	eb	Standard	0.60	-0.01%	0.47944	0.70350	0.39492	0.33107
3	M3	ebf	Standard	0.40	0.00%	0.47285	0.69383	0.39492	0.33107
3	M3	ebf	Standard	0.45	0.00%	0.47309	0.69419	0.39493	0.33107
3	M3	ebf	Standard	0.50	0.00%	0.47252	0.69335	0.39494	0.33109
3	M3	ebf	Standard	0.55	0.00%	0.47252	0.69335	0.39494	0.33109
3	M3	ebf	Standard	0.60	0.00%	0.47296	0.69399	0.39494	0.33109
3	M3	e	Unsplit L.	0.40	8.50%	0.46832	0.68747	0.39676	0.33106
3	M3	e	Unsplit L.	0.45	8.50%	0.46832	0.68747	0.39676	0.33106
3	M3	e	Unsplit L.	0.50	8.50%	0.46832	0.68747	0.39676	0.33106
3	M3	e	Unsplit L.	0.55	8.50%	0.46832	0.68747	0.39676	0.33106
3	M3	e	Unsplit L.	0.60	8.50%	0.46832	0.68747	0.39676	0.33106
3	M3	eb	Unsplit L.	0.40	8.00%	0.47379	0.69551	0.39686	0.33110
3	M3	eb	Unsplit L.	0.45	8.00%	0.47206	0.69297	0.39686	0.33110
3	M3	eb	Unsplit L.	0.50	7.70%	0.47169	0.69245	0.39725	0.33126

3	M3	eb	Unsplit L.	0.55	8.00%	0.47267	0.69386	0.39686	0.33110
3	M3	eb	Unsplit L.	0.60	7.90%	0.47521	0.69759	0.39686	0.33110
3	M3	ebf	Unsplit L.	0.40	7.50%	0.46538	0.68317	0.39694	0.33114
3	M3	ebf	Unsplit L.	0.45	7.40%	0.46454	0.68195	0.39704	0.33116
3	M3	ebf	Unsplit L.	0.50	7.40%	0.46756	0.68636	0.39689	0.33111
3	M3	ebf	Unsplit L.	0.55	6.80%	0.46643	0.68472	0.39705	0.33117
3	M3	ebf	Unsplit L.	0.60	6.40%	0.46670	0.68510	0.39706	0.33130
3	M3	e	Split L.	0.40	-0.93%	0.46017	0.67557	0.39738	0.33129
3	M3	e	Split L.	0.45	-0.93%	0.46017	0.67557	0.39738	0.33129
3	M3	e	Split L.	0.50	-0.93%	0.46017	0.67557	0.39738	0.33129
3	M3	e	Split L.	0.55	-0.93%	0.46017	0.67557	0.39738	0.33129
3	M3	e	Split L.	0.60	-0.93%	0.46017	0.67557	0.39738	0.33129
3	M3	eb	Split L.	0.40	-0.65%	0.45876	0.67350	0.39737	0.33129
3	M3	eb	Split L.	0.45	-0.66%	0.46132	0.67725	0.39744	0.33132
3	M3	eb	Split L.	0.50	-0.65%	0.46107	0.67689	0.39742	0.33131
3	M3	eb	Split L.	0.55	-0.66%	0.46121	0.67709	0.39740	0.33130
3	M3	eb	Split L.	0.60	-0.66%	0.46149	0.67751	0.39747	0.33133
3	M3	ebf	Split L.	0.40	-0.67%	0.46221	0.67857	0.39748	0.33134
3	M3	ebf	Split L.	0.45	-0.68%	0.46207	0.67836	0.39748	0.33134
3	M3	ebf	Split L.	0.50	-0.67%	0.46223	0.67860	0.39752	0.33136
3	M3	ebf	Split L.	0.55	-0.69%	0.46246	0.67893	0.39751	0.33135
3	M3	ebf	Split L.	0.60	-0.69%	0.46250	0.67899	0.39748	0.33134
3	M4	e	Standard	0.50	0.00%	0.46735	0.68521	0.39108	0.33088
3	M4	eb	Standard	0.50	0.01%	0.40142	0.58854	0.39107	0.33086
3	M4	ebf	Standard	0.50	0.00%	0.39068	0.57281	0.39107	0.33085
3	-	-	-	-	-	0.47072	0.69773	0.45394	0.34070
5	M1	e	Standard	0.50	0.22%	0.37350	0.53038	0.60138	0.52550
5	M1	eb	Standard	0.50	0.47%	0.36545	0.51895	0.60138	0.52550
5	M1	ebf	Standard	0.50	0.04%	0.38198	0.54242	0.60138	0.52550
5	M2	e	Standard	0.50	-0.02%	0.34397	0.48900	0.54730	0.48793
5	M2	eb	Standard	0.50	-0.04%	0.35286	0.50164	0.54740	0.48796
5	M2	ebf	Standard	0.50	0.07%	0.35327	0.50221	0.54738	0.48795
5	M3	e	Standard	0.40	0.00%	0.34450	0.48956	0.51964	0.46634
5	M3	e	Standard	0.45	0.00%	0.34450	0.48956	0.51964	0.46634
5	M3	e	Standard	0.50	0.00%	0.34450	0.48956	0.51964	0.46634
5	M3	e	Standard	0.55	0.00%	0.34450	0.48956	0.51964	0.46634
5	M3	e	Standard	0.60	0.00%	0.34450	0.48956	0.51964	0.46634
5	M3	eb	Standard	0.40	0.00%	0.35529	0.50488	0.51938	0.46624
5	M3	eb	Standard	0.45	0.00%	0.35598	0.50586	0.51944	0.46626
5	M3	eb	Standard	0.50	0.00%	0.35755	0.50809	0.51943	0.46626
5	M3	eb	Standard	0.55	0.00%	0.34665	0.49260	0.51947	0.46628
5	M3	eb	Standard	0.60	0.00%	0.35401	0.50307	0.51956	0.46631
5	M3	ebf	Standard	0.40	0.00%	0.35768	0.50827	0.51944	0.46626
5	M3	ebf	Standard	0.45	0.00%	0.35215	0.50042	0.51933	0.46622
5	M3	ebf	Standard	0.50	0.00%	0.35141	0.49936	0.51941	0.46625

5	M3	ebf	Standard	0.55	0.01%	0.36941	0.52494	0.51941	0.46625
5	M3	ebf	Standard	0.60	-0.01%	0.35539	0.50501	0.51923	0.46618
5	M3	e	Unsplit L.	0.40	1.90%	0.35693	0.50726	0.51914	0.46557
5	M3	e	Unsplit L.	0.45	1.80%	0.35793	0.50868	0.51913	0.46557
5	M3	e	Unsplit L.	0.50	1.80%	0.35793	0.50868	0.51913	0.46557
5	M3	e	Unsplit L.	0.55	1.90%	0.35693	0.50726	0.51914	0.46557
5	M3	e	Unsplit L.	0.60	1.80%	0.35793	0.50868	0.51913	0.46557
5	M3	eb	Unsplit L.	0.40	1.90%	0.35989	0.51146	0.51900	0.46552
5	M3	eb	Unsplit L.	0.45	1.90%	0.36007	0.51170	0.51895	0.46550
5	M3	eb	Unsplit L.	0.50	1.40%	0.35405	0.50315	0.51892	0.46551
5	M3	eb	Unsplit L.	0.55	1.80%	0.36161	0.51389	0.51885	0.46547
5	M3	eb	Unsplit L.	0.60	1.90%	0.35840	0.50932	0.51882	0.46546
5	M3	ebf	Unsplit L.	0.40	0.80%	0.35568	0.50547	0.51902	0.46555
5	M3	ebf	Unsplit L.	0.45	1.00%	0.35906	0.51027	0.51892	0.46553
5	M3	ebf	Unsplit L.	0.50	1.00%	0.35630	0.50629	0.51892	0.46604
5	M3	ebf	Unsplit L.	0.55	0.86%	0.35732	0.50779	0.51888	0.46550
5	M3	ebf	Unsplit L.	0.60	0.74%	0.35363	0.50256	0.51909	0.46556
5	M3	e	Split L.	0.40	-0.25%	0.35912	0.51033	0.51864	0.46542
5	M3	e	Split L.	0.45	-0.23%	0.35625	0.50626	0.51874	0.46545
5	M3	e	Split L.	0.50	-0.23%	0.35625	0.50626	0.51874	0.46545
5	M3	e	Split L.	0.55	-0.25%	0.35912	0.51033	0.51864	0.46542
5	M3	e	Split L.	0.60	-0.25%	0.35912	0.51033	0.51864	0.46542
5	M3	eb	Split L.	0.40	-0.27%	0.35257	0.50103	0.51873	0.46545
5	M3	eb	Split L.	0.45	-0.26%	0.35542	0.50508	0.51869	0.46543
5	M3	eb	Split L.	0.50	-0.25%	0.35697	0.50728	0.51869	0.46545
5	M3	eb	Split L.	0.55	-0.26%	0.35649	0.50660	0.51870	0.46544
5	M3	eb	Split L.	0.60	-0.28%	0.35729	0.50774	0.51876	0.46546
5	M3	ebf	Split L.	0.40	-0.34%	0.34747	0.49379	0.51868	0.46543
5	M3	ebf	Split L.	0.45	-0.30%	0.35316	0.50187	0.51874	0.46546
5	M3	ebf	Split L.	0.50	-0.31%	0.34964	0.49686	0.51874	0.46552
5	M3	ebf	Split L.	0.55	-0.30%	0.35227	0.50059	0.51857	0.46541
5	M3	ebf	Split L.	0.60	-0.33%	0.35123	0.49911	0.51848	0.46539
5	M4	e	Standard	0.50	-0.01%	0.34236	0.48643	0.51909	0.46657
5	M4	eb	Standard	0.50	0.00%	0.34747	0.49370	0.51920	0.46660
5	M4	ebf	Standard	0.50	0.00%	0.36495	0.51853	0.51901	0.46653
5	-	-	-	-	-	0.44520	0.63475	0.52006	0.45651

e: Basic empirical passive air entrainment option.
eb: Bulking option activated varied density air entrainment option.
ebf: Drift flux option activated air bubble movement tracking air entrainment option.

APPENDIX-B

Table B.1 Energy dissipation rates for BC elevation non-constrained simulations

Q (m^3/s)	Grid Type	Aeration Type	Avrg. elaps. clock time / siml. time	Volume error (%lost)	Energy Dissipation (m)	% Dissipation	I	y_0F_0
1.0	M1	e	5	-0.02%	0.48215	0.74793	0.32836	0.20246
1.0	M1	eb	5	0.00%	0.47925	0.74328	0.32582	0.20196
1.0	M1	ebf	5	-0.01%	0.47667	0.73928	0.32583	0.20196
1.0	M2	e	53	-0.01%	0.48007	0.74472	0.30148	0.18799
1.0	M2	eb	57	0.01%	0.47898	0.74304	0.30150	0.18799
1.0	M2	ebf	61	0.00%	0.47772	0.74108	0.30150	0.18799
1.0	M3	e	278	-0.04%	0.47988	0.74393	0.29908	0.18918
1.0	M3	eb	193	0.03%	0.47901	0.74270	0.30028	0.18926
1.0	3cm	ebf	350	-0.02%	0.47834	0.74148	0.29730	0.18840
1.0	4cm	ebf	400	-0.01%	0.47815	0.74138	0.29643	0.18681
1.0	M3	ebf	280	0.01%	0.47911	0.74297	0.29661	0.18642
1.0	6cm	ebf	290	0.01%	0.47909	0.74271	0.30099	0.19034
1.0	7cm	ebf	310	-0.04%	0.47875	0.74172	0.29941	0.19184
1.0	M4	e	627	-0.02%	0.48086	0.74548	0.29221	0.18458
1.0	M4	eb	653	0.00%	0.47936	0.74360	0.29117	0.18135
1.0	M4	ebf	833	0.01%	0.47721	0.74030	0.29193	0.18158
1.0	-	-	1	-	0.48049	0.74818	0.30621	0.17659
3.0	M1	e	8	0.05%	0.40734	0.59979	0.44082	0.35536
3.0	M1	eb	7	-0.02%	0.41031	0.60419	0.44106	0.35540
3.0	M1	ebf	7	0.03%	0.41673	0.61364	0.44107	0.35540
3.0	M2	e	61	-0.01%	0.47890	0.70539	0.43794	0.35200
3.0	M2	eb	67	0.00%	0.47710	0.70319	0.44193	0.35231
3.0	M2	ebf	73	0.00%	0.47615	0.70112	0.43544	0.35139
3.0	M3	e	328	-0.02%	0.47509	0.69944	0.42248	0.34186
3.0	M3	eb	353	0.03%	0.46750	0.68825	0.42246	0.34187
3.0	M3	ebf	458	0.00%	0.47031	0.69239	0.42242	0.34186
3.0	M4	e	1000	-0.02%	0.46754	0.68845	0.41654	0.33587
3.0	M4	eb	1067	-0.01%	0.46199	0.68028	0.41652	0.33587
3.0	M4	ebf	1417	0.01%	0.46648	0.68688	0.41649	0.33586
3.0	-	-	1	-	0.47072	0.69773	0.45394	0.34070
5.0	M1	e	12	0.00%	0.37275	0.52926	0.53579	0.48371
5.0	M1	eb	11	0.00%	0.36686	0.52091	0.53579	0.48371
5.0	M1	ebf	12	0.00%	0.36590	0.51955	0.53578	0.48371
5.0	M2	e	195	0.01%	0.34864	0.49557	0.54420	0.48606
5.0	M2	eb	201	0.00%	0.35636	0.50654	0.54420	0.48606
5.0	M2	ebf	214	0.01%	0.36090	0.51294	0.54340	0.48582
5.0	M3	e	875	0.08%	0.34486	0.48847	0.49965	0.46081
5.0	M3	eb	910	0.07%	0.35807	0.50718	0.49965	0.46082

5.0	M3	ebf	998	-0.02%	0.35259	0.49941	0.49965	0.46081
5.0	M4	e	1991	0.03%	0.35966	0.50977	0.50402	0.46238
5.0	M4	eb	2148	-0.01%	0.36374	0.51556	0.50400	0.46238
5.0	M4	ebf	2358	0.00%	0.34881	0.49440	0.50402	0.46237
5.0	-	-	1	-	0.44520	0.63475	0.52006	0.45651

e: Basic empirical air entrainment option.
eb: Bulking option activated varied density air entrainment option.
ebf: Drift flux option activated air bubble movement tracking air entrainment option.